

Massive Stellar Populations and the Formation of Binary Black Holes

by

Jonathan (JD) Merritt

A dissertation accepted and approved in partial fulfillment of the
requirements for the degree of
Doctor of Philosophy
in Physics

Dissertation Committee:

Ray Frey, Chair

Ben Farr, Advisor

Tien-Tien Yu, Core Member

Carol Paty, Institutional Representative

University of Oregon

Summer 2025

© 2025 Jonathan (JD) Merritt

This work, including text and images of this document but not including supplemental files (for example, not including software code and data), is licensed under a Creative Commons

Attribution-NoDerivatives 4.0 International License.



DISSERTATION ABSTRACT

Jonathan (JD) Merritt

Doctor of Philosophy in Physics

Title: Massive Stellar Populations and the Formation of Binary Black Holes

Since the detection of Gravitational Waves in 2015, the last decade has seen a rapid evolution of the new field of gravitational wave (GW) astronomy. I have approached the topic from two very different angles, but have converged on a deepened understanding of the same natural phenomenon, the merger of binary black holes (BBH). The first approach is studying and modelling unexplained glitches in the Laser Interferometer Gravitational-Wave Observatory (LIGO) data, with the novel application of data science techniques. These glitches had the potential to confuse otherwise robust search methods for massive BBH merger signals, and required new approaches to mitigation. This involved analysis of the raw data and working closely with the detector characterization experts that monitor the instruments and their environment, as well as work with astrophysical analysis pipelines and the experts in parameter estimation. The second main project included here is from an astrophysical approach, improving the treatment of stellar winds models in the rapid population synthesis code COMPAS, which simulates the evolution and death of massive stars to make predictions about the formation channels of BBH systems that are detected in GWs. This dissertation includes previously published and unpublished co-authored material.

CURRICULUM VITAE

NAME OF AUTHOR: Jonathan (JD) Merritt

GRADUATE AND UNDERGRADUATE SCHOOLS ATTENDED:

University of Oregon, Eugene, OR, USA
Colorado College, Colorado Springs, CO, USA
Wesleyan University, Middletown, CT, USA

DEGREES AWARDED:

Doctor of Philosophy, Physics, 2025, University of Oregon
Bachelor of Arts, Physics, 2015, Colorado College

AREAS OF SPECIAL INTEREST:

Astrophysics of massive stars
Gravitational waves

PROFESSIONAL EXPERIENCE:

Creative Energies, Lander, WY - Solar Installer 2016-2017
University of Oregon - Graduate Employee, Teaching Assistant 2018-2025

PUBLICATIONS:

Implications of modern mass-loss rates for massive stars. JD Merritt, Simon Stevenson, Andreas Sander, Ilya Mandel, Jeff Riley, Ben Farr, Lieke van Son, Tom Wagg, Serena Vinciguerra, Holden Jose. In Prep. **Contributions: COMPAS code development, testing.**

Transient glitch mitigation in Advanced LIGO data with glitschen. J.D. Merritt, Ben Farr, Rachel Hur, Bruce Edelman, Zoheyr Doctor. Phys. Rev. D 104, 102004; 15 Nov. 2021. **Contributions: Lead model development, testing, and writing.**

Not Just Winds: Why Models find Binary Black Hole Formation is Metallicity Dependent, While Binary Neutron Star Formation is Not. L. A. C. van Son, S. K. Roy, I. Mandel, W. M. Farr, A. Lam, J. Merritt, F. S. Broekgaarden, A. Sander, J. J. Andrews. **Contributions: COMPAS debugging and winds models.**

Constraining Unmodeled Physics with Compact Binary Mergers from GWTC-1. Bruce Edelman, Francisco J. Rivera-Paleo, J.D. Merritt, Ben Farr, Zoheyr Doctor, Jeandrew Brink, Will M. Farr, Jonathan Gair, Joey Shapiro Key, Jess McIver, Alex B. Nielsen. Phys. Rev. D 103, 042004 (2021). **Contributions: Model Testing.**

GWTC-3: Compact Binary Coalescences Observed by LIGO and Virgo During the Second Part of the Third Observing Run. R. Abbott et. al., the Virgo Collaboration. **Contributions: Parameter Estimation and Detector Characterization, investigation of glitchlike events.**

GWTC-2: Compact Binary Coalescences Observed by LIGO and Virgo during the First Half of the Third Observing Run. The LIGO Scientific Collaboration. **Contributions: Generated Figure 1, Parameter Estimation in O3a.**

ACKNOWLEDGEMENTS

I want to thank my family for raising me to be in appreciation of nature and always asking interesting questions, my father for kindling a love of science, my mother for providing the model of a scientist, and my brother for being my best friend. I want to thank my advisor, Ben, for unwavering support, understanding, and positivity. This was especially critical during the hard times, and when this work was not my main priority. His values of balance and thriving in a well-rounded life made this achievement possible for me with a dual life as a climber, and I wish more people in science could do the same. I want to thank my fellow graduate students, especially Bruce Edelman, Jordan Palamos, and Phillippe Nguyen, for their mentorship in a new and difficult field. I want to thank my collaborators in the LIGO/LVK collaboration for sharing their staggering decades of work and experience with new analysts. I want to thank Simon Stevenson, Jeff Riley, Ilya Mandel, and everyone I met in Melbourne for their continuing mentorship, openness, and collaborative energy that inspired me to pivot into a new field and changed my life.

This dissertation is the product of unionized labor as part of the Graduate Teaching Fellows Federation, AFT Local 3544.

Dedicated to my partner Tory, who helped me through all of this, with love, and cats, and dogs, and chickens and ducks, and even fish and shrimp, and wonderful time outside, travelling the world, in the garden, through good and bad and everything in between.

TABLE OF CONTENTS

Chapter	Page
I. INTRODUCTION	20
II. GENERAL RELATIVITY	23
2.1. Gravitational Waves and General Relativity	23
2.1.1. Linearized Gravitational Waves	24
2.2. Production and Sources of GWs	28
2.3. Astrophysical Sources	30
2.3.1. Bursts	30
2.3.2. Continuous Waves	31
2.3.3. Stochastic Signals	31
2.3.4. Coalescing Compact Binaries	31
III. DETECTION OF GRAVITATIONAL WAVES	32
3.1. History of Gravitational Wave Detectors	32
3.1.1. Resonant Bar Detectors	32
3.1.2. History of Interferometric Detectors	34
3.2. Direct Detections of Gravitational Waves	35
3.3. Interferometric Detector Design	35
3.4. Analysis of Gravitational Wave Data	40
3.4.1. Noise Model	40
3.5. Basic Properties of Detector Noise	41
3.5.1. Likelihood	42
3.5.2. Matched Filtering Formalism	44
3.5.3. Signal Model	45

Chapter	Page
3.5.4. Parameter Estimation	46
IV. STELLAR ASTROPHYSICS	47
4.1. Intrinsic Stellar Parameters	47
4.1.1. Surface Temperature	48
4.1.2. Luminosity	48
4.1.3. Mass	49
4.1.4. Radius	49
4.1.5. Rotation	50
4.1.6. Metallicity	52
4.2. Physical Processes and their Timescales	54
4.2.1. Dynamical Timescale	54
4.2.2. Thermal Timescale	54
4.2.3. Nuclear Timescale	55
4.2.4. Diffusion Timescale	56
4.2.5. Pulsation	57
4.2.6. Mass-Loss Timescale	57
4.2.7. Internal Structure	58
4.2.8. Evolutionary Stages and Tracks of Massive Stars	59
4.3. Supernovae	59
4.4. Binarity	62
4.4.1. Mass-loss in Binaries	63
4.4.2. Tides	64
4.4.3. Mass Transfer	64
4.4.4. Roche-lobe Overflow	65
4.4.5. Stability Criteria	65

Chapter	Page
4.4.6. Stable Mass Transfer	66
4.4.7. Common Envelopes	66
4.5. Formation Channels of Double Compact Objects	67
4.5.1. Field Formation	67
4.5.1.1. Common Envelope	67
4.5.1.2. Stable Mass Transfer	69
4.5.1.3. Chemically Homogenous Evolution	69
4.5.1.4. Population III Stars	69
4.5.2. Dynamical Formation	70
4.5.3. Active Galactic Nuclei Assisted	71
4.6. Detailed Stellar Evolution Codes	71
4.6.1. Rapid Population Synthesis	71
V. TRANSIENT GLITCH MITIGATION IN ADVANCED LIGO DATA WITH <i>GLITSCHEN</i>	76
5.1. Introduction	76
5.2. Method	79
5.2.1. Modeling the Advanced LIGO Noise Background	79
5.2.2. The Transient Glitch Background	81
5.2.3. The <i>glitschen</i> Model	82
5.2.4. Implementation and Performance	86
5.2.4.1. Selection of Training Data	86
5.2.4.2. Preprocessing and Training	87
5.2.4.3. Performance	88
5.3. Results	88
5.3.1. Testing with Maximum Likelihood Reconstruction	88
5.3.2. Sampling	92

Chapter	Page
5.3.3. Signal Safety Testing	92
5.3.4. GW190521: testing our model’s limits with the most massive (and glitch-like) confident O3a event	93
5.4. Conclusion and Future Work	95
5.5. Acknowledgements	98
5.6. Optimal Choice of the Model Dimensionality	99
VI. IMPLICATIONS OF MODERN MASS-LOSS RATES FOR MASSIVE STARS	100
6.1. Introduction	100
6.2. Methods	104
6.2.1. Winds of OB stars	105
6.2.2. Very massive stars	109
6.2.3. Red supergiant mass loss	112
6.2.4. Wolf–Rayet stars	119
6.3. Population synthesis results	122
6.3.1. Maximum black hole mass	122
6.3.2. Forming the most massive Galactic stellar mass BHs: Cyg X-1 and Gaia BH3	127
6.3.3. Impact on double compact objects	129
6.4. Discussion and conclusions	135
REFERENCES CITED	138

LIST OF FIGURES

Figure	Page
1. Cumulative detections as of the end of O3b, with 1 and 2 sigma contours of simulated catalogs in blue, and the actual cumulative detections in black. (The author of this dissertation generated an earlier version of this plot for a catalog paper). (Abbott et al., 2023)	36
2. The planned timeline of LVK observing runs (B. P. Abbott, 2020) . . .	36
3. The optical design of Advanced LIGO in 2014, at the start of the first Observing Run. (Aasi et al., 2015)	37
4. A diagram of the seismic isolation system, in which the test masses are suspended from finely tuned wires of silica (Aasi et al., 2015).	38
5. Major limiting terms in the noise curve of Advanced LIGO, at the outset of O1 (Aasi et al., 2015).	39
6. The amplitude spectral density (ASD) of the LIGO Hanford, Livingston, and Virgo detectors (Abbott et al., 2020b).	40
7. A plot of a time domain Inspiral, Merger, Ringdown (IMR) waveform for an $80M_{\odot}$ and $50M_{\odot}$ BBH coalescence (circular, non-precessing, aligned spins), generated using the IMRPhenomD (Khan et al., 2016) waveform, plotted using the open source gwpy (Macleod et al., 2021) and pycbc packages.	45
8. Test particle tracks in the Eggleton approximation to Roche radii. . . .	65
9. Typical loud blip (above) and tomte (below) glitches from the test set for Livingston in O3a, to demonstrate morphology. Q-scans indicate power as color in time-frequency pixels, and the timeseries (below in blue) shows additional morphology. Note that timescales and frequency ranges plotted vary. Blips are sometimes shorter than 5ms, where tomtes can last over 100ms.	81

Figure	Page
10. L1 O3a tomte glitch model eigenvectors. Increasing weight from top to bottom.	85
11. Frequency-domain residuals after subtraction from the test set (10%) reserved from each glitch type, detector, and epoch. The bins are scaled such that the lowest visible represent single samples from single glitches. Note that extremal samples are louder in Livingston. It has been observed that with greater sensitivity and range transient glitches become louder as well Soni et al. (2021).	90
12. H1 O3a test blip: full posterior estimation. Note the repeating blips afterward. This example shows the tendency of the sampler to converge on the loudest glitch available. The histogram of center time samples shows high certainty (just below the timeseries reconstruction). In the corner plot for the latent space weights (z_1 - z_5), we see that this test set glitch is typical of the class.	91
13. L1 O3a test tomte: full posterior estimation. This is a very typical tomte glitch, with all walkers converging on the same center time, low uncertainties in the timeseries reconstruction, and the posterior distribution aligning well with the distributions on the training set latent weights.	91
14. GW190521 Full Posterior Estimation, L1. The distribution in the center time is multi-modal, indicating that the glitch model fails to capture the full morphology of the signal (LALINFERENCE maxL in black), no matter where it is placed. The reconstruction features high uncertainty (samples in orange), and the posterior distribution in the latent variables lies outside the training set of glitches. All of this indicates that the model has failed to reconstruct GW190521 as a glitch, as expected.	96
15. GW190521 Full Posterior Estimation, H1	97
16. The relative Bayes factors as a function of dimensionality, q , for each detector and glitch type in the analysis. The peak of these curves allow for an automatic choice of dimensionality that avoids over-fitting.	99

17. Hertzsprung–Russell diagram, with evolutionary tracks color-coded by the dominant mass-loss type (distinct from “stellar type” in COMPAS). These tracks are generated using the new Merritt 2024 combination of mass loss prescriptions. The left panel shows solar metallicity ($Z = 0.0142$) tracks and the right panel shows tracks at the lower metallicity $Z = 0.001$. ZAMS mass is annotated at the start of the track. The final compact object type and mass (assuming the Mandel and Müller (2020) stochastic remnant mass prescription) are also annotated at the track’s end. The shaded region in the upper right corner of this diagram labelled ‘LBV regime’ denotes stars that are beyond the Humphreys and Davidson (1979) limit and stars whose tracks enter this region are assumed to experience LBV-like mass loss. 103
18. Terminal-age main-sequence (TAMS) mass M_{TAMS} as a function of the initial zero-age main-sequence (ZAMS) mass M_{ZAMS} . The three panels show the results for different metallicities: $Z=[0.03, 0.01, 0.001]$. The blue curve uses the Vink, de Koter, and Lamers (2001) prescription, the cyan curve uses the Vink and Sander (2021) prescription, the red curve uses the Krtićka and Kubát (2018) prescription and the green curve uses the Björklund, Sundqvist, Singh, Puls, and Najarro (2023). The previous default prescription is Vink et al. (2001). All prescriptions exhibit a strong metallicity dependence. The gray diagonal line indicates no main-sequence mass loss. Stars that exceed the Humphreys–Davidson limit may experience additional LBV mass loss already during core H burning, leading to a plateau at high mass; dashed lines have LBV winds turned off to demonstrate only the impact of main-sequence mass loss. 107
19. M_{TAMS} as a function of M_{ZAMS} for the three VMS mass-loss prescriptions described in Section 6.2.2. The three panels show the results for different metallicities: $Z = [0.03, 0.01, 0.001]$. The dotted lines show how VMS mass-loss treatment would proceed without the onset of LBV winds above the HD limit. The gray diagonal line shows $M_{\text{TAMS}} = M_{\text{ZAMS}}$, for no mass loss on the MS. 111

Figure	Page
20. Fraction of envelope mass remaining for massive stars during the RSG phase. The abscissa is the fractional time along the RSG phase, whilst the ordinate is normalized to the envelope mass at the start of the RSG phase. The solid lines use our standard RSG prescription (Decin, Richards, Marchant, & Sana, 2024), whilst the dashed curves use the prescription from Yang et al. (2023). The colors denote the initial (ZAMS) mass of the stars in solar masses, as labeled in the legend. Solar metallicity is assumed.	117
21. Mass-loss rate as a function of luminosity for RSGs according to the various prescriptions discussed in this paper. For prescriptions that are dependent on mass, we assume a mass of $15 M_{\odot}$ for visualization purposes. For NJ90, solar metallicity and a surface temperature of 4000 K is assumed. Kee, Sundqvist, Decin, de Koter, and Sana (2021) is not included, because rates vary over four orders of magnitude given reasonable choices of the turbulent velocity. None of the implemented prescriptions have direct metallicity dependence. [Incorrect for NJ90, which should be defined on first use.]	118
22. Mass-loss rates of WR stars as a function of luminosity at solar metallicity. The dashed black line shows the previous prescription in COMPAS (Belczynski et al., 2010; Hamann, Koesterke, & Wessolowski, 1995; Vink & de Koter, 2005). The dotted blue curve shows the mass-loss prescription from Vink (2017). The solid red curve shows the mass-loss prescription for massive WR stars from A. A. C. Sander and Vink (2020), without applying the temperature correction from A. A. C. Sander et al. (2023). As discussed in Section 6.2.4, in COMPAS we use the maximum of the Vink (2017) prescription and the A. A. C. Sander and Vink (2020) prescription with the temperature correction applied (cf. Equation 6.11). The blue curve shows the correction applied at an effective temperature of 120,000 K. The dashed purple curve shows the Shenar et al. (2019) mass-loss prescription.	121
23. Initial-final total and core mass relation for single massive stars. The top panel shows the relation for $Z = 0.03$ and the bottom panel for $Z = 0.0001$, the highest and lowest metallicities modeled in COMPAS, respectively.	124

24. Maximum black hole mass formed from a single star as a function of metallicity. The blue line shows the result using the previous wind prescription in COMPAS (Belczynski et al., 2010). The green line shows the updated result using the new default combinations of wind prescriptions implemented in this work. The orange line shows a pessimistic choice of mass-loss prescriptions that lead to increased mass loss and typically lower black hole masses. All models use the Mandel and Müller (2020) remnant mass prescription. The maximum black hole mass at low metallicity ($Z \lesssim 10^{-3}$) for the **BELCZYNSKI2010** and **MERRITT2024** models is set by pair instability supernovae, implemented according to Hendriks, van Son, Renzo, Izzard, and Farmer (2023). The yellow cross and star show the mass and metallicity estimate for the black hole in Cyg X-1 (Miller-Jones et al., 2021), while the leftward teal line shows the mass and metallicity for Gaia BH3 (Panuzzo et al., 2024). LMC and SMC metallicity are assumed to be 0.5 and 0.2 of solar, respectively, Vink et al. (e.g. 2023). 126
25. Formation rates of merging BBHs per star forming mass as a function of metallicity. The different colored lines denote our different sets of mass-loss prescriptions (see Table 11). The shaded region around each line indicates the sampling uncertainty, as estimated through bootstrapping. The blue line shows the previous default model (**BELCZYNSKI2010**: Belczynski et al., 2010; Riley et al., 2022b), the orange line shows the **PESSIMISTIC** model and the green line shows our new default model (**MERRITT2024**). 130
26. Maximum total mass of merging BBHs as a function of metallicity, as distinct from final mass which would account for energy lost in GWs. The vertical dashed lines denote solar metallicity, and that of the Large and Small Magellanic Clouds. The horizontal dashed red line denotes the total mass of GW150914, with the median sample, and 90% credible intervals filled (Abbott et al., 2016a), illustrating that such high-mass BBHs are expected to form only in low-metallicity environments in these models. 132

27.	Projected detections of BBH binned by chirp mass and redshift, assuming sensitivity of the third observing run (O3) of LVK, with a detection threshold SNR of 8. Updating winds creates an excess near a chirp mass of $10 M_{\odot}$, and lowers the density at $25\text{--}45 M_{\odot}$. Blue=BELCZYNSKI2010, Orange=PESSIMISTIC, Green=MERRITT2024.	133
-----	---	-----

LIST OF TABLES

Table	Page
1. IGEC resonant-bar gravitational wave detectors and their capabilities. . .	33
2. Summary of Stellar Timescales	58
3. Internal structure, fusion regime, and evolutionary outcomes for stars of various masses (Chabrier & Baraffe, 1997; Woosley, Heger, & Weaver, 2002)	59
4. Stellar phases and abbreviations used, adapted from Riley, Stevenson, et al. (2022).	60
5. Properties of nuclear burning stages in a $15 M_{\odot}$ star (Woosley et al., 2002).	61
6. Summary of stellar end states by ZAMS mass and core conditions, adapted from COMPAS (Riley, Agrawal, et al., 2022), with core temperatures and burning stages informed by stellar evolution models (e.g., Woosley et al. 2002).	62
7. Comparison of Dimensionality in Stellar Modeling Codes. 1-D: Kippenhahn, Weigert, and Weiss (2012); Paxton, Bildsten, Dotter, and et al. (2011); Paxton, Cantiello, Arras, and et al. (2013), Heger2000	72
8. Summary of Major Binary Population Synthesis Codes	75
9. Selecting short duration, heavy BBH mergers we provide an important test for the model, which should give lower SNRs than the CBC model. Events are in order of detector frame chirp mass ($\mathcal{M}_{\text{det}}, M_{\odot}$). For all of these events we see lower SNRs by a factor of 2-3, whereas we expect to recover nearly all of the SNR in confirmed glitches. CBC parameter estimation results from et.al. (2021).	94
10. Running samplers on these events, we obtain the DIC from our distributions of log likelihoods. The deviance information criterion (DIC) favors models with a lower value. The CBC model is highly preferred to the glitch model in all cases, indicating that pass the signal safety test.	94

Table	Page
11. Sets of mass-loss prescriptions used in this paper, where the columns are evolutionary phases.	102

CHAPTER I

INTRODUCTION

The theory of General Relativity brought about a new era for physics in the 20th century, describing gravity not as a force, but as a property of the curvature of space-time, and after passing test after test, it has enabled a nascent field of physics in the 21st century: gravitational wave (GW) astronomy. Between 2015 and 2025, the catalog of confidently detected compact binary mergers has expanded to well over 100.

There is only so much we can learn from single events detected in gravitational waves only. I like to use the analogy of hearing a car crash around the block with no visual information, and trying to reconstruct the make, model, velocity, etc. of each vehicle, and even place a confidence level on who was at fault. Given a multi-messenger detection with an electromagnetic counterpart, we can make much more significant conclusions. But given a large number of events with limited conclusions for each, we can place confidences on the overall properties of a population. Work on modelling and mitigating glitches in the detectors took novel approaches to improve this new science.

I developed a novel technique with *Transient glitch mitigation in Advanced LIGO data with glitches*, where I was lead author. Before this, I fulfilled LIGO (Laser-Interferometer Gravitational-Wave Observatory) collaboration duties including Parameter Estimation rota, where a small group is assigned to perform astrophysical parameter estimation on new events as the data is collected. This led to small contributions to catalog papers, with co-authorship with the LIGO Scientific Collaboration, and minor model-testing contributions to *Constraining*

Unmodeled Physics with Compact Binary Mergers from GWTC-1, with lead authorship by Bruce Edelman (not described directly here).

As the catalog expands, the opportunities for population statistics, and conclusions that place constraint on the astrophysics of formation channels can be realized. From this other, astrophysical perspective, we approach the same problem of understanding binary black hole mergers, with a survey of stellar winds to improve population synthesis codes. I will share my contributions (lead author, survey of stellar winds models, implementation and testing in the code) to the paper *Implications of modern mass-loss rates for massive stars*, where I worked most closely with Simon Stevenson on all aspects of background research and code development, was introduced to the collaboration and the project by Ilya Mandel, used code primarily written by Jeff Riley, and received expert theoretical advice on the physics of stellar winds from Andreas Sander. This work centered on exploring the impact of metallicity on the final outcomes for massive systems, and found use in *Not Just Winds: Why Models find Binary Black Hole Formation is Metallicity Dependent, While Binary Neutron Star Formation is Not*, with lead author Lieke Van Son (not described directly here).

To establish necessary background, we will frame the work we have done and acknowledge the immense progress thus far in disparate fields. We will begin by outlining the basics of General Relativity, up to the propagation, emission, and detection of gravitational waves, with several illustrative examples.

We will then discuss the basics of gravitational wave detectors, giving enough background to motivate the developments of novel glitch models that can be used in parameter estimation, specifically targeting an unexplained class of

transient glitches that are problematic for searches for high mass binary black hole mergers.

We will then establish some principles of stellar evolution, as they affect massive stellar populations that lead to compact binary mergers, with a focus on mass-loss through stellar winds, and what this reveals about the environments and processes that are capable of forming binary black holes that merge in a Hubble time.

CHAPTER II

GENERAL RELATIVITY

2.1 Gravitational Waves and General Relativity

On September 14, 2015 the LIGO detectors recorded (Abbott et al., 2016b) the first direct detection of gravitational waves, ending a global effort by hundreds of scientists nearly a hundred years after gravitational waves were predicted by Albert Einstein's theory of general relativity. A more complete description of general relativity can be found in many classic references including Hartle (2003); Misner, Thorne, and Wheeler (1973). Examples given here follow Palamos (2020).

In Newtonian gravity ρ creates a gravitational field Φ

$$\nabla^2\Phi = 4\pi G\rho$$

which results in a force felt by massive particles

$$\vec{F} = -m\vec{\nabla}\Phi.$$

Trajectories are then calculated using Newton's law of motion.

In Einsteinian gravity, matter and energy curve spacetime according to the Einstein field equations (Einstein, 1915)

$$G_{\alpha\beta} = 8\pi GT_{\alpha\beta}. \tag{2.1}$$

Particles then follow geodesics in this curved geometry:

$$\frac{d^2x^\alpha}{dt^2} = -\Gamma_{\mu\nu}^\alpha \frac{dx^\mu}{dt} \frac{dx^\nu}{dt} \tag{2.2}$$

where (2.2) is the geodesic equation and the coefficients $\Gamma_{\mu\nu}^\alpha$, known as Christoffel symbols, are defined in terms of the metric and its derivatives as

$$g_{\alpha\delta}\Gamma_{\beta\gamma}^\delta = \frac{1}{2} \left(\frac{\partial g_{\alpha\beta}}{\partial x^\gamma} + \frac{\partial g_{\alpha\gamma}}{\partial x^\beta} - \frac{\partial g_{\beta\gamma}}{\partial x^\alpha} \right).$$

The metric tensor (or simply *metric*), $g_{\alpha\beta}$, is the fundamental mathematical object encoding the geometry of spacetime and provides the notion of a line element in some coordinate system $\{x_\alpha\}$ as

$$ds^2(x) = g_{\alpha\beta}(x)dx^\alpha dx^\beta.$$

The relationship between spacetime curvature and matter energy density is given to us in Einstein's equation (2.1) here written in natural units (without a cosmological constant). The $G_{\alpha\beta}$ term on the left hand side is known as the Einstein tensor and depends entirely on the metric, $g_{\alpha\beta}$, which determines the curvature of spacetime. On the right hand side, $T_{\alpha\beta}$ is commonly known as the *stress-energy tensor* which defines any matter and/or energy that may be present. The proportionality constant can be determined by requiring that Newtonian gravity is recovered in the weak field, slow motion regime.

In practice, solving the Einstein equations is prohibitively difficult. Relating 4x4 symmetric tensors, they become a system of ten coupled nonlinear partial differential equations (PDEs). Often, solutions are found with the aid of symmetries, in the weak field limit, or with numerical methods. The possibility for gravitational waves emerges under the assumptions of linearized gravity, where curvature is introduced as a small perturbation to a flat spacetime, which will be explored next.

2.1.1 Linearized Gravitational Waves. The left side of Einstein's field equations can be written as

$$G_{\alpha\beta} = R_{\alpha\beta} - \frac{1}{2}g_{\alpha\beta}R \tag{2.3}$$

where $R_{\alpha\beta}$ is the Ricci tensor and R is the Ricci scalar. The Ricci tensor depends on the metric through the connection

$$R_{\alpha\beta} = \frac{\partial\Gamma_{\alpha\beta}^{\gamma}}{\partial x^{\gamma}} - \frac{\partial\Gamma_{\alpha\gamma}^{\beta}}{\partial x^{\beta}} + \Gamma_{\alpha\beta}^{\gamma}\Gamma_{\gamma\delta}^{\delta} - \Gamma_{\alpha\delta}^{\gamma}\Gamma_{\beta\gamma}^{\delta}$$

and the Ricci scalar is the contraction $R = g^{\alpha\beta}R_{\alpha\beta}$.

To simplify the problem enough to show the existence and propagation of waves, we can take $g_{\alpha\beta}$ to be the flat Minkowski metric $\eta_{\alpha\beta}$ plus a small perturbation $h_{\alpha\beta}$

$$g_{\alpha\beta} = \eta_{\alpha\beta} + h_{\alpha\beta}$$

and discard higher powers of $h_{\alpha\beta}$ present in subsequent equations. To first order in h the Christoffel symbols become

$$\Gamma_{\alpha\beta}^{\gamma} = \frac{1}{2}\eta^{\gamma\delta}\left(\frac{\partial h_{\alpha\delta}}{\partial x^{\beta}} + \frac{\partial h_{\beta\delta}}{\partial x^{\alpha}} - \frac{\partial h_{\alpha\beta}}{\partial x^{\delta}}\right).$$

We can insert that into the expression above for the Ricci tensor and after some cancellations arrive at

$$R_{\alpha\beta} = \frac{1}{2}\left(\frac{\partial^2 h_{\beta}^{\gamma}}{\partial x^{\gamma}\partial x^{\alpha}} - \eta^{\gamma\delta}\frac{\partial^2 h_{\alpha\beta}}{\partial x^{\gamma}\partial x^{\delta}} - \frac{\partial^2 h_{\gamma}^{\alpha}}{\partial x^{\beta}\partial x^{\alpha}} + \frac{\partial^2 h_{\alpha}^{\gamma}}{\partial x^{\beta}\partial x^{\gamma}}\right).$$

The Ricci scalar can be calculated from $R = g^{\alpha\beta}R_{\alpha\beta} = \eta^{\alpha\beta}R_{\alpha\beta} + O(h^2)$

$$R = \frac{\partial^2 h^{\alpha\beta}}{\partial x^{\alpha}\partial x^{\beta}} - \eta^{\alpha\beta}\frac{\partial^2 h_{\gamma}^{\alpha}}{\partial x^{\alpha}\partial x^{\beta}}.$$

With the linearized Ricci tensor and scalar, we compute the linearized Einstein tensor using equation 2.3:

$$G_{\alpha\beta} = \frac{1}{2}\left(\frac{\partial^2 h_{\beta}^{\gamma}}{\partial x^{\gamma}\partial x^{\alpha}} - \eta^{\gamma\delta}\frac{\partial^2 h_{\alpha\beta}}{\partial x^{\gamma}\partial x^{\delta}} - \frac{\partial^2 h}{\partial x^{\beta}\partial x^{\alpha}} + \frac{\partial^2 h_{\alpha}^{\gamma}}{\partial x^{\beta}\partial x^{\gamma}}\right) - \frac{1}{2}\eta_{\alpha\beta}\left(\frac{\partial^2 h^{\alpha\beta}}{\partial x^{\alpha}\partial x^{\beta}} - \eta^{\alpha\beta}\frac{\partial^2 h}{\partial x^{\alpha}\partial x^{\beta}}\right).$$

The expression can be simplified with the substitution

$$\bar{h}_{\alpha\beta} := h_{\alpha\beta} - \frac{1}{2}\eta_{\alpha\beta}h,$$

where $\bar{h}_{\alpha\beta}$ is known as the trace-reversed metric perturbation because $\bar{h} = \eta^{\alpha\beta}\bar{h}_{\alpha\beta} = -h$. This way, the linearized Einstein tensor becomes

$$G_{\alpha\beta} = \frac{1}{2} \left(\frac{\partial^2 \bar{h}_\beta^\gamma}{\partial x^\gamma \partial x^\alpha} - \eta^{\gamma\delta} \frac{\partial^2 \bar{h}_{\alpha\beta}}{\partial x^\gamma \partial x^\delta} - \eta_{\alpha\beta} \frac{\partial^2 \bar{h}^{\gamma\delta}}{\partial x^\gamma \partial x^\delta} + \frac{\partial^2 \bar{h}_\alpha^\gamma}{\partial x^\beta \partial x^\gamma} \right)$$

which we then use to write the linearized Einstein field equations as

$$\frac{\partial^2 \bar{h}_\beta^\gamma}{\partial x^\gamma \partial x^\alpha} - \eta^{\gamma\delta} \frac{\partial^2 \bar{h}_{\alpha\beta}}{\partial x^\gamma \partial x^\delta} - \eta_{\alpha\beta} \frac{\partial^2 \bar{h}^{\gamma\delta}}{\partial x^\gamma \partial x^\delta} + \frac{\partial^2 \bar{h}_\alpha^\gamma}{\partial x^\beta \partial x^\gamma} = 16\pi G T_{\alpha\beta}.$$

With a careful choice of coordinates we further simplify. In a procedure common in electromagnetism, we impose a gauge condition on the metric perturbation

$$\frac{\partial \bar{h}^{\alpha\beta}}{\partial x^\beta} = 0. \quad (2.4)$$

Equation 2.4 defines the *Lorenz gauge* and in that gauge the linearized Einstein equation takes the simple form:

$$-\square \bar{h}_{\alpha\beta} = 16\pi G T_{\alpha\beta} \quad (2.5)$$

where \square is flat-space wave operator (or d'Alembertian) and $\square \bar{h}_{\alpha\beta} = \eta^{\gamma\delta} \frac{\partial^2 \bar{h}_{\alpha\beta}}{\partial x^\gamma \partial x^\delta}$ since mixed derivatives do not appear for the Minkowski metric. With 2.5 we have linearized Einstein field equations in the Lorenz gauge, reducing to a wave equation for the perturbation with the stress-energy tensor as a source. Thus we have gravitational waves.

To explore properties of these waves, consider equation 2.5 in vacuum

$$-\square \bar{h}_{\alpha\beta} = 0 \quad (2.6)$$

with plane wave solutions of the form $\bar{h}_{\alpha\beta} = A_{\alpha\beta} e^{ik_\gamma x^\gamma}$ where $A_{\alpha\beta}$ is known as the polarization tensor and k_γ the wave vector. For this solution to solve (2.6) the wave vector must satisfy

$$k_\gamma k^\gamma = 0.$$

Typically k_γ is referred to as a null vector, and thus gravitational waves travel at the speed of light.

Due to the Lorenz gauge condition (2.4) the constant $A_{\alpha\beta}$ must satisfy

$$A^{\alpha\beta}k_\beta = 0. \tag{2.7}$$

The tensor $A^{\alpha\beta}$ initially had ten independent components, since it is a symmetric 4×4 tensor. The condition 2.7 (which is equivalent to four equations) reduces that to six independent components. We can further exploit arbitrary coordinate transformations of the form

$$x'^\alpha = x^\alpha + \xi^\alpha(x)$$

which are still allowed provided ξ^α respects (2.4) implying

$$\square\xi_\alpha = 0.$$

This gives four more conditions, and thus the metric perturbation only has 2 remaining independent degrees of freedom. These final gauge conditions can be chosen to impose the following constraints:

$$A_{\alpha\beta}x^\beta = 0$$

$$A_\alpha^\alpha = 0$$

which specify the so-called *transverse traceless* gauge (TT). As the name implies, when working in this gauge the polarization tensor is traceless and all non-zero terms are in the transverse direction. So if we have a plane gravitational wave propagating in the z-direction and write the polarization tensor in matrix form it

would look like:

$$\begin{pmatrix} 0 & 0 & 0 & 0 \\ 0 & A_{11} & A_{12} & 0 \\ 0 & A_{12} & -A_{11} & 0 \\ 0 & 0 & 0 & 0 \end{pmatrix}.$$

These two independent polarizations are commonly referred to as the “plus” and “cross” polarizations of gravitational radiation. To explore the observable effect of the polarizations, we can examine a ring of test particles in the xy plane. A gravitational wave in the plus polarization traveling in the z -direction will alternately stretch and compress space in the x and y directions. The cross polarization is similar but rotated by 45° .

Now that we have explored how the propagation of these waves emerges from basic predictions of General Relativity, we will examine sources.

2.2 Production and Sources of GWs

We will describe the production of gravitational waves by astrophysical sources, beginning with an analogy from Misner et al. (1973) between gravitational and electromagnetic radiation, via the multipole expansion.

GW power can be roughly estimated in analogy to electromagnetic radiation by substituting the electric charge e with the mass in the source term. The dominant term for electromagnetic radiation is the dipole: power radiated by a source with dipole moment p is proportional to \ddot{p}^2 . In gravitation, an analogous term would be a “mass dipole” moment which is $p_{mass} = \sum_n m_n x_n$. The first derivative of the mass dipole is the total linear momentum. Due to the conservation of momentum, the second derivative is zero, therefore the dipole term cannot contribute to gravitational radiation. The next term in the electromagnetic case

corresponds to the magnetic dipole. The gravitational analog to the magnetic dipole is the angular momentum which is also conserved and therefore also does not contribute to the radiated power. The electric quadrupole radiates with power

$$P_{EM} \sim \ddot{Q}_{ij} \ddot{Q}_{ij}$$

where Q_{ij} is the electric quadrupole tensor and summation is implied over the latin indicies. Finally, there is no reason for the mass quadrupole to be conserved and we can conclude that power radiated in GWs depends on the time-varying quadrupole moment of the source.

The linearized Einstein field equations can be solved with a source using the method of Green's functions (analogously to electromagnetism). For slow moving sources, and in the far field regime, the perturbation in the TT gauge becomes Hartle (2003)

$$h_{ij}^{TT}(t, x) \simeq \frac{2G}{c^4 r} \ddot{I}_{ij}^{TT}(t - r/c) \quad (2.8)$$

where the quadrupole tensor, $I_{ij}^{TT}(t)$ is defined as:

$$I^{ij}(t) = \int x^i x^j \rho(t - r/c, x) d^3x.$$

Since the GW strain depends on a changing quadrupole moment, it follows that no gravitational radiation can be produced by spherically symmetric expansion or axially symmetric rotation. Using 2.8 for h_{ij}^{TT} we find an order of magnitude estimate for the strength of a GW, following (Schutz, 1985). For motion inside a highly non-spherical source, the usual component of \ddot{I}_{ij} can be approximated as

$$\ddot{I} = Mv_{N.S.}^2.$$

where $v_{\text{N.S.}}$ is the non-spherical part of the velocity inside the source. By the virial theorem

$$v_{\text{N.S.}} \sim \frac{GM}{2R}$$

where R is the source size. So the equation for the strength of a GW becomes

$$h \sim \frac{GM}{rc^2} \frac{GM}{Rc^2}.$$

Notably, the first term looks like the Newtonian potential of the far-field source and the second term looks like the Newtonian gravitational potential at the source. If we take the parameters of the famous Hulse-Taylor binary pulsar PSR B1913+16 (of the 1993 Nobel Prize), we end up with an approximate amplitude of

$$h \sim \frac{G (2.8 m_{\odot})}{(8 \text{ kpc}) c^2} \frac{G (2.8 m_{\odot})}{(4.8 R_{\odot}) c^2} \sim 2 \times 10^{-23}.$$

As a rough order of magnitude estimate, this illustrates the incredible sensitivity necessary to detect gravitational waves from Earth. At present, this system is radiating far below the sensitive frequency range of current ground-based GW detectors, with an orbital period of 7.75hr and an estimated 10^8 years until coalescence, when the highly nonlinear final inspiral will emit GWs that sweep upward in frequency.

2.3 Astrophysical Sources

In ground based laser interferometry, the primary method for detecting GW, sources are usually divided into the following four categories: coalescing compact binaries (CBCs), bursts, continuous waves (CWs), and stochastic signals.

2.3.1 Bursts. Searches for unmodeled bursts are vital, given that using only specifically templated searches for known waveforms may blind us to the discoveries of new phenomena, which is certainly one of the greatest motivators in science. The expectation of a signal of any arbitrary form, which must only be

coherent between detectors, motivates a more model-agnostic class of searches. As of yet there have been no significant candidates not explained as noise/glitches or CBCs, but burst search pipelines operate differently and sometimes recover novel CBC events overlooked by traditional templated searches (Abbott, others (LIGO Scientific Collaboration, & Collaboration), 2024)

2.3.2 Continuous Waves. Continuous waves are generated by many nearby galactic sources, and while no evidence for a signal has yet been found (Abac & Abbott, 2025), some nearby young pulsars may be good candidates, and a detection would provide information on their internal structure as well as a novel test of GR.

2.3.3 Stochastic Signals. Stochastic signals are expected to be a background of continuous emitters, mergers (CBCs) including supermassive black holes (et al. (LIGO Scientific Collaboration & Collaboration), 2019), and the theorized primordial background from early universe processes such as the big bang (Caprini & Figueroa, 2018), inflation, possible phase transitions, and cosmic strings (Abbott, others (LIGO Scientific Collaboration, & Collaboration), 2021).

Which of these background processes may dominate varies depending on the frequency band, and some may be detectable by LISA or pulsar timing arrays.

2.3.4 Coalescing Compact Binaries. The focus of this work is on the astrophysics of binary black hole inspirals, and their formation. Waveforms are discussed in the detection section.

CHAPTER III

DETECTION OF GRAVITATIONAL WAVES

Thus far, as of 2025, all gravitational wave detections have been via ground-based interferometry. By many measures these are the most sensitive devices ever constructed, measuring changes in arm length to one part in 10^{24} . There is no shortage of analogy or metaphor, apt and less apt, for communicating just how small of an effect that is. What is more impressive to consider is the human story that brought us these detections. The expertise and engineering necessary, over decades and by thousands of experts, to design, construct, and operate the detectors is immense, and beyond the scope of this dissertation. We will explore the instruments and their history in sufficient detail to motivate the construction of novel models for glitch mitigation, and to understand how instrumental effects are accounted for in astrophysical catalogs and population inference.

3.1 History of Gravitational Wave Detectors

We are now entering the second decade of gravitational wave astronomy. Of course, the story started with the predictions of General Relativity more than a century ago, and continued with the confirmation of theory through the observation of the effects of gravitational radiation on the orbital evolution of compact binaries (binaries with a pulsar).

3.1.1 Resonant Bar Detectors. There is, however, an interesting and little known history of attempts to directly detect gravitational waves beginning long before the technology and nature would allow. Famously, in the 1960s, Joseph Weber was inspired to use resonant-mass antennas (Weber, 1960), large aluminum cylinders weighing tons, and tuned to vibrate at certain resonant modes in the kilohertz regime. If a gravitational wave were to pass through the bar,

it should ring-up quadrupolar oscillations. Weber used piezoelectric readout sensors to detect these. Famously, Weber claimed the detection of gravitational waves in 1969 and 1970 (Weber, 1969), via coincident signals in multiple resonant bar detectors. One was in College Park, Maryland and the other was in Chicago, about 1000 km away. Current estimates place the strain sensitivity of these devices at about 10^{-16} , with thermal, seismic, and electronic limitations all coming into play. As multiple independent efforts failed to reproduce his results, the claim became controversial. However his work paved the way for future cryogenic bar detector efforts in the 1980s and 1990s. Major advances brought the resonant bar technique remarkably closer to the astrophysical detection threshold, with cryogenic cooling, SQUID (Superconducting Quantum Interference Devices) and other ultra low-noise amplification techniques increasing sensitivity by many orders of magnitude. The effort was orchestrated on multiple continents, with the International Gravitational Event Collaboration (IGEC) looking for coincident bursts. This consortium provided a precedent for the global LIGO-Virgo-Kagra (LVK) collaboration.

Detector	Location	Operating Period	Temp (K)	Strain h	Notes
EXPLORER	CERN, Switzerland	1980s-2000s	2.0	$\sim 10^{-19}$	First large-scale European bar; operated with NAUTILUS (de Waele et al. (1993))
NAUTILUS	Frascati, Italy	1995-2016	0.1	$\sim 10^{-20}$	Ultra-cooled bar to 0.1 K; part of IGEC network (Astone et al. (2001))
AURIGA	Legnaro, Italy	1997-present	4.2	$\sim 10^{-20}$	Suspended bar with capacitive readout; cryogenic operation (Astone et al. (1997))
ALLEGRO	Louisiana, USA	1991-2007	4.2	$\sim 10^{-19}$	Coincidence studies with LIGO Livingston (Astone et al. (2001))
NIOBE	Perth, Australia	1993-2001	2.6	$\sim 10^{-19}$	Used niobium bar for superconducting properties (Astone et al. (2001))

Table 1. IGEC resonant-bar gravitational wave detectors and their capabilities.

Ultimately, there are a few inherent limitations of the resonant bar technique: narrow bandwidth means that they will ring up only through part of an astrophysical signal, many of which sweep through a large range of frequencies.

They also have weak angular resolution and no sensitivity to polarizations as in interferometers. Notably, AURIGA has continued to operate and improve its capabilities, with strain reaching better than 2×10^{-21} , in a 100 Hz band around 1 kHz (Branca et al., 2017), which has been used to place limits on certain Dark Matter candidates.

3.1.2 History of Interferometric Detectors. In 1962 Soviet physicists Mikhail Gertsenshtein and Vladimir Pustovoit first proposed the use of laser interferometry to detect gravitational waves (Gertsenshtein & Pustovoit, 1963). In 1971, Robert L. Forward built a table-top interferometer to validate the concept, with 2-meter arms (Forward, 1978). To pursue the goal of astrophysical detection, long baselines would be necessary. In 1972, Rainer Weiss laid out the need for kilometer-scale baselines, attention to seismic, thermal, and quantum noise limitations, and in doing so made a proposal that would meet the expected gravitational wave amplitude from astrophysical sources (Weiss, 1972). In the 80s, prototypes and technological demonstrations, especially at MIT, Caltech, Garching, and Glasgow continued to improve. In 1984 Caltech and MIT signed an agreement on the joint design and construction of LIGO, or the Laser Interferometer Gravitational-wave Observatory. LIGO was originally proposed by Kip Thorne, Ronald Drever, and Rainier Weiss, and approved for funding in 1992 (Weiss, Drever, & Thorne, 1992). Construction began in 1994, commissioning from 1999-2002, and early searches in 2002-2005 Saulson (2003). One of the key approaches that enabled LIGO's eventual success was a two-stage approach: build an initial detector at scale based on proven technology, test it extensively and then upgrade it with technologies that in some cases did not exist at the outset, giving each run a higher probability of detecting gravitational waves.

3.2 Direct Detections of Gravitational Waves

The first observing run (O1) of Advanced LIGO (Abbott, others (LIGO Scientific Collaboration, & Collaboration), 2016a) yielded direct detections of the merger of binary black holes (BBH), beginning with GW150914 (Abbott et al., 2016), for which the 2017 Nobel Prize in Physics (The Royal Swedish Academy of Sciences, 2017) was awarded. The first binary neutron star (BNS) merger (Abbott et al., 2017) and an electromagnetic counterpart (B. P. Abbott, 2017) in the form of a kilonova were detected in O2. O3 brought two neutron star-black hole coalescences (NSBH) (Abbott et al., 2021). By the end of O3 there were over 90 strong candidates, and going into O4 with even greater sensitivity and more observations we can make astrophysical inferences that constrain the population, elucidate extreme regimes of unknown physics, and provide an independent method for performing cosmology. Currently, the LSC (LIGO Scientific Collaboration) includes more than 1,000 scientists from more than 100 institutions and 18 countries.

3.3 Interferometric Detector Design

The instruments are specialized versions of a Michelson interferometer with 4km long arms (Aasi et al., 2015). Fabry-Perot cavities are used in the arms, power-recycling means that a photon makes many round trips between the test masses, with 125W at input and 75kW circulating in the arms.

Achieving a vacuum better than that of space requires a multi-month process of slowly removing the last atoms within. The test masses are suspended on seven successive layers of seismic isolation, and are calibrated with photon pressure, and now with the newtonian gravitational pull of small 1kg rotor nearby (Ross et al., 2021), just to demonstrate how finely balanced the test masses are.

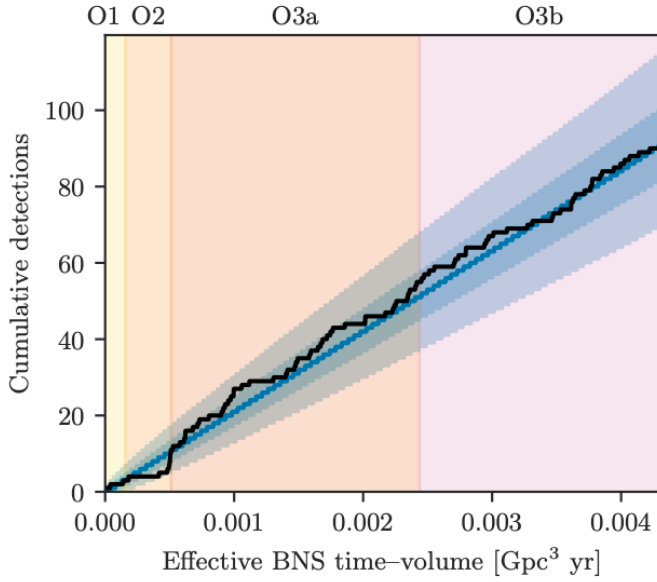


Figure 1. Cumulative detections as of the end of O3b, with 1 and 2 sigma contours of simulated catalogs in blue, and the actual cumulative detections in black. (The author of this dissertation generated an earlier version of this plot for a catalog paper). (Abbott et al., 2023)

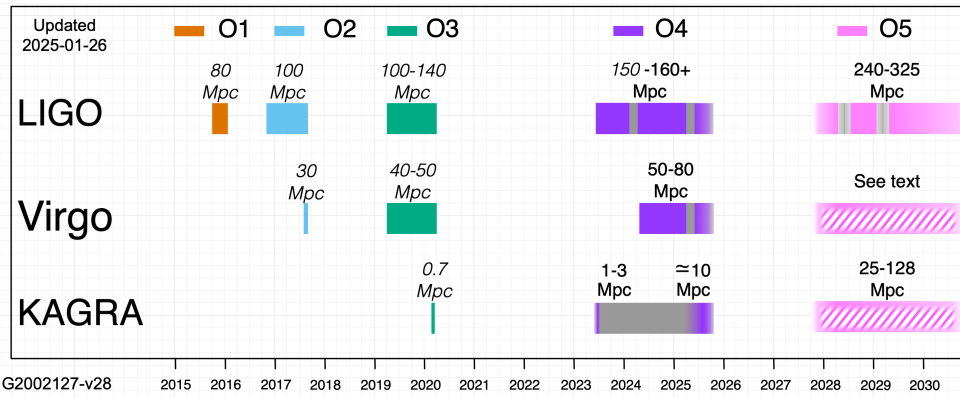


Figure 2. The planned timeline of LVK observing runs (B. P. Abbott, 2020)

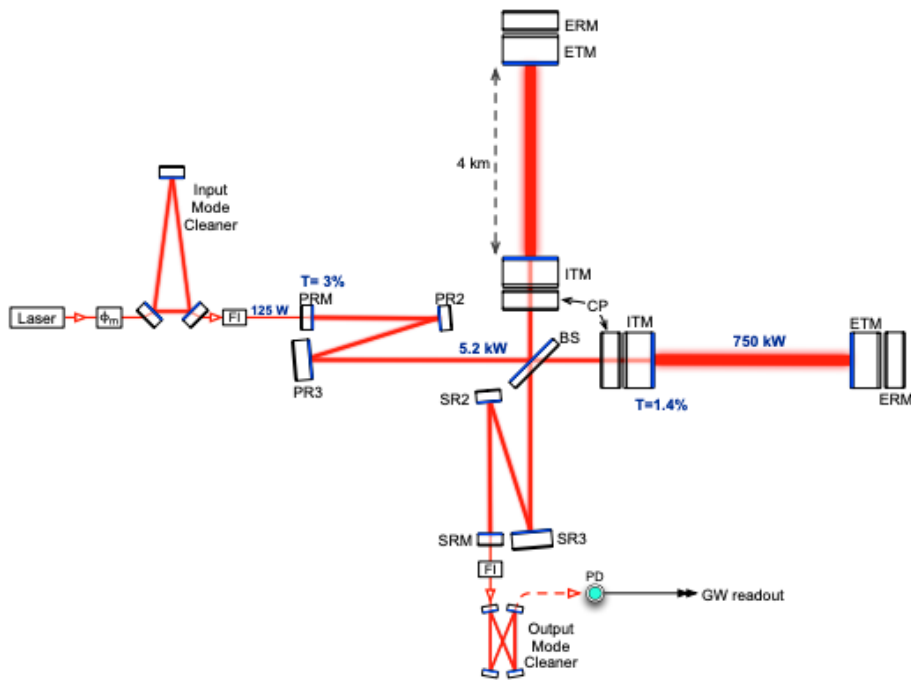


Figure 3. The optical design of Advanced LIGO in 2014, at the start of the first Observing Run. (Aasi et al., 2015)

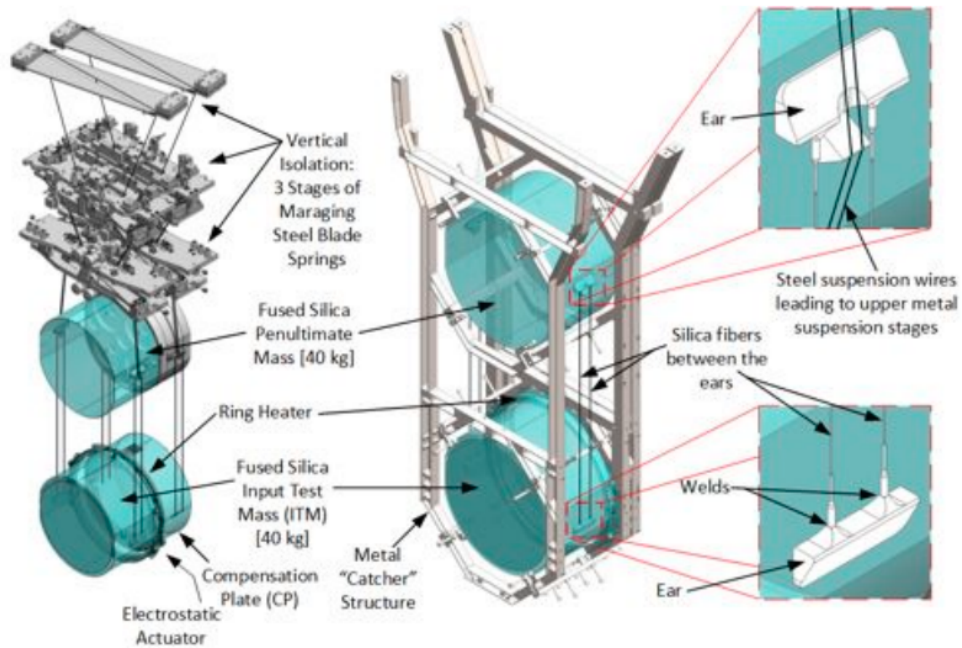


Figure 4. A diagram of the seismic isolation system, in which the test masses are suspended from finely tuned wires of silica (Aasi et al., 2015).

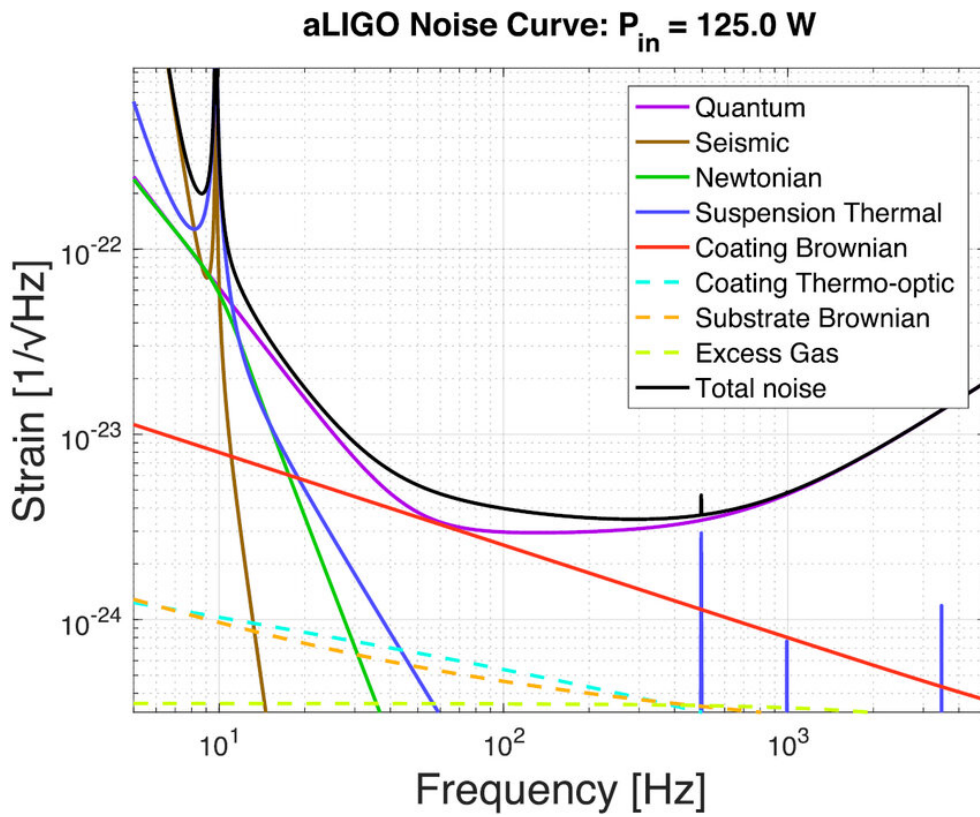


Figure 5. Major limiting terms in the noise curve of Advanced LIGO, at the outset of O1 (Aasi et al., 2015).

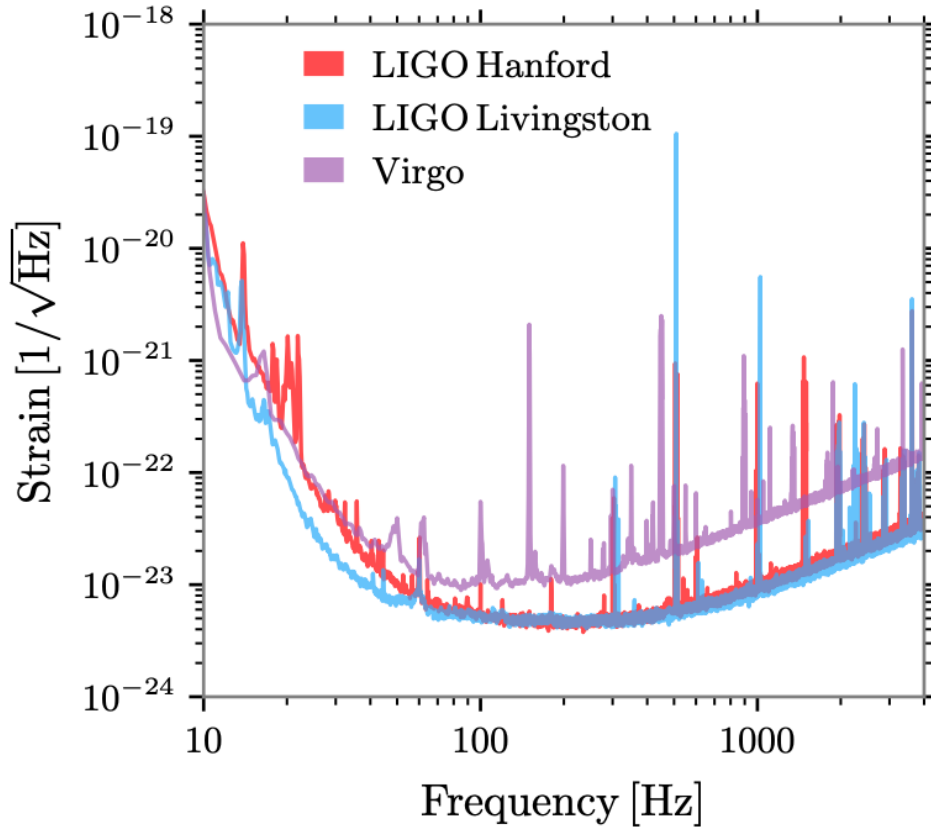


Figure 6. The amplitude spectral density (ASD) of the LIGO Hanford, Livingston, and Virgo detectors (Abbott et al., 2020b).

3.4 Analysis of Gravitational Wave Data

With Abbott et al. (2020a) and Abbott, Abbott, et al. (2021) the collaboration provides an excellent overview of analysis techniques, and open data with which to replicate their analyses.

3.4.1 Noise Model. There will be a brief discussion of the properties of LIGO noise so as to motivate the use of novel mitigation techniques for unexplained transient noise sources.

3.5 Basic Properties of Detector Noise

There is an excellent review of the noise in the LIGO detectors in Abbott et al. (2020b). The idealized noise in the strain channel can be modelled as a stochastic process with statistical properties given by a joint probability distribution, $p(\mathbf{n})$.

The estimated mean of the noise time series:

$$\hat{\mu} = \frac{1}{N} \sum_{i=1}^N n_i \quad (3.1)$$

Where $N = \dim(\mathbf{n})$ is the number of data samples. The sample covariance matrix:

$$\hat{C}_{ij} = \frac{1}{M-1} (n_i - \hat{\mu})(n_j - \hat{\mu}) \quad (3.2)$$

Estimates of covariance can only be made, if noise is assumed to follow a particular distribution, and if noise properties are unchanging in time, or the assumption of stationarity. Assuming the noise follows a multivariate normal distribution, the assumption of Gaussianity, the joint probability density is:

$$p(\mathbf{n}) = \frac{1}{\sqrt{\det(2\pi\mathbf{C})}} \exp \left[-\frac{1}{2} \sum_{i,j} (n_i - \mu)(n_j - \mu) C_{ij}^{-1} \right] \quad (3.3)$$

The inverse of the covariance matrix is denoted C_{ij}^{-1} , where i, j index discrete time or frequency bins. The noise is referred to as *stationary* if the covariance depends only on the lag $|i - j|$. In this case, the covariance can be described by the correlation function $C(\tau)$, where $\tau = |t_i - t_j|$ is the time lag.

Transforming to the Fourier domain, where i, j now label frequencies f_i, f_j , stationary noise is characterized by a diagonal covariance matrix:

$$C_{ij} = \delta_{ij} S_n(f_i), \quad (3.4)$$

which defines the *power spectral density* $S_n(f)$. The power spectral density is the Fourier transform of the correlation function $C(\tau)$. The *amplitude spectral density* is given by the square root of the power spectral density and has units of $\text{Hz}^{-1/2}$.

Noise is referred to as *white* if $C_{ij} = \delta_{ij}\sigma^2$ in both the time and frequency domains. However, white noise is a poor approximation to the noise observed in LIGO-Virgo detectors.

The process of whitening a strain time series $d(t)$ involves:

$$\begin{aligned} d(t) &\xrightarrow{\text{FFT}} \tilde{d}(f) \\ \tilde{d}(f) &\xrightarrow{\text{Whiten}} \tilde{d}_w(f) = \frac{\tilde{d}(f)}{\sqrt{S_n(f)}} \\ \tilde{d}_w(f) &\xrightarrow{\text{iFFT}} d_w(t) \end{aligned} \tag{3.5}$$

In the case of noise transients (things that go bump), as opposed to spectral lines or known stationary noise, assumptions of stationarity/diagonal covariance, gaussianity, etc. are broken, and they prove impossible to remove by whitening using the PSD.

3.5.1 Likelihood. To calculate the likelihood that the data has a signal, we need to model both the signal and the noise, and confirm that the residuals after removing the model signal match the noise model. For Gaussian noise, the likelihood can be given by:

$$p(d | h) = \frac{1}{\sqrt{\det(2\pi\mathbf{C})}} \exp\left(-\frac{1}{2}\chi^2(d, h)\right), \tag{3.6}$$

where \mathbf{C} is the noise correlation matrix, and the chi-squared statistic is defined as:

$$\chi^2(d, h) = \mathbf{r} \cdot \mathbf{C}^{-1} \cdot \mathbf{r} = (d_{Ik} - h_{Ik}) C_{(Ik)(Jm)}^{-1} (d_{Jm} - h_{Jm}), \quad (3.7)$$

where repeated indices imply summation over the network of detectors I, J and time samples k, m . If the noise is uncorrelated between detectors, then:

$$C_{(Ik)(Jm)} = \delta_{IJ} S_{km}^I,$$

where S_{km}^I is the noise spectral density matrix for detector I . If noise is stationary, then correlations depend only on the time lag between data samples. Then the noise correlation matrix is diagonal in the Fourier domain, as discussed earlier:

$$S_{km}^I = \delta_{km} S^I(f_k).$$

In that case, the chi-squared reduces to a noise-weighted inner product:

$$\chi^2(d, h) = (\mathbf{r} | \mathbf{r}), \quad (3.8)$$

where the noise-weighted inner product is defined as:

$$(a | b) = 2 \int_0^\infty \frac{\tilde{a}(f) \tilde{b}^*(f) + \tilde{a}^*(f) \tilde{b}(f)}{S_n(f)} df. \quad (3.9)$$

The likelihood is critical in Bayesian inference Veitch et al. (2015). By combination with priors for the signal and noise models, we can calculate the model evidence Cornish and Littenberg (2007); Littenberg and Cornish (2010), quantifying the odds that a signal is present, as well as the posterior distributions for model

parameters $\boldsymbol{\theta}$, including the astrophysical parameters for a compact binary inspiral Abbott, others (LIGO Scientific Collaboration, and Collaboration) (2016b, 2019).

For stationary, Gaussian noise that is uncorrelated between detectors, the likelihood function can be stated as:

$$p(d | \boldsymbol{\theta}) = \exp \left[-\frac{1}{2} \sum_I \left((d^I - h^I(\boldsymbol{\theta}) | d^I - h^I(\boldsymbol{\theta})) + \int \ln S_n^I(f) df \right) \right], \quad (3.10)$$

where the sum is taken over detectors I in the network, and $(a | b)$ is the noise-weighted inner product defined in Eq. (3.9).

3.5.2 Matched Filtering Formalism. The total strain measured by a gravitational-wave detector is modeled as:

$$h(t) = s(t) + n(t) \quad (3.11)$$

where:

- $s(t)$: the gravitational-wave signal,
- $n(t)$: the detector noise.

The matched-filter signal-to-noise ratio (SNR) is given by:

$$\rho = \frac{(s|h)}{\sqrt{(s|s)}} \quad (3.12)$$

where $(a|b)$ denotes the noise-weighted inner product between two functions $a(t)$ and $b(t)$.

The noise weighted inner product between two functions $a(t)$ and $b(t)$ is defined in the frequency domain as:

$$(a|b) = 4 \operatorname{Re} \int_0^\infty \frac{\tilde{a}(f)\tilde{b}^*(f)}{S_n(f)} df \quad (3.13)$$

where:

- $\tilde{a}(f), \tilde{b}(f)$: Fourier transforms of $a(t)$ and $b(t)$,

- $S_n(f)$: the one-sided noise power spectral density,

The optimal matched-filter SNR, achievable for signal $s(t)$, is given by:

$$\rho_{\text{opt}} = \sqrt{(s|s)} \quad (3.14)$$

This expression represents the best-case detection statistic for a known waveform in stationary, Gaussian noise.

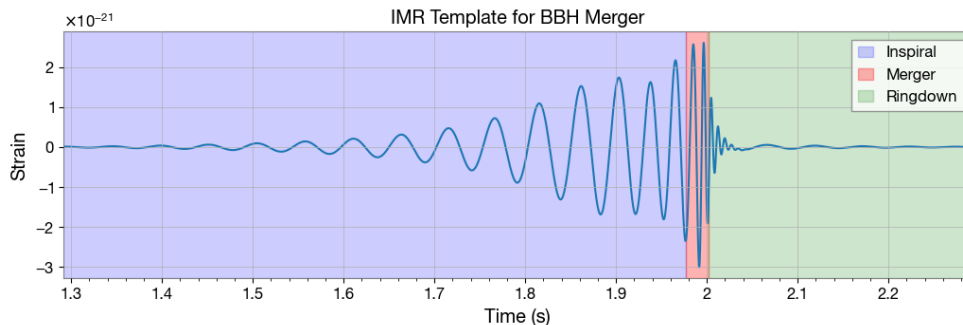


Figure 7. A plot of a time domain Inspiral, Merger, Ringdown (IMR) waveform for an $80M_{\odot}$ and $50M_{\odot}$ BBH coalescence (circular, non-precessing, aligned spins), generated using the IMRPhenomD (Khan et al., 2016) waveform, plotted using the open source gwpy (Macleod et al., 2021) and pycbc packages.

3.5.3 Signal Model. CBC Waveforms can be numerical, analytical, or, in many cases for efficiency and accuracy that may vary in different regimes, combinations of both are stitched together (Ajith, Boyle, Brown, et al., 2012; Hinder, Ossokine, Pfeiffer, & Buonanno, 2018).

For example, IMRPhenomD, a typical BBH waveform for aligned spins (Khan et al., 2016), uses analytical post-newtonian expansion terms during the inspiral, when linearized gravity still explains much of the orbital evolution. This ends around the innermost stable circular orbit (ISCO), or $3R_s$ for a nonspinning black hole. In the strong-field, highly nonlinear part of the merger, full numerical relativity is necessary. Then the ringdown is simulated via perturbation theory, as quasinormal mode oscillations settle into a stable Kerr solution.

Because of the computational demands of computing these waveforms, typically template banks are constructed to span a parameter space of interest, and then faster interpolants are used to find the best waveform for a certain signal.

3.5.4 Parameter Estimation. To infer waveform or astrophysical parameters from a signal embedded in noise, we need a model M for the gravitational-wave signal. We also account for prior information I .

Given a model M that depends on a set of parameters $\boldsymbol{\theta}$, background information I , and a set of observations (data) d , inference is done via application of Bayes' theorem:

$$p(\boldsymbol{\theta} \mid d, M, I) = \frac{p(\boldsymbol{\theta} \mid M, I) p(d \mid \boldsymbol{\theta}, M, I)}{p(d \mid M, I)} \quad (3.15)$$

The left-hand side is the *posterior probability density function*, or simply the *posterior* for $\boldsymbol{\theta}$. The three terms on the right-hand side are:

- The *prior probability density function* $p(\boldsymbol{\theta} \mid M, I)$
- The *likelihood function* $p(d \mid \boldsymbol{\theta}, M, I)$
- The *evidence*:

$$p(d \mid M, I) = \int d\boldsymbol{\theta} p(\boldsymbol{\theta} \mid M, I) p(d \mid \boldsymbol{\theta}, M, I) \quad (3.16)$$

Within the Bayesian parameter estimation framework, inference is reduced to the calculation of the posterior $p(\boldsymbol{\theta} \mid d, M, I)$, given the model M and the analysis assumptions I , which uniquely determine the prior distribution and the likelihood function.

CHAPTER IV

STELLAR ASTROPHYSICS

First, we will explore some of the observable parameters of stars, and how these are measured and inferred. Then, we will explore the physical processes responsible for stellar evolution, through the frame of timescales. Then, we will explore the structure, evolutionary phases, and final outcomes for massive stars. Finally, we will explore the complexities introduced by binarity, and the interactions between evolving stars. How various approaches to modelling evaluate, combine, or ignore these details will be apparent in a brief overview of stellar evolution codes. The general goal of this chapter is to establish in sufficient detail the necessary background in the field of stellar evolution and especially binary evolution to motivate the construction and use of rapid population synthesis codes (Belczynski et al., 2008; Breivik, Chatterjee, Larson, & Kalogera, 2020; Eldridge & Stanway, 2009; Fragos et al., 2023; Hurley, Tout, & Pols, 2002; Portegies Zwart & Verbunt, 1996; Riley, Agrawal, et al., 2022; Willems, Kolb, Justham, & Tout, 2010). We will understand how they are used and why, in which regimes they fall short, and how they can be improved in the future.

4.1 Intrinsic Stellar Parameters

To understand how astrophysical theory is constrained by observation, and can then inform realistic models, we must disentangle which parameters of stars are directly observable (and how they are observed), and which parameters are inferred. Additionally we must understand how observations and models are biased and limited.

4.1.1 Surface Temperature. The effective temperature of a star (T_{eff}) is defined as the temperature of a blackbody with the same luminosity per surface area as the star. Via the Stefan-Boltzmann law:

$$L = 4\pi R^2 \sigma T_{eff}^4 \quad (4.1)$$

It is less straightforward to define the radius at which this temperature is observed. The photosphere of a star is the transparent layer of plasma extending downward to a boundary at which optical depth is 2/3 (Carroll & Ostlie, 2007), or equivalently 50% of light emitted is not re-scattered but escapes the star. For the purposes of effective temperature, the typical definition of the radius is the Rosseland optical depth (1).

4.1.2 Luminosity. The luminosity is the total electromagnetic power emitted. When not qualified otherwise, luminosity is typically bolometric, meaning over all wavelengths. As an intrinsic parameter, its measurement is dependent on both distance and absorption. If a distance is determined by a luminosity measure, it may be called a luminosity distance.

In many cases, an object's energy output may not peak in the band of measurement. For an extreme example, consider a Wolf-Rayet star, a massive and evolved star with a stripped hydrogen envelope with an effective blackbody temperature that could be well over 100,000K. If observed in the infrared, less than 2% of the energy emitted will be in band (Nieva, 2013). While bolometers exist for various applications, they are not sufficiently sensitive to measure starlight. In practice, light is gathered in multiple bands, and then a spectral model is matched to observations to infer the true peak wavelength.

Electromagnetic luminosity is not the only energy sink for stars: neutrinos carry a non-negligible amount of energy from many processes, and a majority of energy from some processes (Supernovae) (Carroll & Ostlie, 2007).

4.1.3 Mass. Masses are notoriously difficult to infer. The available methods are many, and they each offer a unique set of limitations. The first category includes those that directly measure dynamical effects of gravity, being the most model-independent and accurate. (Torres, Andersen, & Gimenez, 2010) In binary systems, Keplerian orbital dynamics can give high precision measurement of mass. Binaries are either visual (apparent separation and tangential velocity), spectroscopic (spectral shift gives radial velocity), or eclipsing (photometry), and can determine mass to a precision of 1-10%. Gravitational Microlensing can give high precision measurements of mass, especially in the case of dark or compact objects, but requires the relatively rare alignment of the lensing foreground object, and is dependent on the measurement of lens mass (Sahu, Anderson, Casertano, & et al., 2022). Empirical models employ Mass-luminosity relations (Eker, Soydugan, Soydugan, & et al., 2015), Isochrone fitting (da Silva, Girardi, Pasquini, & et al., 2006), spectral energy distribution (SED) fitting, and astroseismology (Chaplin & Miglio, 2013). These methods are all highly model-dependent and their precisions are often in the range of 5-30%.

4.1.4 Radius. Similarly, there are direct methods of measuring stellar radius, but in practice many estimates of radius must be inferred and are model dependent. It is in some cases possible to resolve the disk of a star using interferometry, where the angular size is related to a radius via a parallax distance. Boyajian, von Braun, van Belle, et al. (2012) Several hundred nearby stars Chelli et al. (2016) have had their angular diameter measured directly. This

method is difficult to extend beyond 500pc, and works best for stars of large radius (giants). These datasets are used to constrain other inference based methods of estimating radius. For eclipsing binaries, it is possible to measure the radii of stars by modelling the light curve (Torres et al., 2010). Among the indirect methods are SED fitting, which uses broadband photometry to estimate flux, and with a parallax distance and a measured T_{eff} radius is inferred (Stassun, Collins, & Gaudi, 2017) Just as with mass, it is possible to estimate radius from astroseismology. Given a certain oscillation frequency, mean stellar density can be estimated. Given an inferred luminosity and T_{eff} we can always infer a luminosity-radius for an ideal spectrum using the Stefan-Boltzmann law (4.1).

4.1.5 Rotation. There are many methods for measuring stellar rotation, with possibly the best known being spectroscopic line broadening. This technique actually measures the projected rotational velocity $v \sin i$, where i is the inclination angle of the stellar rotational axis. For this to work, there need to be well-defined absorption lines, and we need some constraint on the inclination angle (Gray, 2005). Broadening can show the extent of greatest rotation, which for most stars occurs at the equator. However differential rotation is the norm, given circulation of the stellar atmosphere.

Rotation can also be measured via photometric variability. Given surface features, especially starspots, which are present across multiple rotation periods, time-series photometry can be used to infer a rotational period (Noyes, Weiss, & Vaughan, 1984).

Astroseismology can also be used to constrain rotation: oscillation modes in stars can be split by rotation, due to the Coriolis effect. This can also give insight into the internal rotation profile and structure of stars (frequently core vs. envelope

rotation can differ), in addition to surface rotation (García, Hekker, Stello, et al., 2011).

Zeeman-Doppler imaging and spectropolarimetry are techniques which track rotationally modulated magnetic features, causing variation in circular polarization across spectral lines, giving yet another method for inferring rotation. This technique requires bright, magnetic, and rapidly rotating stars, and is also sensitive to inclination (Donati & Brown, 1997).

It is also possible to simply look for oblateness using interferometry. For stars with a resolvable disk, which also rotate rapidly, direct measurement of rotational flattening has been measured (van Belle, Ciardi, Thompson, Akeson, & Lada, 2001).

Gyrochronology fits empirical rotation-age relations, where magnetic braking leads to slower rotation over time, or some other known process leads to spin-up or spin-down with a known scaling law (Barnes, 2007). This works best for low mass stars that are not fully convective, and younger stars.

In summary, rotation can often be inferred for bright stars with distinct features, but for faint stars or compact objects the picture changes significantly. White dwarfs (WDs) can sometimes have their rotation measured via spectral broadening, and some types of WD experience regular pulsation and are susceptible to astroseismology.

For isolated neutron stars (NSs) which are not pulsars there are analogous though fraught methods for inferring rotation. X-ray surface hot spot modulation from thermal emission can be observed, and are the neutron-star analog of magnetically driven "starspots". Famously, the "Magnificent Seven", are a set of well observed, thermally emitting, radio-quiet neutron stars (Haberl, 2007).

It is also possible to detect cyclotron resonant scattering features, where magnetars exhibit X-ray absorption features that modulate and may reflect spin (Mereghetti, 2008).

In principle, there is a neutron-star analog of astroseismology. It is theorized that neutron stars undergo crustal fracture, or "starquake". This may be observed as glitches in precisely timed pulsars, as "mountains" (millimeter scale deviations in the spheroidal shape of neutron stars!) move or collapse. For stars that accrete, this process may occur regularly. Detection has not been achieved for isolated and non-pulsing NS, though starquakes would introduce or resolve quadrupolar deformation, and are a theorized source of gravitational waves (Andersson, 2011). Recent estimates place these events in the possible sensitivity range of current and future gravitational wave detectors (Chatterjee, Mandal, & Mukhopadhyay, 2024; Giliberti & Cambiotti, 2021).

4.1.6 Metallicity. In the history of the universe, since big-bang nucleosynthesis, all of the elements heavier than hydrogen, helium, and a very small amount of lithium owe their existence to the various processes of stellar evolution. In the typical parlance of astronomy, "metals" are simply elements heavier than helium. As successive generations of stars live and die, they enrich the interstellar medium with heavy elements. This gives us the apt terms "stellar archaeology" (Frebel, 2010), "galactic archaeology" (Freeman & Bland-Hawthorn, 2002), etc. as we forensically re-trace the steps that gave the local universe the chemical composition we observe (and that we're made of). We have the rather unintuitive "stellar population classification", where Population I stars are metal rich (the sun is a typical example, though super-solar metallicities are found in many environments), Population II stars are metal poor, and Population III stars

are primordial metal-free stars, and have not been directly observed, thus models for their evolution and end-states are not well-constrained. Metallicity can be quantified in a few different ways.

By definition, the sum of the mass fractions of hydrogen (X), helium (Y), and metals (Z) must satisfy:

$$X + Y + Z = 1 \quad (4.2)$$

An example for the present-day solar composition (based on modern estimates) is:

$$X_{\odot} \approx 0.715, \quad Y_{\odot} \approx 0.270, \quad Z_{\odot} \approx 0.015 \quad (4.3)$$

For stellar nucleosynthesis, iron abundance is a critical benchmark.

The logarithmic metallicity $[\text{Fe}/\text{H}]$ is related approximately to the metal-to-hydrogen mass fraction ratio Z/X by:

$$[\text{Fe}/\text{H}] \approx \log_{10} \left(\frac{Z}{X} \right)_{\star} - \log_{10} \left(\frac{Z}{X} \right)_{\odot} \quad (4.4)$$

Assuming that iron scales with total metallicity (a good approximation for Population I and II stars), one can derive:

$$\frac{Z}{X} = \left(\frac{Z}{X} \right)_{\odot} \cdot 10^{[\text{Fe}/\text{H}]} \quad (4.5)$$

This allows the recovery of the total metal mass fraction Z if the hydrogen fraction X is known, or vice versa.

Observationally, high resolution spectroscopy allows for abundance analysis. This requires models of the stellar atmosphere, and is confounded by factors such as turbulence (Gray, 2005; Sneden, 1973).

4.2 Physical Processes and their Timescales

In stellar evolution, many calculations are made possible by the drastic separation of timescales. When considering only one process, the others can be held static in a model. In many problems, this is a reasonable assumption. In some of the more interesting transitional phases in a star's lifetime, one process will come to dominate over another, or these assumptions will even break down, and this is where some of the as-yet unresolved issues in stellar evolution models lie. First, we will examine some of the basic timescales at play in typical stars.

4.2.1 Dynamical Timescale. Stars exist in a balance known as hydrostatic equilibrium (gravitational collapse and fluid pressure are in balance, giving an axisymmetric and static ellipsoidal shape). Disruptions to stellar structure due to changing conditions proceed to re-equilibrate on dynamical timescales, otherwise known as free-fall timescales. It is roughly equal to the time for a sound-wave to cross a star.

The timescale is given by the collapse time in the absence of any pressure forces Hansen, Kawaler, and Trimble (2004); Riley, Agrawal, et al. (2022).

$$\tau_{\text{dyn}} = \sqrt{\frac{R^3}{GM}} \approx 1600 \text{ s} \left(\frac{R}{R_{\odot}} \right)^{3/2} \left(\frac{M}{M_{\odot}} \right)^{-1/2} \quad (4.6)$$

This would take about 30 minutes for the sun, and a matter of milliseconds for a neutron star, with its total collapse nearly complete. For a massive but diffuse supergiant with a radius 1000 times that of the sun, the collapse time is over 20 days, and the dynamical processes at play are thus very different.

4.2.2 Thermal Timescale. The thermal, or Kelvin-Helmholtz timescale is the time it would take for an object to radiate away all of its

gravitational binding energy, given constant luminosity and the absence of nuclear burning.

$$\tau_{\text{KH}} \sim \frac{GM^2}{RL} \tau_{\text{KH}} \approx 3.0 \times 10^7 \text{ yr} \left(\frac{M}{M_{\odot}} \right) \left(\frac{M_{s/\text{env}}}{M_{\odot}} \right) \left(\frac{R}{R_{\odot}} \right)^{-1} \left(\frac{L}{L_{\odot}} \right)^{-1} \quad (4.7)$$

where $M_{s/\text{env}}$ is either the total mass of the star M for stellar types without a clearly defined envelope, or the mass of the envelope M_{env} for stars with a clearly defined envelope, as per Hurley et al. (2002). In the 19th century, before the discovery of nuclear fusion, it was thought that the age of the sun was a few million years (Kutner, 2003), now sometimes referred to as the "gravitational lifetime" of a star. Similarly, protostars which have yet to achieve fusion ignition evolve on the thermal timescale.

4.2.3 Nuclear Timescale. The nuclear timescale describes the main-sequence lifetime of a star, fusing hydrogen into helium, assuming all the star's hydrogen is fusible. The dominant fusion process turns four protons into one helium nucleon, where the energy liberated is the difference in binding energies:

$$\frac{\Delta E}{E} = \frac{4m_p c^2 - m_{\text{He}} c^2}{4m_p c^2} \approx 0.007 \quad (4.8)$$

roughly speaking, for the sun:

$$\tau_{\text{nuc}} = \frac{\Delta E}{L} \approx \frac{0.007 M_{\odot} c^2}{L_{\odot}} \approx 10^{11} \text{ yr} \quad (4.9)$$

In reality, the sun's lifetime on the main sequence is a factor of 10 shorter, because sun-like stars evolve off of the main sequence after they have consumed only 10% of their hydrogen. Thus the predicted lifetime of the sun is about 10^{10} yr . After the main-sequence, successive evolutionary phases result in faster, hotter burning for even less abundant fuels, and are typically an order of magnitude

shorter. Mass is the main determining factor in how fast and how far these successive stages can go. The Zero-Age Main-Sequence mass (ZAMS) is the mass at the start of Hydrogen burning. In evolved, massive stars, fusion of heavier elements occurs in thin shells within the core which are radiation dominated and have a limited ability to mix. Only in the least massive stars, convective mixing allows the core access to all of the new fuel. This process gives M-dwarves with $M_{ZAMS} < 0.35M_{\odot}$, a fully convecting interior, and a relatively small rate of fuel consumption; an estimated lifespan of over $10^{12}yr$ (Choi et al., 2016). In similar models, stars with $M_{ZAMS} < 0.8M_{\odot}$ will not have evolved off the main sequence in a Hubble time (13.8Gyr). Thus, we have never observed the end-state evolution of these low-mass stars (Laughlin & Bodenheimer, 1997), and stellar observation can also offer an oblique and roundabout approach to measuring the age of the universe.

For massive stars, luminosity scales as at least M^3 , but often M^4 , with greater temperatures and pressures in the core. Additionally, more massive stars have less efficient mixing than low-mass stars and can access less than 10% of their fuel. For example, in one model, a star beginning with $65M_{\odot}$ at ZAMS will be on the main sequence for less than 5 million years, with a peak luminosity of $10^6 L_{\odot}$. Successive evolution, with an analogous Helium-main-sequence fusing heavier elements in thin shells in the core, proceeds at a rate typically an order of magnitude faster, and the star will run out of fuel and undergo supernova (SNe).

4.2.4 Diffusion Timescale. Typically referring to photon diffusion, this is the characteristic timescale for energy radiated from fusion in the core to escape the photosphere of a star. Despite moving at c , photons scatter frequently in the opaque plasma of stellar interiors. This timescale is approximately:

$$\tau_{\text{diff}} \sim \frac{R^2}{c\lambda} \quad (4.10)$$

where λ is the photon's mean free path. For the sun this is $10^4 - 10^5$ yr. Being a stochastic process, if fusion were to cease suddenly, a star would well into a gradual dimming around this time.

4.2.5 Pulsation. There are many unstable regions of the stellar parameter space where periodic changes in luminosity, temperature, and radius are predicted and observed. This proves useful where behavior is predictable, and luminosity can be inferred from spectra and pulsation period, serving as "standard candles" in the cosmic distance ladder. Some well studied instability regions include the classical Cepheids (Bono, Marconi, & Stellingwerf, 2000), the δ Scuti and γ Doradus domains (Dupret, Grigahcène, Garrido, Gabriel, & Scuflaire, 2005), RR Lyrae variables, and the β Cephei and Slowly pulsating B-type regions (Aerts, Christensen-Dalsgaard, & Kurtz, 2010; Pamyatnykh, 1999). The pulsation timescales for radial modes is typically close to the dynamical timescale. An excellent discussion of the physics of stellar pulsation can be found in (Pols, 2011).

4.2.6 Mass-Loss Timescale. For mass loss via stellar wind, we can calculate how long it would take for the star to lose all available mass at its current mass-loss rate. In our nearby solar laboratory, this value (10^{13} yr) is much longer than the estimated lifetime of the Sun, thus much longer than the nuclear timescale. As luminosity scales drastically with mass, so does photon pressure, and in massive stars the mass-loss timescale becomes much shorter than the nuclear timescale, meaning that the entire envelope of the star can be expelled before the end of main-sequence burning. These types of stars, supergiants, luminous blue

variables (LBVs), Wolf-Rayet (WR) stars, are short lived, with fundamentally different processes governing their evolution than sun-like stars. Uncertainties in the mass loss processes introduce the greatest uncertainties in our predictions of the fates of massive stars, including supernova type, and compact object properties.

Table 2. Summary of Stellar Timescales

Timescale	Sun	10 M_{\odot} MS	50 M_{\odot} MS	100 M_{\odot} MS	10 M_{\odot} WR	Neutron Star	White Dwarf
Dynamical	30 min	10 min	5 min	3 min	few min	μs –ms	~ 1 sec
Thermal (KH)	10^7 yr	10^5 yr	10^4 yr	10^3 yr	10^4 yr	1 – 10^6 yr	10^7 – 10^9 yr
Nuclear	10^{10} yr	2×10^7 yr	4×10^6 yr	2×10^6 yr	10^6 yr	—	—
Diffusion	10^5 yr	10^3 yr	10^3 yr	10^3 yr	few 10^3 yr	—	$\sim 10^5$ yr
Pulsation	5 min	Hours–Days	Hours	Hours	Minutes–Hours	ms–s	—
Mass-loss	\gg lifetime	\sim lifetime	$<$ lifetime	\ll lifetime	10^5 – 10^6 yr	accretion-dependent	negligible

4.2.7 Internal Structure. Given the description of processes at work and their timescales, we can now sketch out some standard structural models of stars, especially for the sake of finding where assumptions change or break down.

The Schwarzschild criterion for convection (Schwarzschild, 1906) in stellar atmospheres provides a theoretical transition point between the two dominant energy transfer mechanisms in stars: convective and radiative transport. Initial (ZAMS) mass is the primary determining factor for how stars evolve (with metallicity as a secondary factor) and the major regimes in mass provide fundamentally different structure due to these transition points.

If we consider stellar layers in hydrostatic equilibrium, and displace mass adiabatically (no heat exchanged), convection is the condition under which those elements continue to move. If the adiabatic temperature gradient is less than the actual temperature gradient, then radiative transport becomes so inefficient that convection sets in as the primary carrier of energy. This can be due to high opacity due to partial ionization. Convection flattens the temperature gradient, reduces central temperature, and mixes fusion fuel evenly through a layer. With

radiative transport, fuel is unable to mix evenly and the lifetimes of a phase can be dramatically reduced. Rigorous derivations of these criteria are in Hansen et al. (2004); Kippenhahn et al. (2012). The mass ranges for which radiative or convective transport dominate in the core or envelope follow:

Mass Range	Core T (K)	Core	Envelope	Main Sequence Type	Evolved Type
$M \lesssim 0.3 M_{\odot}$	$4-7 \times 10^6$	Convective	Convective	M-dwarfs (late M)	He white dwarf (not yet observed, unless stripped)
$0.3-1.3 M_{\odot}$	$7-15 \times 10^6$	Radiative	Convective	K to early F-type	RGB, AGB, CO white dwarf
$1.3-2.0 M_{\odot}$	$15-30 \times 10^6$	Convective	Radiative	A-type to early F-type	Helium core burning, AGB, CO white dwarf
$2.0-8.0 M_{\odot}$	$30-60 \times 10^6$	Convective	Radiative	Late B to A-type	Super-AGB or ONeMg white dwarf / ECSN
$M \gtrsim 10 M_{\odot}$	$60-100 \times 10^6$	Convective	Radiative	O-type	Red supergiant (RSG), LBV, WR, SN II/Ib/Ic

Table 3. Internal structure, fusion regime, and evolutionary outcomes for stars of various masses (Chabrier & Baraffe, 1997; Woosley et al., 2002)

4.2.8 Evolutionary Stages and Tracks of Massive Stars. There are many stages of stellar evolution and many terms for types of stars at each stage. Some of the main ones used are defined below:

They can be generally grouped by type. As the end of the main sequence, Hertzsprung Gap and Helium flash stars exhibit a larger radius and different behavior, and we refer to these later stages as "evolved types". This may be used interchangeably with many of the above terms, and mainly means that Helium and heavier elements are being burned in the core.

4.3 Supernovae

Stellar end states are determined by the mass, and by extension the pressure and temperature, reached in the core, and the regimes of fusion that are sustained there. Iron represents the end of normal stellar nucleosynthesis having the highest binding-energy-per-nucleon. Forming elements heavier than iron requires significant energy input and occurs only in catastrophic (explosive) circumstances. When fuel runs out, hydrostatic equilibrium is lost, stars experience collapse, and either re-equilibration or explosion. "Burning" heavier elements requires dramatically higher temperatures and pressures in the core to overcome the Coulomb force of

Stellar Phase	Abbreviation
Main sequence (H-burning)	MS
Hertzsprung gap (evolved types)	HG
Core helium burning	CHeB
Asymptotic giant branch	AGB
Red/Yellow/Blue super giant	RSG, YSG, BSG
Chemically homogeneously evolving	CHE
Luminous Blue Variable	LBV
Wolf Rayet(stripped types)	WR
Helium main sequence, HG, GB	HeMS, HeHG, HeGB
Helium white dwarf (remnants)	HeWD
Carbon-oxygen white dwarf	COWD
Oxygen-Neon white dwarf	ONeWD
Neutron star	NS
Black hole	BH

Table 4. Stellar phases and abbreviations used, adapted from Riley, Stevenson, et al. (2022).

heavier nuclei. The structure of the core becomes increasingly compact with later evolution, and the timescales of burning become dramatically shorter, with silicon burning lasting only days!

Table 5. Properties of nuclear burning stages in a $15 M_{\odot}$ star (Woosley et al., 2002).

Burning Stage	T [10^9 K]	ρ [g/cm^3]	Fuel	Main Products	Timescale
Hydrogen	0.035	5.8	H	He	1.1×10^7 yr
Helium	0.18	1.4×10^3	He	C, O	2.0×10^6 yr
Carbon	0.83	2.4×10^5	C	O, Ne	2.0×10^3 yr
Neon	1.6	7.2×10^6	Ne	O, Mg	0.7 yr
Oxygen	1.9	6.7×10^6	O, Mg	Si, S	2.6 yr
Silicon	3.3	4.3×10^7	Si, S	Fe, Ni	18 d

For lower-mass stars, late evolution burns helium, and possibly carbon, nitrogen, oxygen. follows the asymptotic giant branch (AGB), which episodically expels the envelope, creates a planetary nebula, and leaves a white dwarf (He, C-O, or O-Ne depending on mass) for stars with $M_{ZAMS} < 7.8M_{\odot}$. For stars near the threshold for core collapse, electron-capture supernovae (ECSNe) may occur (Hiramatsu et al., 2021). For stars above $M_{ZAMS} < 8.1M_{\odot}$, an iron core is built, supported by electron degeneracy pressure. Core collapse (CCSNe) supernova follows when this core mass surpasses its Chandrasekhar limit (Chandrasekhar, 1931).

At a core temperature of 3×10^9 K, there is sufficient energy (511 keV) for photons to produce e^+, e^- pairs, acting as a sink for energy, and leading to collapse, followed by rapid fusion which disrupts the star leaving no remnant. This was predicted in 1964 (Fowler & Hoyle, 1964) and first simulated in 1967 (Barkat, Rakavy, & Sack, 1967; Fraley, 1968). There still seems to be no way around this mechanism (Woosley, 2017), and it sets an upper limit on the core temperature

Table 6. Summary of stellar end states by ZAMS mass and core conditions, adapted from COMPAS (Riley, Agrawal, et al., 2022), with core temperatures and burning stages informed by stellar evolution models (e.g., Woosley et al. 2002).

Final State	ZAMS Mass [M_{\odot}]	He Core [M_{\odot}]	Core Temp [K]	Heaviest Fusion	Notes
Helium White Dwarf (He WD)	< 0.5	—	$\lesssim 10^7$	H	Forms in binaries via envelope stripping; He burning not ignited.
Carbon-Oxygen White Dwarf (CO WD)	0.5–8	$1.6M_{\odot}$	$\sim 10^8$	He	Helium burning complete; carbon ignition not reached.
Oxygen-Neon White Dwarf (ONe WD)	8–10.5	$\gtrsim 1.6M_{\odot}$	$\sim 5 \times 10^8$	C	Carbon ignition occurs; neon burning not reached.
Electron-Capture Supernova (ECSN)	~ 7.5 –8.1	1.6–2.25	$\sim 10^9$	Ne/Mg	Collapse via electron captures in ONe cores; forms low-mass NS.
Core-Collapse Supernova (CCSN)	>8.1	>2.25	$\gtrsim 10^{9.5}$	Si/Fe	Collapse of iron core; remnant is NS or BH depending on fallback.
Ultra-Stripped Supernova (USSN)	Binary-dependent	Any (if env. < 0.1)	$\gtrsim 10^9$	Si/Fe	Occurs after case BB mass transfer in binaries; reduced envelope and natal kick.
Direct Collapse	$\gtrsim 40$ –50 (metallicity dependent)	$\gtrsim 10$	$\gtrsim 10^{9.5}$	Si/Fe	No SN; most or all of supergiant progenitor collapses to BH. May be common at low Z.
Pulsational Pair-Instability SN (PPISN)	Variable (He core 35–60)	35–60	$\sim 2 \times 10^9$	O/Si	Pulses triggered by pair production; ends in BH formation.
Pair-Instability Supernova (PISN)	$\gtrsim 120$ (He core >60)	60–135	$\gtrsim 3 \times 10^9$	O/Si	Star fully disrupted by explosive oxygen burning; no remnant.
Direct Collapse	$\gtrsim 250$ –300	$\gtrsim 135$ –150	$\gtrsim 10^9$	Si/Fe	Direct collapse again becomes possible above the gap.

of stable stars. Direct collapse without supernova may be possible both above and below the pair instability gap, allowing efficient conversion of all or most of the envelope into BH mass Fryer (1999), motivating searches for disappearing progenitors and ”failed supernovae” (Gerke, Kochanek, & Stanek, 2014), and turning up strong evidence for RSG as progenitors for direct collapse black holes (Adams, Kochanek, Gerke, Stanek, & Dai, 2017a).

4.4 Binarity

A majority of sun-like stars exist with close companions, or as higher-order multiples. For massive stars, binarity increases, with 70-100% of O and B type stars existing in binaries (Duchêne & Kraus, 2013; Moe & Di Stefano, 2017; Sana et al., 2012), scaling approximately as:

$$f_{\text{bin}} \propto M^{0.5}$$

While higher order or N-body interactions can form or disrupt binaries, especially in high density environments such as globular clusters or galactic centers, we will consider primarily the field-formation scenario, meaning that the gravitational

collapse of gas formed not just one but two or more protostars at approximately the same time, from the same interstellar material. For tracking the evolution and interaction of binaries, we will adopt the same parameters as Riley, Agrawal, et al. (2022) as used in the COMPAS code, and outline mass transfer and other interactions in a very similar way. The orbital angular momentum of a binary system with non-rotating stars is given by:

$$J_{\text{orb}} = \mu \sqrt{GM_{\text{tot}}a(1 - e^2)} \quad (4.11)$$

where

$$M_{\text{tot}} = M_1 + M_2, \quad \mu = \frac{M_1 M_2}{M_{\text{tot}}} \quad (4.12)$$

and a is the semi-major axis, e is the orbital eccentricity, and G is the gravitational constant.

4.4.1 Mass-loss in Binaries. Mass-loss carries away the specific angular momentum of the mass-shedding star. We assume this occurs gradually with $M/M_{\odot} \gg P_{\text{orb}}$ where P_{orb} is the orbital period of the system. If fast (radiation pressure having pushed them to escape velocity) winds are emitted spherically symmetrically from the surface of the star, this is known as the Jeans mode (Huang, 1956).

The orbital separation evolves due to isotropic wind mass loss as:

$$\frac{\dot{a}}{a} = -\frac{\dot{M}_{\text{tot}}}{M_{\text{tot}}} \quad (4.13)$$

which implies:

$$aM_{\text{tot}} = \text{constant}$$

and the orbital eccentricity remains unchanged Dosopoulou and Kalogera (2016).

4.4.2 Tides. Tidal interactions play a significant role in the evolution of close binaries (Zahn, 1975), and can change separation, spin, eccentricity, etc. which all have an influence on final outcomes. They lead to spin-orbit coupling, aligning the star’s spin with the orbital axis. They also tend to circularize orbits, and redistribute angular momentum from components to the orbit, as tidal lock is the lowest energy orbital configuration.

There has been recent effort to self-consistently model tides in population synthesis, though this will not be covered here.

4.4.3 Mass Transfer. A symplified treatment of mass transfer as might appear in various population synthesis codes will help us establish some of the outcomes of interactions. We will distinguish between two components of a binary with a donor (subscript d) and an accretor (subscript a). We can have conservative or nonconservative mass transfer, and in the latter case total angular momentum of the binary changes. If we take the time derivative of the total angular momentum and re-arrange, we obtain:

$$\frac{\dot{a}}{a} = 2 \frac{\dot{J}_{\text{orb}}}{J_{\text{orb}}} - 2 \frac{\dot{M}_{\text{d}}}{M_{\text{d}}} - 2 \frac{\dot{M}_{\text{a}}}{M_{\text{a}}} + \frac{\dot{M}_{\text{d}} + \dot{M}_{\text{a}}}{M_{\text{d}} + M_{\text{a}}} + \frac{2e\dot{e}}{1 - e^2} \quad (4.14)$$

We can parameterize the efficiency of mass donated as:

$$\dot{M}_{\text{a}} = -\beta \dot{M}_{\text{d}} \quad (4.15)$$

with $0 \leq \beta \leq 1$. We assume circularization at the onset of Roche-lobe overflow (RLOF). We can also assume nonaccreted matter leaves the system with γ times the specific orbital angular momentum, i.e. $J_{\text{orb}}/\dot{M} = \gamma J_{\text{orb}}/M$. Thus the last

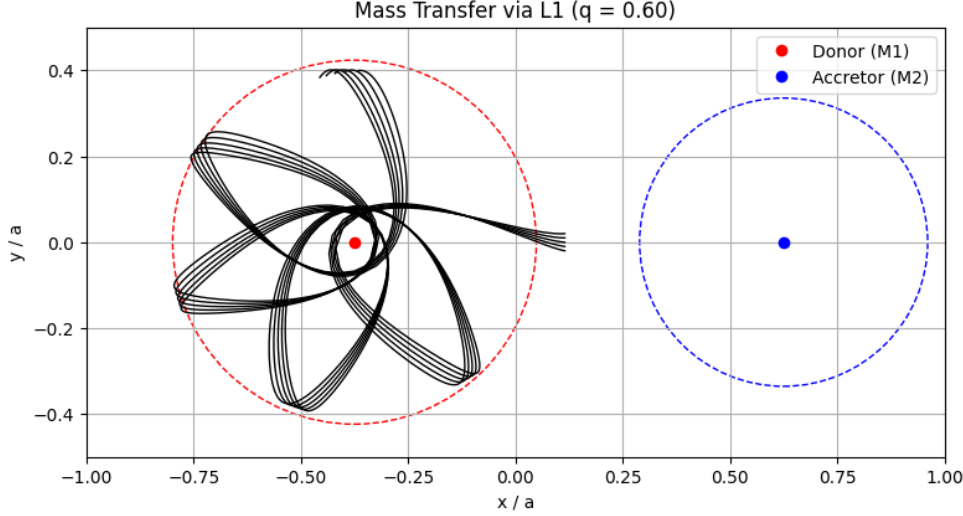


Figure 8. Test particle tracks in the Eggleton approximation to Roche radii.

equation becomes:

$$\frac{\dot{a}}{a} = -2 \frac{\dot{M}_d}{M_d} \left[1 - \beta \frac{M_d}{M_a} - (1 - \beta) \left(\gamma + \frac{1}{2} \right) \frac{M_d}{M_d + M_a} \right] \quad (4.16)$$

This gives the overall orbital evolution during a mass transfer episode.

4.4.4 Roche-lobe Overflow. The first Lagrangian point in the binary is the junction between both Roche lobes, beyond which material is gravitationally unbound, and through which material can follow equipotential lines and freely transfer from one star to another. COMPAS follows Eggleton (1983) in approximating the Roche lobe radii. Rather than the realistic teardrop-shaped lobes, this model treats the stars as point masses, with circular radii, which once overlapped at periapsis ($R > R_{RL}(1 - e)$) can initiate mass transfer.

$$r_{RL} = \frac{R_{RL}}{a} = \frac{0.49q^{2/3}}{0.6q^{2/3} + \ln(1 + q^{1/3})} \quad \text{where} \quad q = \frac{M_d}{M_a} \quad (4.17)$$

4.4.5 Stability Criteria. Once RLOF occurs, we can compare the radius of the donor star responds to mass loss in comparison to the Roche-radius.

Dynamically unstable mass transfer will lead to a common envelope(CE) event (Soberman, Phinney, & van den Heuvel, 1997).

4.4.6 Stable Mass Transfer. During a stable mass transfer episode, the transfer rate occurs approximately on the thermal timescale.

$$\dot{M}_d = \frac{M_d}{\tau_{\text{KH},d}} \quad (4.18)$$

For the accretor, the rate is limited by thermal expansion in the case of stars, and the eddington limit in the case of compact objects.

$$\dot{M}_a = \begin{cases} \dot{M}_{\text{KH},a} & \text{if stellar accretor} \\ \dot{M}_{\text{Edd}} & \text{if compact object accretor} \end{cases} \quad (4.19)$$

$$\dot{M}_{\text{KH},a} = C \cdot \frac{M_a}{\tau_{\text{KH},a}} \quad (4.20)$$

$$\dot{M}_{\text{Edd}} = 1.5 \times 10^{-8} \left(\frac{R_*}{10 \text{ km}} \right) M_\odot \text{ yr}^{-1} \quad (4.21)$$

4.4.7 Common Envelopes. Two cores can occupy a shared envelope in a short-lived phase resulting from dynamically unstable mass transfer (Ivanova et al., 2013). The common envelope phase is commonly invoked to achieve the small orbital separations necessary for compact binaries to merge within a hubble time. The physics of this process are not well understood, and models and initial conditions need to be carefully balanced to achieve a reduction in separation without a merger. Drag inside the shared envelope leads to an inspiral, and orbital energy is used to expel the envelope, leaving two cores at a closer initial separation. Hydrodynamical simulations (Lau et al., 2022) are necessary to elucidate details and outcomes of this process. Because common envelope events proceed on dynamical timescales, they are difficult to observe, lasting days-

months for the initial plunge-in phase, and perhaps being observable for years-decades for the Luminous red novae (MacLeod, Macias, Ramirez-Ruiz, Graczyk, & Schweizer, 2017; Pejcha, Metzger, & Tomida, 2016), a hypothesized observable counterpart/aftereffect to common envelopes. Many candidates are also well explained by mergers, or "failed common envelope" events. There are catalogs of possible post common envelope systems (Kruckow, Neunteufel, Di Stefano, Gao, & Kobayashi, 2021), most of which feature white dwarf remnants. Typically in population synthesis, the common envelope process is parameterized with the $\alpha_{CE} - \lambda$ formalism.

$$E_{\text{bind}} = \alpha_{\text{CE}} \Delta E_{\text{orb}} \quad (4.22)$$

ΔE_{orb} is the difference between the binary orbital energy after the CE phase and α_{CE} is the fraction of the orbital energy that is used to unbind the envelope. λ parameterizes the internal structure and how much of the shared envelope can be unbound.

$$E_{\text{bind}} = -\frac{GMM_{\text{env}}}{\lambda R} \quad (4.23)$$

4.5 Formation Channels of Double Compact Objects

4.5.1 Field Formation. Field formation is the term for isolated binary evolution. In all field formation scenarios the common assumptions are: two stars in a stable orbit form at the same time with the same metallicity, ie. from the same cloud of gas and dust. Higher order interactions, gravitational or otherwise, are not considered.

4.5.1.1 Common Envelope. Following Mandel and Farmer (2022), we can sketch out the steps by which the common envelope process acts as a

formation channel for binary black holes that merge in a Hubble time. This channel comprises an episode of stable mass transfer, followed by a common envelope once the secondary evolves.

1. A binary with initial masses of 100 and 75 M_{\odot} are separated by 10AU and have about 5% of solar metallicity.
2. The more massive primary completes hydrogen burning on the main sequence faster, and the core contracts, leading to a more energetic helium burning shell and a vastly expanded envelope, expanded past it's Roche lobe. The mass transfer occurs on the thermal timescale of the donor. The mass loss is non-conservative and may widen the binary to 20AU.
3. Mass transfer removes the entire envelope of the primary, leaving a Wolf-Rayet star.
4. The stripped primary continues to evolve on the "Helium main sequence", rapidly reaching the point of core collapse and leaving a black hole.
5. The secondary evolves off the hydrogen main sequence, expanding to overflow it's Roche Lobe. Mass transfer is now dynamically unstable, leading to a common envelope, drag, inspiral, and orbital hardening. The energy of the orbit is transferred to the envelope, which is thermally expelled at the right time to avoid merger, with an orbital separation of $35R_{\odot}$ in their example.
6. The secondary evolves, loses mass, and eventually collapses into a black hole. The binary merges in 10Gyr via gravitational radiation.

With so many uncertain steps with physics that is difficult to constrain, the viability of this process is a topic of great debate in the literature. Later we

will walk through the fraction of systems expected to survive each of the hurdles present here (kicks, mergers, etc.) Indeed, the models require fine tuning here for the channel to contribute significantly.

4.5.1.2 *Stable Mass Transfer.* It is also possible to have a similar sequence as enumerated above, but with the common envelope phase replaced by a stable mass transfer phase. van Son et al. (2022) has an analysis of the impact this channel may have on the BBH mass distribution.

It is worth mentioning that many of these channels may lead to mass ratio reversal, meaning that the more massive primary, which donates mass first, becomes a less massive compact object than its companion.

4.5.1.3 *Chemically Homogenous Evolution.* CHE may be a possibility for close, high mass binaries at less than 10% solar metallicity: rapid rotation is thought to lead to enhanced mixing. If the core is able to access hydrogen from the envelope, then much more (as much as 70%) of the initial mass of the star can be converted into final black hole mass, with the possibility of direct collapse (de Mink & Mandel, 2016; Mandel & de Mink, 2016; Marchant, Langer, Podsiadlowski, Tauris, & Moriya, 2016). The components of such a system would avoid expansion and mass transfer, remaining tidally locked in a close orbit. While this channel remains physically plausible, it has become more disfavored as a dominant contributor due to the fine tuning required in separation and metallicity, and its inconsistency with the lack of observed high, aligned spin BHs in observations (Bavera, 2020; Belczynski et al., 2020; Qin et al., 2018). The possibility for CHE was added to COMPAS as described in Riley et al. (2021b).

4.5.1.4 *Population III Stars.* While yet unobserved, expected at $z \gtrsim 15$, the first generation of stars are thought to have evolved in ways

fundamentally different from binaries in the local universe, including limited expansion in later phases of evolution. With zero metallicity, and a top-heavy IMF, initial masses have been suggested over $1000 M_{\odot}$. They would experience weak winds, and direct collapse with masses above the pair-instability gap (Madau & Rees, 2001).

Even more exotic models allow the formation of supermassive stars (SMSs) of 10^4 – $10^6 M_{\odot}$. These then rapidly collapse into massive BH seeds ($10^5 M_{\odot}$). This is a possible solution to the apparent super-*eddington* growth of the supermassive black holes (SMBH) observed in the local universe (Begelman, Volonteri, & Rees, 2006; Latif, Schleicher, Schmidt, & Niemeyer, 2013).

Delay times in mergers mean that we may observe these as a contributor to the BBH population even in the local universe ($z < 1$) (Belczynski et al., 2017; Hartwig et al., 2016; Kinugawa, Inayoshi, Hotokezaka, Nakauchi, & Nakamura, 2014).

4.5.2 Dynamical Formation. In dense stellar environments (Globular clusters, Young massive/open clusters, and galactic nuclei), higher order interactions can harden orbits and allow for close compact binaries (Rodriguez, Haster, Chatterjee, Kalogera, & Rasio, 2016). With black holes being massive, the congregate toward the center as kinetic energy is equipartitioned by scattering interactions (Mandel & Farmer, 2022). In three body interactions, the lighter member is always more likely to be ejected, and so with time more binaries have harder orbits with heavier components.

In isolated triples, Kozai-Lidov effects can harden one binary, and may also enhance merger rates (Antonini, Gieles, Gualandris, Heggie, & Trenti, 2019; Antonini & Rasio, 2016).

The key signatures of this channel are isotropic spins due to the randomness of dynamical pairing, and a wide range of mass ratios. Additionally, hierarchical mergers are possible (sequential merging of multiple generations of BBH), thereby allowing mergers in the pair instability gap with all components being formed via isolated evolution, with GW190521 (Abbott et al., 2020) being the foremost candidate for this pathway (Kimball et al., 2020).

4.5.3 Active Galactic Nuclei Assisted. It may be possible for stellar mass black holes to become embedded in the dense accretion disc of SMBH in Active Galactic Nuclei (AGN). This environment offers opportunities for three-body encounters in the disc, as well as hardening of the orbit via gas interaction (Bartos, Kocsis, Haiman, & Márka, 2017; McKernan, Ford, Lyra, & Perets, 2012). This mechanism, via conversion of orbital energy to thermal energy, has even been proposed as an electromagnetic counterpart for normally dark BBH mergers, and a possible counterpart to GW190521 (Graham, 2020).

4.6 Detailed Stellar Evolution Codes

Detailed stellar evolution self-consistently models the physics of stellar evolution, with the goal being to elucidate new processes as constrained by both observation and theory. Typically a single star or a single binary system is modelled, and the dimensionality, resolution, and physics in play can be chosen based on the use case. A quick list of some of the most popular detailed stellar evolution codes follows:

4.6.1 Rapid Population Synthesis. The purpose of rapid binary population synthesis, or BPS, is to accurately but quickly represent formation scenarios of any rare event of interest, and understand how often they arise in a realistic population. To understand the relative rarity of CBCs, we can explore

Table 7. Comparison of Dimensionality in Stellar Modeling Codes. 1-D: Kippenhahn et al. (2012); Paxton et al. (2011, 2013), Heger2000

. 2-D: Deupree (1990); Viallet, Meakin, Arnett, and Mocák (2013). 3-D: Freytag et al. (2012); Fryxell, Olson, Ricker, and et al. (2000); Meakin and Arnett (2007); Müller, Janka, and Heger (2012); Ricker and Taam (2012)

Feature / Assumption	1-D (MESA, STARS, KEPLER)	2-D (ROTORC, MUSIC)	3-D (FLASH, CASTRO, AREPO)
Spatial symmetry	Spherical symmetry ($\partial/\partial\theta = \partial/\partial\phi = 0$)	Axisymmetry ($\partial/\partial\phi = 0$)	No symmetry assumed
Convective transport	Parametrized (e.g. MLT)	Parametrized or resolved	Resolved via hydrodynamics
Rotation	Shellular (1-D diffusive transport)	Cylindrical or shellular approximation	Fully resolved
Magnetic fields	Effective diffusion or ignored	Axisymmetric MHD possible	Full MHD possible
Turbulence	Not resolved; modeled as diffusion	Partial modeling possible	Directly simulated
Mass accretion	Prescribed rate or boundary condition	Spatially resolved in one axis	Fully spatially resolved
Shock propagation	Only approximate treatment	Better angular resolution	Fully resolved
Binary interaction	Treated externally or via prescriptions	Not usually modeled	Possible with binary-specific 3-D codes
Computational cost	Low (minutes to hours per model)	Moderate	High (weeks to months per simulation)

the reasons for their scarcity, using the popular Drake equation style approach, following the logic of Mandel and Farmer (2022). Firstly, the initial mass function of stars, or IMF (Salpeter, 1955), is still reliably observed as:

$$\xi(M) = \xi_0 M^{-2.35} \quad \text{for } M \gtrsim 0.5 M_\odot \quad (4.24)$$

for higher masses. The Kroupa (2001) IMF improves this fit by flattening the distribution somewhat at lower masses. It is important to clarify that this is the distribution of masses at formation, determined by the characteristic size of collapsing clouds of gas and other star forming processes, not the number that can be observed from any point in space. Meaning that for $10M_\odot$ stars, 200 sun-like stars will form. And for $100M_\odot$ stars, over 50,000 sun-like stars will form. The rarity of massive stars is twofold because of their shorter lifespans. The sun will live for 500 times longer than a typical $10M_\odot$ star, thus observing these stars in evolution, especially in short lived transitional phases that display interesting physics, is difficult. Considering the specific example of binary black hole (BBH) formation through the common envelope (CE) channel:

- $f_{\text{primary}} \sim 0.001$: fraction of stars massive enough to form black holes

Given a typical initial minimum mass for forming black holes of around $20M_{\odot}$, via the IMF we can see that about 0.1% of binaries will have a primary mass this large.

- $f_{\text{secondary}} \sim 0.5$: fraction of binaries with massive secondaries

The mass ratio between primary and secondary appears to be roughly uniform for massive stars (Moe & Di Stefano, 2017; Sana et al., 2012)

- $f_{\text{init sep}} \sim 0.5$: fraction of systems with favorable initial separations

Initial separations are approximately uniform in log, and the first mass transfer episode should happen at the expansion to core helium burning, during an expansion of several orders of magnitude, occupying much of this range.

- $f_{\text{survive SN1}} \sim 1$: survival probability after the first supernova

Most models predict low kicks for black holes, so for BBH formation most systems will survive (not the case for BNS)

- $f_{\text{CE}} \sim 0.1$: fraction that successfully eject the common envelope

The most uncertainty is likely in this step, but for a number of reasons outlined in Mandel and Farmer (2022) the system is unlikely to survive.

- $f_{\text{survive SN2}} \sim 1$: survival probability after the second supernova

- $f_{\text{merge}} \sim 0.2$: fraction that merge within a Hubble time

The range of final separations is critical because orbital evolution due to gravitational radiation is highly nonlinear, to merge in a hubble time the components must be very close, for example two $10M_{\odot}$ black holes with zero

eccentricity need to be within about $20R_{\odot}$ to merge in 14Gyr (Mandel & Farmer, 2022). Orbital separation is very sensitive to wind mass loss, and this illustrates the importance of a careful treatment of winds.

$$\begin{aligned}
 f_{\text{BBH}} &= f_{\text{primary}} \times f_{\text{secondary}} \times f_{\text{init sep}} \times f_{\text{survive SN1}} \times f_{\text{CE}} \times f_{\text{survive SN2}} \times f_{\text{merge}} \\
 &\approx 0.001 \times 0.5 \times 0.5 \times 1 \times 0.1 \times 1 \times 0.2 = 5 \times 10^{-6} \quad (4.25)
 \end{aligned}$$

Why perform full population synthesis when we could write down a Drake-style equation for a rare system of interest? Because many of these steps involve huge uncertainties that can't be adequately constrained through either theory or observation, using simulation proves a fruitful way to dial in these fractions closely while also exploring physical detail in the process.

Why simulate a whole population when we could simulate one system that will definitely merge? If we simply fine tune parameters of interest to get these rare systems, we find only one of sometimes many (and unexpected) pathways from disparate initial conditions, and also lose information about systems that don't form the system of interest. The statistics make plain the need for a fast code that can generate many examples, balanced with physical realism. Even when downselecting to some more relevant sub-space of initial conditions, many of these processes are still governed somewhat randomly. In a typical COMPAS run, initializing 1 million binaries, already with the parameters tuned for DCOs, will lead to 1-2 thousand objects that merge in a hubble time.

In the various population synthesis codes, the ideal use case and the optimization around it varies. There are also plenty of efforts following similar goals in other related fields, like galactic population synthesis (Bruzual & Charlot, 2003),

or exoplanetary population synthesis (Mordasini, Alibert, Benz, & Naef, 2009).

Our focus remains on rapid binary stellar population synthesis, with the use case tailored to binary black hole mergers.

Table 8. Summary of Major Binary Population Synthesis Codes

Code	Year	Main Use Case	Language	Open Source	Citation
SEBA	1996	Early compact object binary evolution	C / Fortran	No	Portegies Zwart and Verbunt (1996)
BSE	2002	Rapid binary stellar evolution	Fortran	No	Hurley et al. (2002)
STARTRACK	2008	X-ray binaries and GW source populations	C	No	Belczynski et al. (2008)
BPASS	2009	Spectral synthesis with binaries	Fortran / IDL	Yes	Eldridge and Stanway (2009)
BiSEPS	2010	Evolution of millisecond pulsars, cataclismic variables	Fortran	No	Willems et al. (2010)
COMPAS	2018	GW-driven binary compact object formation	C++ / Python	Yes	Riley, Stevenson, et al. (2022)
COSMIC	2019	Rapid Monte Carlo evolution of binaries	Python / C	Yes	Breivik et al. (2020)
POSYDON	2023	rapid/detailed binary stellar evolution using MESA	Python	Yes	Fragos et al. (2023)

CHAPTER V
TRANSIENT GLITCH MITIGATION IN ADVANCED LIGO DATA WITH
GLITSCHEN

This chapter includes coauthored and previously published material. While I am lead author, there were significant contributions from others, where Ben Farr provided the idea for the model design, Zoheyr Doctor provided expert advice on all aspects of parameter estimation, Bruce Edelman contributed coding talent and helped me make the code modular and shareable, and Rachel Hur helped with model testing and explored integration into existing parameter estimation pipelines.

5.1 Introduction

Detecting gravitational waves (GWs) is an immense challenge, requiring the construction and monitoring of the most sensitive interferometers ever built B. Abbott et al. (2016). The strain signal from a loud binary black hole (BBH) inspiral typically perturbs the detectors' arm lengths to one part in 10^{21} . Managing the noise background is an overwhelming portion of that challenge: an earthquake in another hemisphere, a passing vehicle, a cosmic ray hit, a thirsty raven Schofield, Covas, Effler, and Savage (2017), or scattered light from a blinking LED can all bring the data well short of the level necessary for detection et. al. (2021). In spite of a myriad of obstacles, the LIGO-Virgo Collaboration (LVC) has detected 58 confident compact binary coalescence (CBC) events as of the end of the first half of the third observing run (O3a) Collaboration, the Virgo Collaboration, and et. al. (2021); et.al. (2021). Into O4 these observatories may see confident CBC signals upwards of once-a-day Abbott et al. (2020c). Upgrades to the detectors will improve sensitivity and the addition of KAGRA to the LIGO-Virgo-KAGRA network (LVK) will improve astrophysical parameter estimation (PE) and sky

localization. The LVK still expects serious challenges overcoming the noise background, carefully examining more near-threshold triggers, and keeping all the pipelines going with the rapid acquisition of a larger volume of data.

In Advanced LIGO data there are some transient noise sources for which no physical cause has been identified Cabero et al. (2019). These noise sources have the potential to impact astrophysical searches significantly Müller and Anabel (2018). In particular, high-mass and high-mass-ratio BBH searches are affected, in which the astrophysical hypothesis predicts a short duration signal sweeping up into the sensitive frequency bands of the detectors near merger. “Blip” glitches and the lower frequency, longer duration “tomte” glitches are glitch types that are capable of masquerading as these high mass CBCs. These occur on the order of 1/hour Cabero et al. (2019) but sometimes much more frequently, so the probability of coincidence in multiple detectors is non-negligible. Coincident or nearly coincident glitches can confuse search pipelines that strongly rely on coherence between detectors to determine if a trigger is astrophysical. Worse, the effect on the ranking statistic, established by time-sliding data streams from multiple detectors to establish false alarm rates (FARs) Abbott et al. (2020b) is affected significantly by the presence of these glitches in the background, effectively down-ranking many events. There is evidence that these glitches grow louder and more prevalent with increasing sensitivity Soni et al. (2021). Blips and tomtes all but eliminate our ability to evaluate high-mass, extreme-mass-ratio, and extreme-spin single-detector triggers Davis, White, and Saulson (2020) from a confident astrophysical perspective because the data is contaminated with $\mathcal{O}(10^4)$ loud glitches.

GravitySpy Zevin et al. (2017) is a pipeline developed to classify glitch types. It leverages citizen science with an image recognition neural network, specifically trained on q-transforms, which display power in time-frequency pixels Chatterji, Blackburn, Martin, and Katsavounidis (2004). Thanks to these efforts, there are now over 10^6 glitches classified, each with an associated confidence metric and SNR Zevin et al. (2017). GravitySpy itself can be used to effectively distinguish different types of glitches from each other, but it can't be used to distinguish signal from glitch, or to subtract glitches from data. For this we seek a parametric, *generative* model for common glitch types. Barring the discovery and mitigation of possible environmental, electronic, or instrumental causes Braginsky, Ryazhskaya, and Vyatchanin (2006); Helmling-Cornell (n.d.); Yamamoto et al. (2008) for these problematic classes of glitch, distinction between glitch-like astrophysical events and BBH signals that resemble common and problematic glitch types may be our only tractable method for opening up the high-mass and high-mass-ratio region of CBC search parameter space.

With the *glitschen* package, we propose a data-driven, easy to use, and computationally cheap framework for the modeling of short duration transient glitches. Our model uses an analytical maximum likelihood estimation (MLE) approach to fit a probabilistic principal component analysis (PPCA) model to all of the training data, operating under the hypothesis of a transient glitch superimposed on Gaussian noise Tipping and Bishop (1999). While PCA's have previously been used in the context of glitch categorization Powell et al. (2017); Powell, Trifirò, Cuoco, Heng, and Cavaglia (2015), we focus on the construction of glitch-class-specific parameterized models for glitch *mitigation*. Relative to other glitch mitigation techniques Cornish (2021); Cornish and Littenberg (2015); Cornish

et al. (2021); Mukherjee, Obaid, and Matkarimov (2010); Torres-Forné, Cuoco, Font, and Marquina (2020), these targeted parameterized models have minimal flexibility and are in many ways analogous to the parameterized CBC models used to search for and characterize signals, making them straightforward to incorporate in existing LVK analyses. In comparison to current glitch mitigation techniques such as BAYESWAVE (BW) Cornish and Littenberg (2015), our approach naturally allows for informed priors, allowing us to leverage the extensive glitch population. Our approach can be naturally used in existing analysis libraries such as BILBY, whereas BW’s use of reverse-jump sampling means that only a point estimate from BW can be used to remove a glitch during astrophysical parameter inference. While powerful, our methods require large training sets for each glitch type and will likely be unable to model glitches that are extensive in time-frequency, such as scattered-light.

5.2 Method

5.2.1 Modeling the Advanced LIGO Noise Background. The noise in the detector is a superposition of many noise sources, and is modeled as a stochastic process, drawing randomly from a stationary background spectrum at each frequency “<https://onlinelibrary.wiley.com/doi/abs/10.1002/9783527636037.fmatter>” (n.d.). The detector produces a time series, $n(t)$, which we can represent as a vector, \mathbf{n} . Transforming to the frequency domain we obtain $\tilde{\mathbf{n}}$, with n_i indicating the noise in the i -th frequency bin. Assuming Gaussianity the probability distribution becomes:

$$p(\tilde{\mathbf{n}}) = \frac{1}{\det(2\pi\mathbf{C})^{1/2}} \exp\left[-\frac{1}{2} \sum_{ij} (\tilde{n}_i - \mu)(\tilde{n}_j - \mu) C_{ij}^{-1}\right] \quad (5.1)$$

where $\mathbf{C}_{ij} = \frac{1}{M-1}(n_i - \mu)(n_j - \mu)$ is the covariance matrix of the observations and μ is the mean of the data Abbott et al. (2020b). Stationarity means that the noise

spectrum is not changing over time, so in the frequency domain the covariance matrix is diagonal: $C_{ij} = \delta_{ij}S_n(f_i)$, giving the power spectral density (PSD), $S_n(f)$ which is equal to the square of the amplitude spectral density (ASD). The noise is typically stationary on the timescales (minutes) relevant for PSD computation, but on the hour timescale may need to be updated Abbott et al. (2020b).

We “whiten” the data by dividing the frequency domain data by an estimate of the ASD, resulting in noise with an equal (unitary) noise in all frequencies. We train and test our model using whitened data.

This treatment is highly effective for ‘well-behaved’ noise sources which remain stationary over the duration of ASD calculation, however the motivation for building our model is to mitigate transient glitches, which can occur at any time and pose the greatest challenge for searches that look for transient astrophysical events.

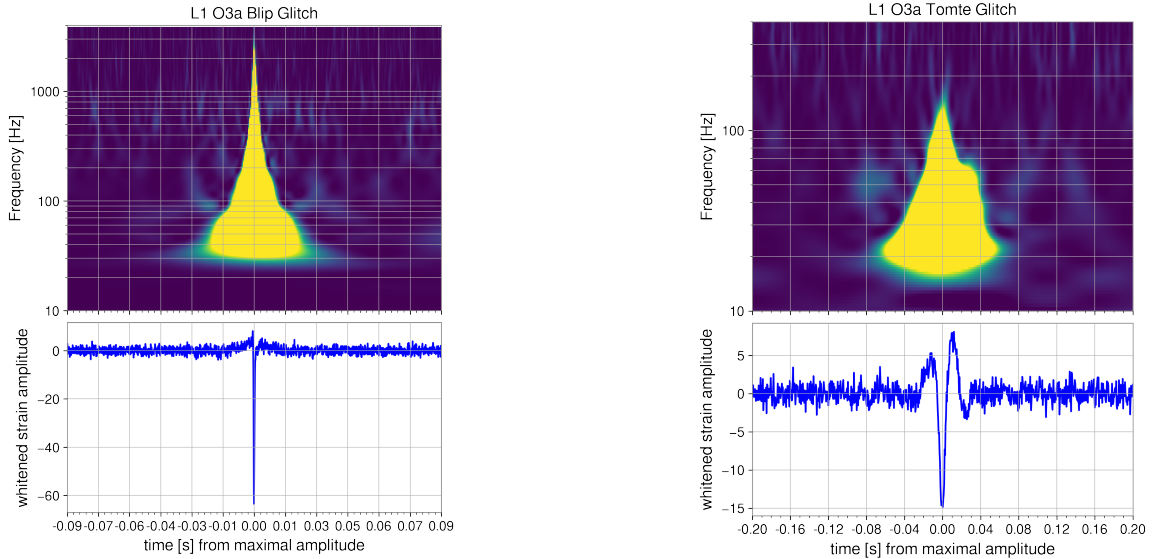


Figure 9. Typical loud blip (above) and tomte (below) glitches from the test set for Livingston in O3a, to demonstrate morphology. Q-scans indicate power as color in time-frequency pixels, and the timeseries (below in blue) shows additional morphology. Note that timescales and frequency ranges plotted vary. Blips are sometimes shorter than 5ms, where tomtes can last over 100ms.

5.2.2 The Transient Glitch Background. The characteristics of the noise background are well covered in Abbott et al. (2020b); et. al. (2021); Soni et al. (2021); Zevin et al. (2017). The morphologies of a typical ‘blip’ and ‘tomte’ glitch are explored in Figure 9. Blip glitches are short, at around 5-10ms, while Tomtes are typically 100ms long. To properly mitigate these glitches we examine their morphology as they appear to searches, *after* any whitening and postprocessing. Physically, it is possible that the glitches are a very brief DC offset that appears in the strain channel, the result of either a single physical perturbation to some component of the detector or the result of a digital error. We will have to consider the additional morphology of finite impulse response whitening filters as being part of the glitch, since the searches must also contend with these features.

While GravitySpy examines q-transforms Chatterji et al. (2004) of glitches, we train on the frequency series of glitches. There is a loss of phase information and direction of amplitude in q-transforms, which record only power for each time-frequency pixel. This may be important for future efforts in distinguishing auxiliary witnesses for these glitches, since a preferential directional perturbation to a part of the detector could show up as a bias in amplitude (positive or negative) in the strain channel for a certain detector and glitch type. We have yet to determine if this is a bias introduced in GravitySpy’s curation of the highest confidence and loudest glitches, or if this extends to the large number of lower confidence glitches as well, but we see a vast majority of confident, loud L1 O3a tomtes with negative amplitudes. Other detectors and glitch types exhibit a certain “glitch-signature” in amplitude bias, sometimes across multiple observing runs.

5.2.3 The *glitschen* Model. In the *glitschen* parametric glitch mitigation model, we employ probabilistic principal component analysis (PPCA). This is a simple and effective way for us to decompose a frequency domain signal into a set of Gaussian distributed latent variables. It is frequently used as a dimensionality reduction tool, making problems in many areas of data science more tractable. There are many ready-made principal component analysis (PCA) implementations available. We found it most transparent and effective to write our own PPCA implementation, closely following the original PPCA model Tipping and Bishop (1999). This enabled us to find a fast and computationally cheap way to analytically maximize our likelihood. PPCA differs from PCA in that it includes a Gaussian noise term.

We employ an isotropic Gaussian noise model:

$$\mathcal{N}(\mathbf{0}, \sigma^2 \mathbf{I}) \tag{5.2}$$

with a d -dimensional observation vector, $\tilde{\mathbf{d}}$:

$$\tilde{\mathbf{d}}|\mathbf{Z}_{train} \sim \mathcal{N}(\mathbf{W}\mathbf{Z}_{train} + \boldsymbol{\mu}, \sigma^2\mathbf{I}) \quad (5.3)$$

We assume the marginal distribution $\mathbf{Z}_{train} \sim \mathcal{N}(\mathbf{0}, \mathbf{I})$ over q latent variables of the training set, and \mathbf{W} has size $d \times q$, containing q training eigenvectors. We recover normal PCA in the limit of $\sigma \rightarrow 0$. We can marginalize over the latent variables to obtain a distribution for $\tilde{\mathbf{d}}$:

$$\tilde{\mathbf{d}} \sim \mathcal{N}(\boldsymbol{\mu}, \mathbf{C}) \quad (5.4)$$

where $\mathbf{C} = \mathbf{W}\mathbf{W}^T + \sigma^2\mathbf{I}$ is the covariance model for the observed data, with dimension $d \times d$. In our case this data is frequency-series data. With N training glitches, our log-likelihood for the entire model and all our observed (training) data is then:

$$\ln \mathcal{L}_{training} = -\frac{N}{2} \left[d \ln(2\pi) + \ln |\mathbf{C}| + tr(\mathbf{C}^{-1}\mathbf{S}) \right] \quad (5.5)$$

with the sample covariance matrix of the observations, \mathbf{S} :

$$\mathbf{S} = \frac{1}{N} \sum_{n=1}^N (\tilde{\mathbf{d}}_n - \boldsymbol{\mu})(\tilde{\mathbf{d}}_n - \boldsymbol{\mu})^T \quad (5.6)$$

This likelihood is often maximized iteratively, and many packaged implementations of PPCA find W in this way Dillon et al. (2017). However we find the global maximum of the likelihood using an analytical method detailed in Tipping and Bishop (1999).

Later, we use this likelihood, with an Occam’s penalty accounting for the effective degrees of freedom in the model, to find the optimal number of components, q , to use. Performing an eigenvalue decomposition on \mathbf{S} , the sample covariance matrix of the observations, we obtain the $d \times q$ matrix \mathbf{U}_q containing q principal eigenvectors (or “eigenglitches”) of \mathbf{S} , and the $q \times q$ diagonal matrix $\boldsymbol{\Lambda}_q$ with coresponding eigenvalues. All eigenvalue decompositions and matrix

inversions are conveniently handled by an open-source computer algebra library with numpyvan der Walt, Colbert, and Varoquaux (2011). The likelihood is maximized when:

$$\mathbf{W} = \mathbf{W}_{ML} = \mathbf{U}_q(\mathbf{\Lambda}_q - \sigma^2\mathbf{I})^{1/2} \quad (5.7)$$

Going forward, we can consider $\mathbf{W} = \mathbf{W}_{ML}$ to always contain the maximum likelihood (ML) eigenvectors. See an example time-domain representation in the figure below.

In order to obtain a projection of a new observation vector, $\tilde{\mathbf{d}}_{obs}$, onto the latent variables we use Bayes rule to get from $\tilde{\mathbf{d}}|\mathbf{Z}_{train}$ to

$$\mathbf{Z}_{train}|\tilde{\mathbf{d}}_{obs} \sim \mathcal{N}(\mathbf{M}^{-1}\mathbf{W}^T(\tilde{\mathbf{d}}_{obs} - \boldsymbol{\mu}), \sigma^2\mathbf{M}^{-1}) \quad (5.8)$$

where $\mathbf{M} = \mathbf{W}^T\mathbf{W} + \sigma^2\mathbf{I}$, with dimensions $q \times q$. This allows us to perform reconstructions of suspected glitches using a trained model. We define

$$\mathbf{Z}_{rec} \equiv \mathbf{M}^{-1}\mathbf{W}^T(\tilde{\mathbf{d}}_{obs} - \boldsymbol{\mu}) \quad (5.9)$$

as the set of q latent optimal (i.e., maximum likelihood) reconstruction weights up to an arbitrary rotation matrix.

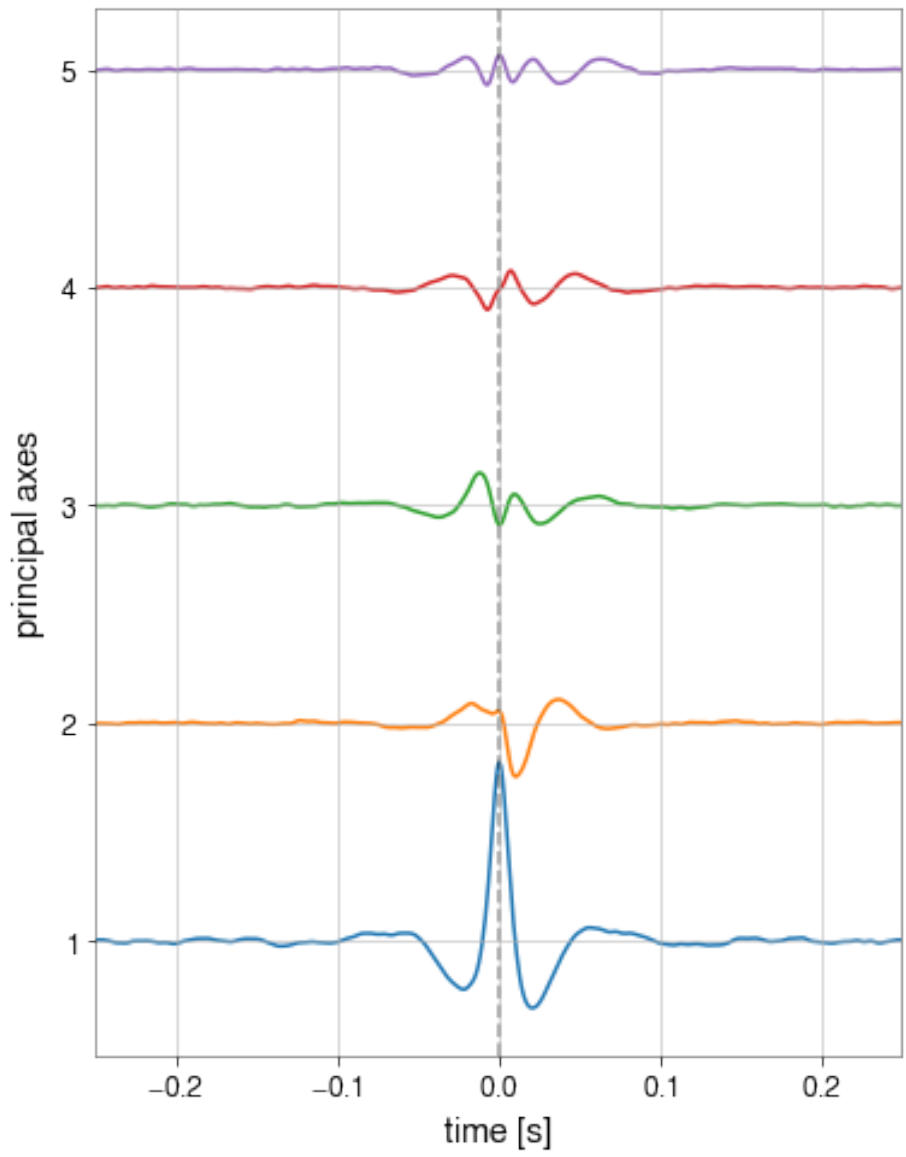


Figure 10. L1 O3a tomte glitch model eigenvectors. Increasing weight from top to bottom.

We can obtain a reconstruction with:

$$\tilde{\mathbf{g}}_{rec} = \mathbf{W} \mathbf{Z}_{rec} + \mu \quad (5.10)$$

To evaluate the quality of our reconstruction given the data, we employ the standard Gaussian noise likelihood, identical to that used by CBC searches and PE, and specifically BILBY Ashton et al. (2019). We define the standard noise weighted inner product of any two frequency-series vectors, \mathbf{a} and \mathbf{b} :

$$(\tilde{\mathbf{a}}|\tilde{\mathbf{b}}) = 2 \int_0^\infty \frac{\tilde{a}(f)\tilde{b}^*(f) + \tilde{a}^*(f)\tilde{b}(f)}{S_n(f)} df \quad (5.11)$$

$S_n = \sigma^2$ is the noise power spectral density (PSD), and σ is the amplitude spectral density (ASD) Abbott et al. (2020b). In practice, the noise term can be taken to be 1, because the model is trained on whitened data. When we assume stationary, Gaussian noise that is uncorrelated between detectors, our reconstruction log-likelihood becomes:

$$\ln \mathcal{L}_{rec} = -\frac{1}{2} \sum_k \left\{ \frac{|\tilde{\mathbf{d}}_{obs,k} - \tilde{\mathbf{g}}(\theta)_{rec,k}|^2}{S_k} + \ln(2\pi S_k) \right\} \quad (5.12)$$

where k is the frequency bin index $\tilde{\mathbf{g}}(\theta)_{rec,k}$ is the frequency domain reconstruction with PPCA parameters θ . With this inner product and likelihood we can compare our model's reconstruction of an event, after training on a certain glitch class, with the likelihood of the astrophysical hypothesis. We can select q based on an Occam's penalty, or we can try to replicate the number of effective free parameters in the CBC model to give equal flexibility.

5.2.4 Implementation and Performance.

5.2.4.1 Selection of Training Data. We curate glitches classified by GravitySpy Zevin et al. (2017) with high 'confidence', where the score ranges from (0,1). Note that confidence is not a normalized probability, but instead

reflects the certainty of classification by the convolutional neural network used. We utilize the newest, LVK-internal version of the GravitySpy model, which has the benefit of training on data from all of O3. Publicly available glitch and event data can be obtained from the Gravitational Wave Open Science Center (GWOSC) Abbott, Abbott, et al. (2021). This analysis was completed using an older version of the calibrated data: the HOFT_C00 strain data frame within the GDS-CALIB_STRAIN_CLEAN channel. Note that some ($< 1\%$) of the glitches used in training are outside of “science mode” times.

All glitches used first must clear our confidence cutoff(0.95-1, depending on type, detector, and epoch), and are then sorted by SNR. Lower SNR glitches can contaminate the model with more unrelated noise features. As such, we have kept a high SNR threshold for inclusion in training(dependent on type, detector, and epoch), where we use the 1500-2000 loudest glitches. It is more productive to limit the set to “golden” examples curated by GravitySpy, even if the glitch or event in the run segment has low SNR, since we believe quiet and loud glitches (5-50 SNR) exhibit similar morphology, based on our exploration of the data.

5.2.4.2 Preprocessing and Training. To train our model, we whiten with an ASD calculated from between 16 and 128 seconds of data, depending on the glitch-type in question. Because we are concerned with the low-frequency content of glitches (in the range of astrophysical searches) all data is downsampled to 2048 Hz, and then for certain glitchtypes we further bandpass training data to aid in reconstruction efficiency. For Tomte glitches, which have a peak frequency around 50-60 Hz, a 10-128 Hz bandpass to the training data ensures we are not overfitting noise outside the glitch time, but still recover more than 99% of the SNR from more than 99% of training glitches. We find that 0.5s

training window is always adequate for tomtes, with typical duration 0.1s. For blips, peak frequencies are typically 500-1000 Hz, so we obtain similar recovered SNR by bandpassing from 10-1024 Hz. We find that a 0.1s window is almost always adequate for blips (allowing one full cycle at 10 Hz). Blips are shorter in duration (almost always shorter than 30ms). For run segments on test glitches and marginal/glitch-like events we keep data in 10-2048 Hz, retaining higher frequency noise. All training examples are centered on the peak amplitude time sample. All preprocessing is performed using open-source libraries including NUMPY van der Walt et al. (2011) and GWPY Macleod et al. (2021).

5.2.4.3 Performance. The model is easily run and bench-marked on a laptop with six cores. The training process takes less than 1 second for 2000 glitches. Maximum likelihood reconstruction takes 1ms-1 μ s depending on how much leeway in center time we allow. Sampling proceeds quickly, giving 10,000 independent samples of the posterior distribution in about 5 minutes, depending on the glitch.

By weighing the likelihood against an Occam’s penalty, we can ensure our model has the appropriate number of dimensions (q) and is not over fitting. We employ a Laplace approximation to the marginal likelihood Minka (2000), along with the Bayesian information criterion, described further in appendix A, to choose the optimal number of eigenvectors for calculating the residuals of the test sets, in the next section. To roughly match the degrees-of-freedom (per-detector) of the CBC model, we employ $q = 5$ in all sampled cases.

5.3 Results

5.3.1 Testing with Maximum Likelihood Reconstruction.

We reserve 10% of glitches for testing (the model has never encountered these

examples), and to evaluate the performance of our model we examine residuals after maximum likelihood reconstruction and subtraction, as seen in Figure 3 histograms. This demonstrates the efficacy of the model in mitigating an entire class of glitches. Test sets shown include 100-200 glitches. We will soon extend this to cleaning entire search backgrounds, and attempt re-ranking of CBC searches.

We plot residuals after glitch subtraction in the frequency domain. They obey a Gaussian distribution after perfect glitch cleaning under the hypothesis of stationary, uncorrelated noise. Cleaning models are trained with the automatic choice of dimensionality via Laplace approximation (described in Appendix A): (15, 2, 9, 8), for H1 blips(truncated from 23 to 15), H1 tomtes, L1 blips, L1 tomtes, respectively.

The binning in Figure 11 extends down to single samples from single test glitches, showing that for all classes and detectors our results are consistent with Gaussian noise. The performance is somewhat higher for tomte glitches, mainly due to the greater homogeneity in their morphology compared to blips. Tomtes in Livingston were 10-20 times more prevalent than in Hanford Soni et al. (2021). This has been partly attributed to Livingston operating at greater sensitivity than Hanford during O3a, but may also be to to unknown environmental factors. It is observed that blips and tomtes are louder at higher sensitivity. Higher SNR and greater numbers allow for better modelling, but show the increasing importance of mitigation as sensitivity improves in future observing runs.

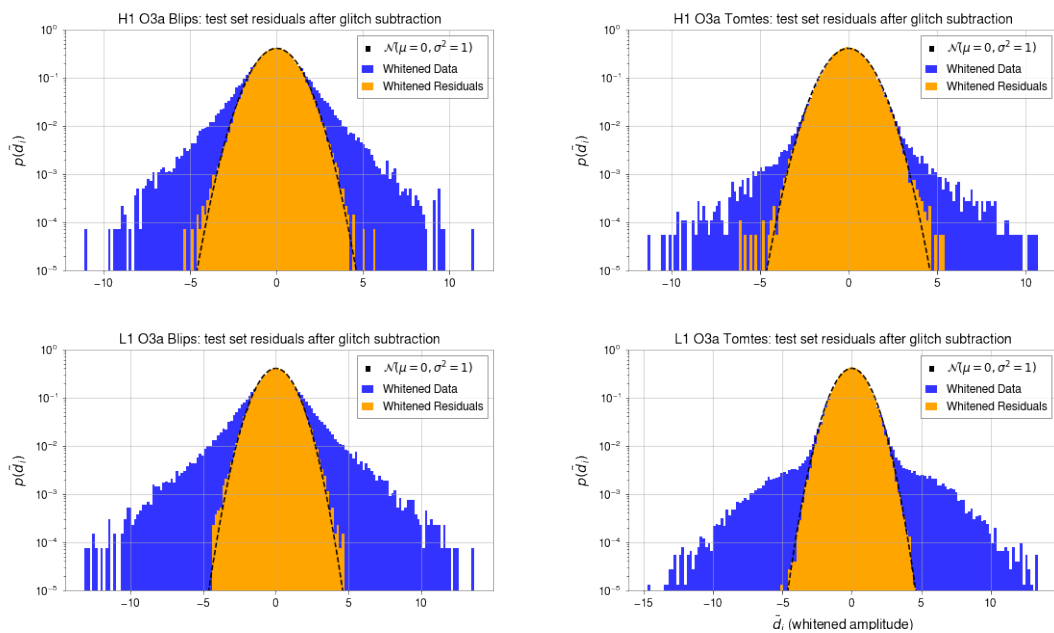


Figure 11. Frequency-domain residuals after subtraction from the test set (10%) reserved from each glitch type, detector, and epoch. The bins are scaled such that the lowest visible represent single samples from single glitches. Note that extremal samples are louder in Livingston. It has been observed that with greater sensitivity and range transient glitches become louder as well Soni et al. (2021).

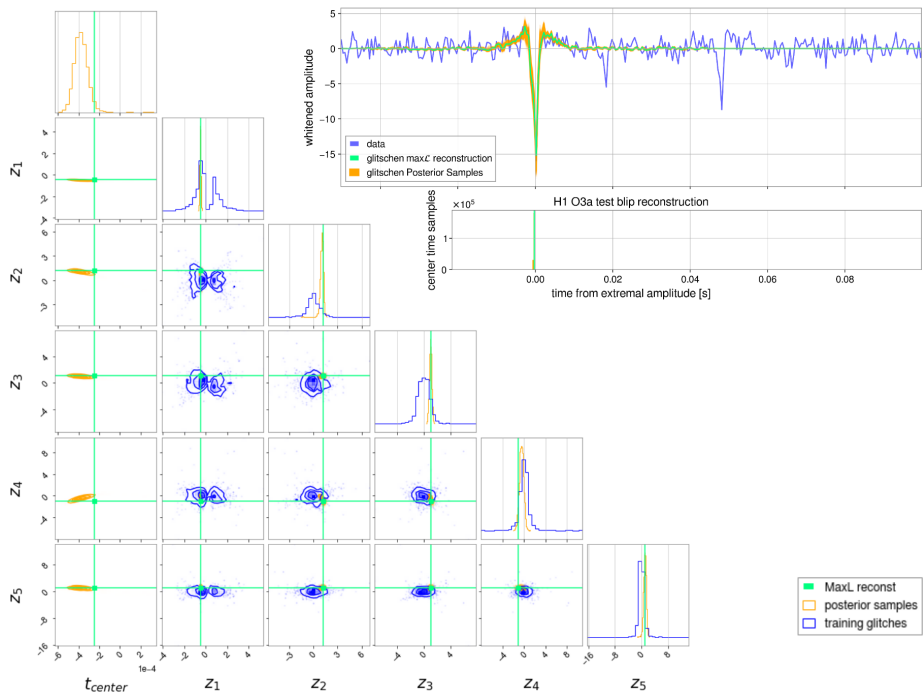


Figure 12. H1 O3a test blip: full posterior estimation. Note the repeating blips afterward. This example shows the tendency of the sampler to converge on the loudest glitch available. The histogram of center time samples shows high certainty (just below the timeseries reconstruction). In the corner plot for the latent space weights (z_1 - z_5), we see that this test set glitch is typical of the class.

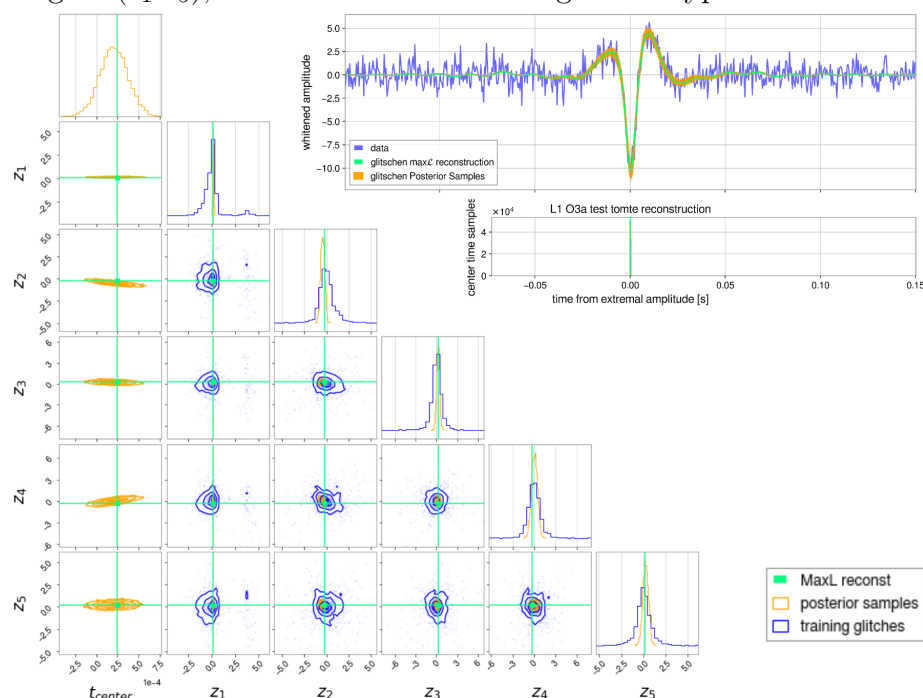


Figure 13. L1 O3a test tomte: full posterior estimation. This is a very typical tomte glitch, with all walkers converging on the same center time, low uncertainties in the timeseries reconstruction, and the posterior distribution aligning well with the distributions on the training set latent weights.

5.3.2 Sampling. We employ two well developed MCMC toolkits, EMCEE Foreman-Mackey, Hogg, Lang, and Goodman (2013), and KOMBINE Farr and Farr (2015), to perform a full Bayesian posterior estimation of our reconstruction. By allowing the center time of the hypothesized glitch to vary, we sample in $q+1$ dimensions. A priori, we assume glitches are equally likely at any time, and thus adopt a uniform prior in center time. The localization of the samples in center time is a good indicator of how glitchlike the morphology of the test signal is. To aid in the efficiency of sampling, we initialize walkers in a Gaussian around the suspected glitch time. In the q PPCA weights, we use a less restrictive wide Gaussian prior, or alternately a highly-informed KDE (kernel density estimate) prior based on the entire training set’s maximum likelihood weights. The latter is generally more restrictive and can limit the flexibility of the sampler to fit more general morphologies, which in some cases may be ideal, and in others can to be adjusted. For all MCMC sampled example glitches and CBC comparisons in the paper, we employ $q = 5$.

In Figures 12 and 13 we demonstrate the results of sampling on a test blip in Hanford, and a test tomte in Livingston. The blip was chosen specifically due to it’s proximity to further repeating blips. The sampler converges easily on the loudest glitch-like event in the run-segment.

5.3.3 Signal Safety Testing. To establish the model’s capability of distinguishing glitch from astrophysical signal, we test if it remains flexible enough to fit different glitch morphologies while being (appropriately) unable to reconstruct and subtract an astrophysical signal. We run our model on a selection of high-mass, short duration BBH signals from GWTC-2 et.al. (2021), acquiring data from the Gravitational Wave Open Science Center(GWOSC)Abbott,

Abbott, et al. (2021). Specifically, we choose events with high detector frame chirp masses (and by extension, short template durations), and FAR (False Alarm Rate) $< 10^{-3}/yr$. Being the confirmed astrophysical signals with morphology closest to short transient glitches such as blips and especially tomtes, these provide a good opportunity to confuse the model. We quote maximum likelihood single detector SNR values for the CBC and alternately the glitch hypotheses in Table 9. Quoted durations are the template duration for the preferred trigger from low latency detection. Two events had H1 offline at the trigger time but were included for their glitchlike morphology. We anticipate that an effective glitch model may be instrumental in vetting single-detector events in the future.

For a more rigorous comparison between the CBC and glitch models we employ a full posterior estimation framework and the Deviance Information Criterion (DIC). This is a variance based approach. The DIC is given by:

$$DIC = D(\bar{\theta}) + \overline{\text{var}(D(\theta))} \quad (5.13)$$

Where the deviance, D , is: $D(\theta) = -2 \ln(p(d|\theta))$ with posterior distribution p , data y , and parameters θ . Given the log likelihoods from samples obtained using both the Glitchen model and a CBC PE run we see that the glitch hypothesis is heavily disfavored for all events tested. These comparisons appear in Table II, where a lower DIC value indicates a better model for the observed data.

5.3.4 GW190521: testing our model’s limits with the most massive (and glitch-like) confident O3a event. GW190521 is the highest mass ($142_{-16}^{+28} M_{\odot}$) and shortest duration (0.1s) CBC event for which we have strong evidence ?. Being a loud triple detector event, it is confidently of astrophysical origin. But for us, it offers a unique opportunity to test our model, since it exhibits signal morphology which is the most “glitch-like” of all high significance

Event Information			Matched-Filter SNR					
Event Name	$\mathcal{M}_{\text{det}}, M_{\odot}$	duration(s)	CBC H1	Tomte H1	Blip H1	CBC L1	Tomte L1	Blip L1
GW190521	$114.8^{+15.2}_{-17.6}$	0.15	7.87	4.11	3.21	12.38	5.93	4.06
GW190602.175927	$72.9^{+10.8}_{-13.7}$	0.22	6.56	3.60	3.55	11.02	4.43	4.88
GW190706.222641	$75.1^{+11.0}_{-17.5}$	0.15	9.07	4.91	4.22	9.18	3.92	3.93
GW190519.153544	$65.1^{+7.7}_{-10.3}$	0.17	9.50	4.42	4.76	11.85	5.42	4.25
GW190620.030421	$57.5^{+9.0}_{-11.2}$	2.3	(offline)	-	-	11.70	3.78	4.63
GW190910.112807	$43.9^{+4.6}_{-3.6}$	1.8	(offline)	-	-	13.86	6.29	4.26
GW190521.074359	$39.8^{+2.2}_{-3.0}$	0.24	12.67	5.85	6.30	22.68	8.83	7.24

Table 9. Selecting short duration, heavy BBH mergers we provide an important test for the model, which should give lower SNRs than the CBC model. Events are in order of detector frame chirp mass ($\mathcal{M}_{\text{det}}, M_{\odot}$). For all of these events we see lower SNRs by a factor of 2-3, whereas we expect to recover nearly all of the SNR in confirmed glitches. CBC parameter estimation results from et.al. (2021).

Event Name	Deviance Information Criterion (DIC)					
	CBC H1	Tomte H1	Blip H1	CBC L1	Tomte L1	Blip L1
GW190521	-54.6	-5.4	8.7	-130.3	-26.7	9.94
GW190602.175927	-37.3	10.2	8.7	-105.6	-5.6	12.0
GW190706.222641	-71.0	13.2	9.6	-74.0	14.8	8.1
GW190519.153544	-87.7	18.4	-18.6	-145.2	25.1	13.1
GW190620.030421	-	-	-	-133.9	17.5	12.5
GW190910.112807	-	-	-	-190.3	-28.5	17.7
GW190521.074359	-152.8	34.0	36.4	-494.5	-67.1	-45.3

Table 10. Running samplers on these events, we obtain the DIC from our distributions of log likelihoods. The deviance information criterion (DIC) favors models with a lower value. The CBC model is highly preferred to the glitch model in all cases, indicating that pass the signal safety test.

astrophysical events. It spent only the last 4 cycles of its inspiral in the sensitive band of the detector, peaking at 60Hz. Tomte glitches look very similar.

Critically, any model for tomtes, at bare minimum, must not be confused by such an event. Because the aim of improved glitch mitigation is to open up this high mass region of parameter space, this is precisely the kind of test we need to pass. Here we demonstrate our full posterior estimation framework on GW190521, and by extension, our ability to distinguish glitch-like astrophysical events from glitches by comparing our glitch hypothesis results with the astrophysical hypothesis results.

In both L1 and H1 (Figures 14 and 15, respectively), we see that the glitch model (MaxL glitch reconstruction in green) is unable to fully capture the signal morphology, with the MaxL CBC reconstruction in black, no matter where it is placed. It remains multi-modal in center time, and an outlier in most of the training set weights, indicating that this is a poor fit to the data, as we expect. High uncertainty is seen in the broadness of the posterior reconstructions, in orange on the timeseries plots. See Tables I and II for a more quantitative comparison of the glitch and CBC hypothesis, for this and other events in O3a.

5.4 Conclusion and Future Work

We have introduced a PPCA-based approach to modeling transient noise in gravitational wave detector data, implemented in the open-sourced *glitschen* package, publicly available here: ¹. We welcome collaborative development, testing, and feedback.

For both ‘blip’ and ‘tomte’ glitches – some of the most impactful for BBH searches in O3 – we have demonstrated the effectiveness of the model for glitch

¹<https://git.ligo.org/jonathan.merritt/glitschen>

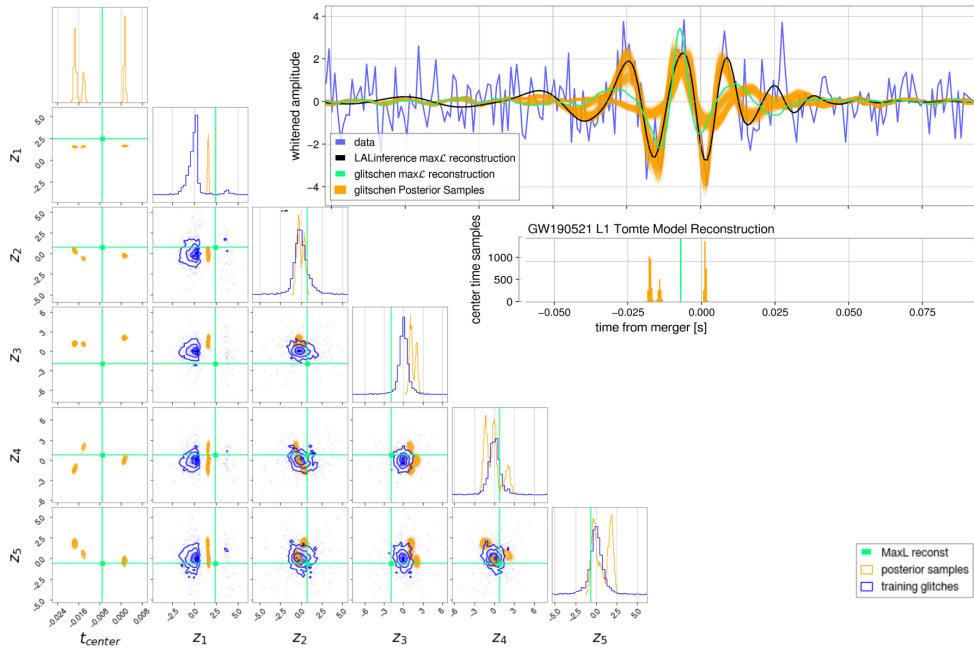


Figure 14. GW190521 Full Posterior Estimation, L1. The distribution in the center time is multi-modal, indicating that the glitch model fails to capture the full morphology of the signal (LALINFERENCE maxL in black), no matter where it is placed. The reconstruction features high uncertainty (samples in orange), and the posterior distribution in the latent variables lies outside the training set of glitches. All of this indicates that the model has failed to reconstruct GW190521 as a glitch, as expected.

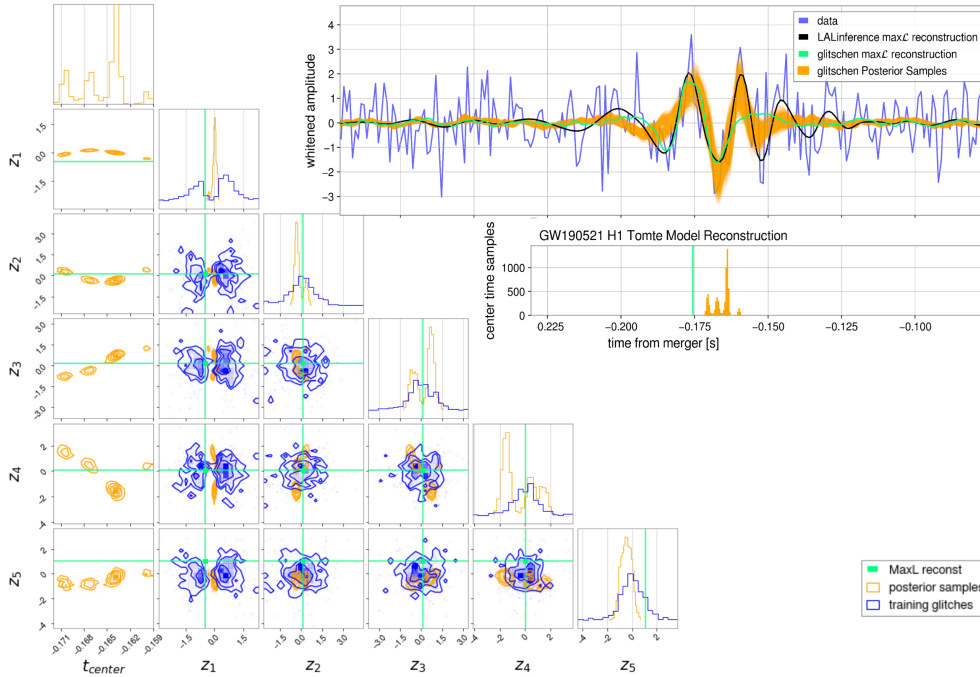


Figure 15. GW190521 Full Posterior Estimation, H1

subtraction, as well as for Bayesian model comparisons with astrophysical signal models.

In future work we will explore the use of clustering algorithms in PPCA space for glitch classification and sub-classification. We will test the effectiveness of the model in reducing the background for compact binary searches. We will also integrate our model into the BILBY Ashton et al. (2019) parameter estimation code, where composite signal and noise models will allow us to marginalize over glitch morphology when glitches are coincident with astrophysical signals.

We tested our model on high-mass events from O3a, but in the future we will extend this testing to simulations in the high-mass *and high mass-ratio* region of parameter space, where discoveries are still to be made and distinguishing astrophysical events from noise is even more difficult.

Because burst searches also trigger on glitches, we plan to test our model in this regime. Searches for cosmic string cusps, supernova templates, and all agnostically un-modeled sources could radically change the field, but only if we can work on the serious blind-spots in our searches. We have already began an injection campaign with cosmic string templates in the parameter space contaminated by blip glitches to determine our ability to differentiate signal from glitch in this context. We plan to extend the use of our model beyond Blips and Tomtes, but because these are the most impactful for BBH searches, they remain the first and most important testing ground.

With more accurate models of glitches, we can improve the detectability and significance of gravitational wave events of all kinds.

5.5 Acknowledgements

Here we thank the GravitySpy team, the detector characterization working group, and everyone who made this effort possible. We're grateful to the CBC, Detchar, and Parameter Estimation groups for their hard work building powerful software tools and tutorials and organizing workshops that help make LIGO data analysis work more accessible.

The authors are grateful for computational resources provided by the LIGO Lab (CIT, LHO, LLO) and supported by National Science Foundation Grants PHY-0757058 and PHY-0823459. This material is based upon work supported in part by the National Science Foundation under Grant PHY-2110636. We are grateful for the following open-source software tools: NUMPY (van der Walt et al., 2011), SCIPY (Virtanen, Gommers, & SciPy 1.0 Contributors, 2020), GWPY (Macleod et al., 2021), MATPLOTLIB (Hunter, 2007), BILBY (Ashton et al., 2019).

5.6 Optimal Choice of the Model Dimensionality

To avoid over or under fitting we can use various metrics to find the optimal number of PPCA eigenvectors to employ for each glitch type, detector, and observing run. We tried a crude method: fraction of recovered SNR in test set glitches. If we recover .99 of the known glitch SNR then any gains added with additional dimensions are giving diminishing returns. However this cutoff point is somewhat arbitrary. Instead, balancing an Occam’s penalty against the model’s training set likelihood is a much more rigorous approach. We employed several methods, including the Akaike information criterion (AIC), the Bayesian information criterion (BIC), and the Laplace approximation to the marginal model log-likelihood, following the method in Minka (2000). By maximizing these metrics we can use the optimal level of model complexity. To arrive at the Laplace approximation, we apply an uninformative conjugate prior on the model parameters and marginalize over everything but q , the PPCA dimensionality. The marginal log-likelihood values are estimates of the model evidence and the ratio of these for different q can be taken as Bayes factors, so far as the Laplace approximation is accurate, which we show in Figure 16.

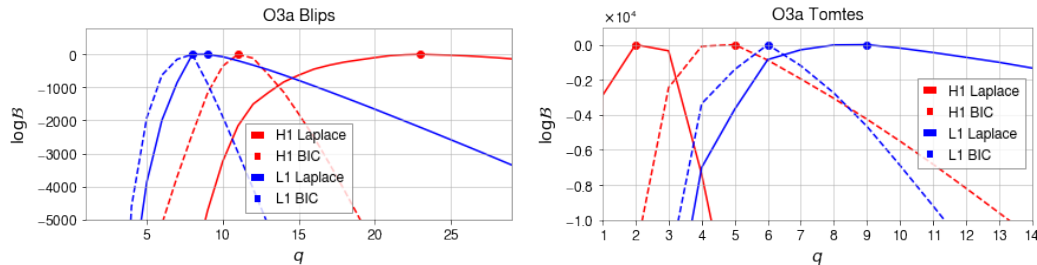


Figure 16. The relative Bayes factors as a function of dimensionality, q , for each detector and glitch type in the analysis. The peak of these curves allow for an automatic choice of dimensionality that avoids over-fitting.

CHAPTER VI

IMPLICATIONS OF MODERN MASS-LOSS RATES FOR MASSIVE STARS

This project is coauthored and unpublished material, we are in the late stages of internal review, and hopefully by the time this thesis is submitted we will also have submitted this work to a journal. While I am the the lead author, I worked most closely with Simon Stevenson on all aspects of background research and code development, was brouintoo the collaboration and the project by Ilya Mandel, used code primarily written by Jeff Riley, and received expert theoretical advice on the physics of stellar winds from Andreas Sander. My advisor Ben Farr helped me with significant portions of the analysis, Holden Jose, an undergraduate at the time of this work, performed exploratory runs of the code with me. Lieke van Son, Tom Wagg, and Serena Vinciguerra paved the way for this work with contributions to the code and extensive exploration and understanding of the impact of stellar winds. This work centered on exploring the impact of metallicity on the final outcomes for massive systems, and I contributed somewhat peripherally to *Not Just Winds: Why Models find Binary Black Hole Formation is Metallicity Dependent, While Binary Neutron Star Formation is Not*, with lead author Lieke Van Son (not described directly here).

6.1 Introduction

Massive stars (with initial masses $> 8 M_{\odot}$) experience significant mass loss through stellar winds throughout their lives, losing a sizable fraction of their initial mass. These stars are the progenitors of supernovae, neutron stars and black holes. There are large uncertainties in both theoretical predictions for, and observations of, the mass-loss rates of massive stars.

Massive stars preferentially form in binaries (e.g., Sana et al., 2012). The evolution of massive binaries can lead to the formation of merging compact binaries (e.g., Mandel & Farmer, 2022; Mapelli, 2021; Tutukov & Yungelson, 1973; van den Heuvel & De Loore, 1973).

The landscape of compact binary astrophysics is expanding rapidly with the rapidly growing catalogs of compact binary mergers detected in gravitational waves (GWs) by the LIGO-Virgo-KAGRA (LVK) collaboration (Abbott et al., 2023), and the detection of detached Galactic black hole binaries by Gaia (El-Badry, 2024; El-Badry et al., 2023; Panuzzo et al., 2024). One of the greatest uncertainties in determining the evolutionary fates of massive stars and binaries is mass loss through stellar winds.

In recent years, increasingly sophisticated models of mass loss have been developed for various phases of stellar evolution (e.g., Krtićka & Kubát, 2017, 2018; A. A. C. Sander & Vink, 2020). At the same time, empirical mass loss prescriptions for evolved stars have benefited from increasingly large samples of massive stars from new observational surveys (e.g., Shenar et al., 2019; Yang et al., 2023).

When incorporated into detailed stellar evolution or stellar population synthesis codes, these updated wind prescriptions allow us to improve the modeling of a plethora of products of massive binary stellar evolution. We can generate populations of compact binary mergers and compare them to recent GW observations (e.g., Broekgaarden et al., 2022; Stevenson & Clarke, 2022), populations of massive supernova progenitors observed in the local Universe (e.g., Davies & Beasor, 2020; Smartt, Eldridge, Crockett, & Maund, 2009) and stellar-mass black holes in binaries in the Milky Way (e.g., Miller-Jones et al., 2021; Panuzzo et al., 2024).

Prescription Set Name	OB	RSG	VMS	WR
New Defaults (MERRITT2024)	Vink and Sander (2021)	Decin et al. (2024)	Sablahit, Vink, Sander, and Higgins (2023)	A. A. C. Sander et al. (2023), Vink (2017)
PESSIMISTIC	Vink and Sander (2021)	Vink and Sablahit (2023)	Bestenlehner (2020)	Shenar et al. (2019)
Old Defaults (BELCZYNSKI2010)	Vink, de Koter, and Lamers (2000); Vink et al. (2001)	Nieuwenhuijzen and de Jager (1990)	Vink et al. (2000, 2001)	Hurley, Pols, and Tout (2000)

Table 11. Sets of mass-loss prescriptions used in this paper, where the columns are evolutionary phases.

In this paper we update the prescriptions for wind mass loss of massive stars in the rapid binary population synthesis code COMPAS (Riley et al., 2022b) during several phases of stellar evolution, including on the main sequence (MS) for both massive and very massive stars (VMS), during the red supergiant (RSG) phase and during the Wolf–Rayet (WR) phase. VMS and RSG are new additions to the phase-based treatment of mass loss in COMPAS. In total, we add 15 new wind-mass-loss prescriptions. We find that uncertainties in mass-loss prescriptions have the largest impact on predictions for the formation rate of merging binary black holes, whilst the formation rates of merging binary neutron stars and neutron star-black hole binaries are more robust. We also discuss our results in the context of the missing red supergiant problem (Smartt et al., 2009), the maximum black hole mass at solar metallicity (Bavera et al., 2023; Belczynski et al., 2010; Miller-Jones et al., 2021; Neijssel et al., 2021; Romagnolo, Gormaz-Matamala, & Belczynski, 2024) and the formation of Gaia BH3 (El-Badry, 2024; Panuzzo et al., 2024).

The remainder of this paper is structured as follows: in Section 6.2 we introduce the population synthesis code COMPAS, and describe the mass-loss prescriptions we have implemented for various stages of massive stellar evolution. In Section 6.3, we illustrate the impact of these updated mass-loss prescriptions on predictions for the remnants of massive stars, including the maximum black hole mass and populations of double compact objects. We discuss our results and conclude in Section 6.4.

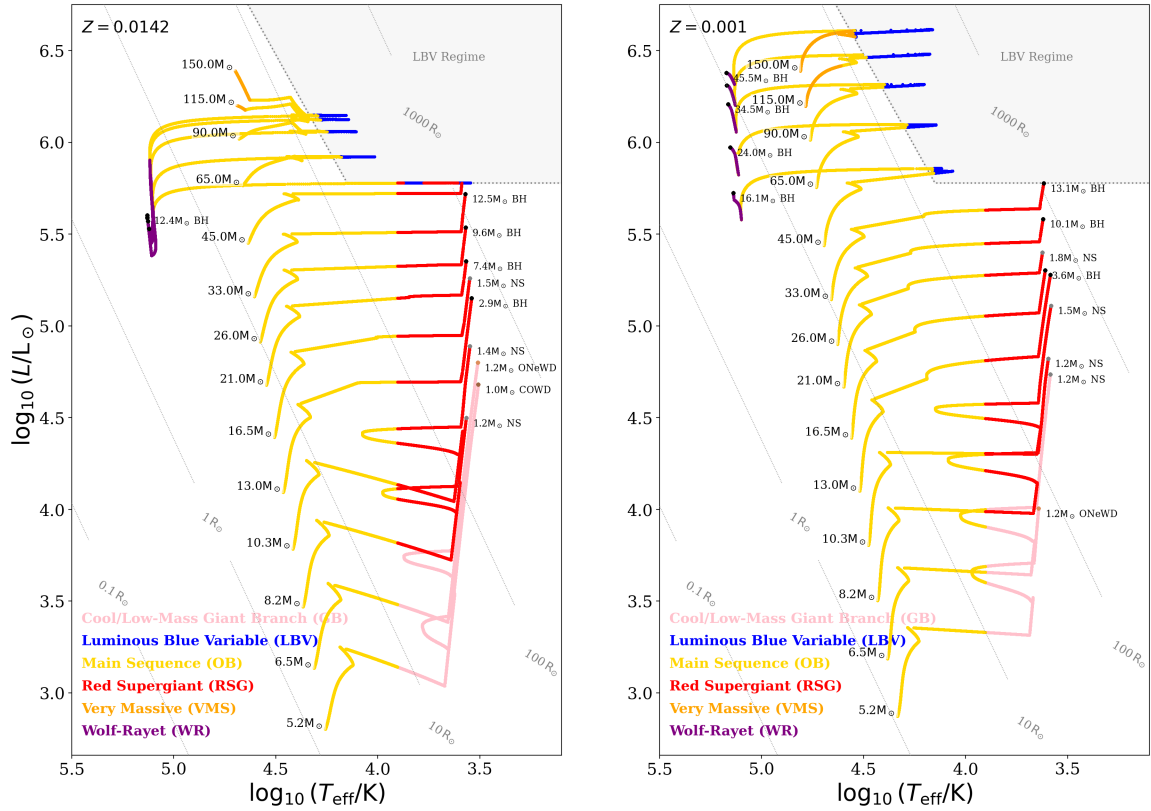


Figure 17. Hertzsprung–Russell diagram, with evolutionary tracks color-coded by the dominant mass-loss type (distinct from “stellar type” in COMPAS). These tracks are generated using the new Merritt 2024 combination of mass loss prescriptions. The left panel shows solar metallicity ($Z = 0.0142$) tracks and the right panel shows tracks at the lower metallicity $Z = 0.001$. ZAMS mass is annotated at the start of the track. The final compact object type and mass (assuming the Mandel and Müller (2020) stochastic remnant mass prescription) are also annotated at the track’s end. The shaded region in the upper right corner of this diagram labelled ‘LBV regime’ denotes stars that are beyond the Humphreys and Davidson (1979) limit and stars whose tracks enter this region are assumed to experience LBV-like mass loss.

6.2 Methods

We use the rapid binary population synthesis code COMPAS (Riley et al., 2022a, 2022b; Stevenson et al., 2017) to model the evolution of massive stellar binaries. Stellar tracks for single stars in COMPAS use the polynomial fitting formulae from Hurley et al. (2000) to the tracks from Pols, Schröder, Hurley, Tout, and Eggleton (1998). Binary stellar evolution is modeled following ?, with modifications as described in Riley et al. (2022b).

In this paper, we focus on mass-loss rates for massive stars, with M_{ZAMS} (zero-age main sequence) $> 10 M_{\odot}$, as these are the progenitors of neutron stars and black holes. These stars have significant mass loss across the Hertzsprung-Russell diagram (HRD).

The previous wind prescription used in COMPAS is detailed in Belczynski et al. (2010) and Riley et al. (2022b). In short, for massive OB main-sequence stars, mass-loss rates from Vink et al. (2000, 2001) were used. For cool stars ($T_{\text{eff}} < 12,500 \text{ K}$), mass-loss rates from Nieuwenhuijzen and de Jager (1990) were used for $L > 4000 L_{\odot}$. For lower-mass, cooler evolved stars, winds from Vassiliadis and Wood (1993) or Kudritzki and Reimers (1978) were used. For helium-rich Wolf-Rayet stars, mass-loss rates from Hamann and Koesterke (1998) were used, with a metallicity scaling from Vink and de Koter (2005), following Belczynski et al. (2010). Stars that exceed the Humphreys-Davidson limit (Humphreys & Davidson, 1979) are assumed to become luminous blue variables (LBVs) and experience eruptive mass loss, following a prescription from Belczynski et al. (2010). For low-mass stars, the prescription from Hurley et al. (2000) was used. We neglect the impact of rotation on mass loss.

In the following sections, we describe the updates we have made to modeling wind mass-loss during the main sequence (OB) (Section 6.2.1), for very massive stars (VMS) (Section 6.2.2), for red supergiants (RSG) (Section 6.2.3), and for helium-rich Wolf–Rayet (WR) stars (Section 6.2.4). Additionally, we compare three sets (New Defaults/MERRITT2024, PESSIMISTIC, Old Defaults/BELCZYNSKI2010) across the four on-phase mass-loss options (OB, RSG, VMS, WR) and explore the implications on compact binary formation and rates. Choices of prescription in these sets are detailed in table 11, and the regime of each wind phase is plotted in an HR diagram in Figure 17.

6.2.1 Winds of OB stars. For stars with $T_{\text{eff}} > 8000$ K and $M < 100 M_{\odot}$, we use a set of “OB mass-loss” prescriptions. Strictly speaking, these are applied in some cases outside of the main sequence and outside of the spectral types O, B, including to stars early on the Hertzsprung gap (HG); in fact, we apply these winds to all stars that satisfy the thresholds above unless they qualify as very massive stars (see Section 6.2.2), as red supergiants (see Section 6.2.3), or as naked helium stars (see Section 6.2.4). Winds are explicitly set to zero for remnants (WD, NS, BH).

Massive, main-sequence O and early B type stars experience strong line-driven winds (e.g., Castor, Abbott, & Klein, 1975; Pauldrach, Puls, & Kudritzki, 1986). Based on a series of Monte Carlo simulations, Vink et al. (2000, 2001) determined a recipe for the mass-loss rates of massive OB stars as a function of stellar parameters¹ including mass, effective temperature, luminosity and metallicity. The mass-loss rates increase for more luminous stars, meaning both that mass loss is expected to increase along the main sequence for a given star

¹We do not include an explicit scaling of the terminal wind velocity, v_{∞} , with metallicity when using the Vink et al. (2001) prescription.

and that initially more massive stars experience stronger winds. Due to its driving mechanism, mass loss is further predicted to increase with metallicity. A discontinuity in the mass-loss behavior predicted by Vink et al. (2000, 2001) occurs at a point in effective surface temperature referred to as the “bi-stability jump”, below which the mass loss is predicted to increase due to a recombination of iron (Vink, de Koter, & Lamers, 1999). While the precise behavior in this region is complex and still a matter of active research (e.g., Bernini-Peron et al., 2023; Krtićka, Kubát, & Krtićková, 2024; Petrov, Vink, & Gräfener, 2016), we assume – like most evolution codes – a simple transition between the two mass-loss regimes at $T_{\text{eff}} = 25,000$ K. Vink et al. (2001) further predict bi-stability jumps around 15,000 K, and 35,000 K but we do not implement these discontinuities explicitly. The Vink and Sander (2021) update to OB mass-loss provides two bi-stability jumps whose temperatures are gamma-dependent.

While the direct mass removal on the main sequence is usually low compared to the subsequent evolution stages, the amount of main-sequence mass loss can considerably influence which subsequent regimes are reached and how much time stars will spend in them (e.g., Higgins & Vink, 2020; Josiek, Ekström, & Sander, 2024; Langer & Maeder, 1995). In COMPAS, stars that lose mass during the main sequence transition to a stellar track of a non-mass-losing star of the reduced mass, at a time that preserves the fractional main-sequence lifetime. This simplified model, which does not track the composition and structure of the partially stripped star, can lead to errors in the stellar luminosity, which may affect subsequent mass evolution predictions (Shikauchi, Hirai, & Mandel, 2024).

Recently, several groups have determined the mass-loss rates for massive OB stars, finding that they are typically lower than those found by Vink et al. (2000,

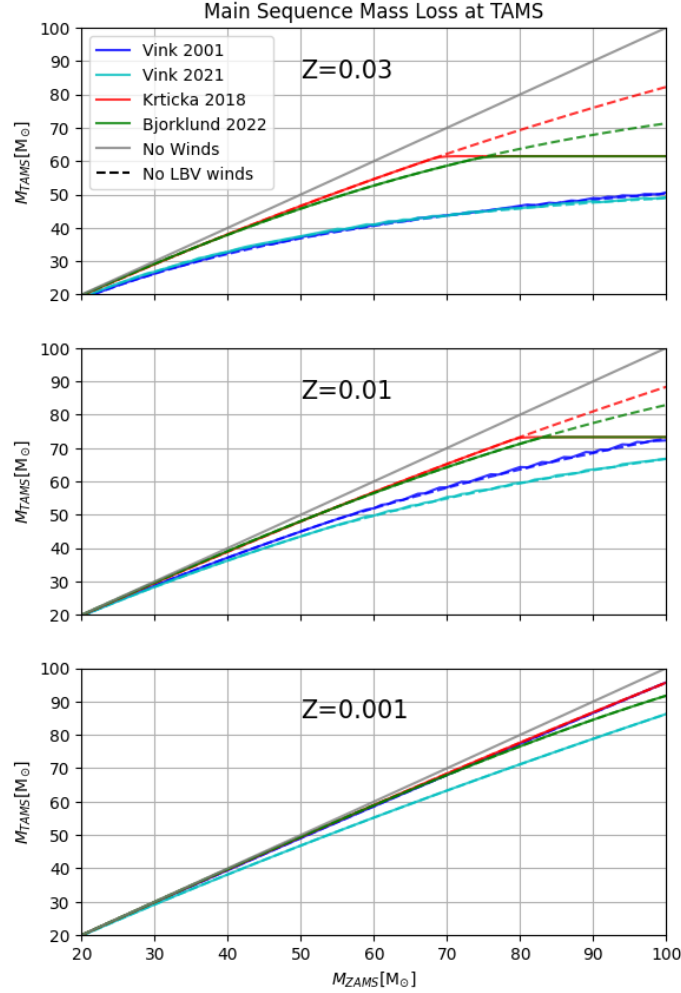


Figure 18. Terminal-age main-sequence (TAMS) mass M_{TAMS} as a function of the initial zero-age main-sequence (ZAMS) mass M_{ZAMS} . The three panels show the results for different metallicities: $Z=[0.03, 0.01, 0.001]$. The blue curve uses the Vink et al. (2001) prescription, the cyan curve uses the Vink and Sander (2021) prescription, the red curve uses the Krtićka and Kubát (2018) prescription and the green curve uses the Björklund et al. (2023). The previous default prescription is Vink et al. (2001). All prescriptions exhibit a strong metallicity dependence. The gray diagonal line indicates no main-sequence mass loss. Stars that exceed the Humphreys–Davidson limit may experience additional LBV mass loss already during core H burning, leading to a plateau at high mass; dashed lines have LBV winds turned off to demonstrate only the impact of main-sequence mass loss.

2001). Using non-thermodynamic equilibrium radiative transfer in the co-moving frame to connect the photosphere to the wind, Krtićka and Kubát (2017, 2018) calculate global, unified models of both the stellar atmosphere and the wind for O type dwarf, giant and supergiant stars at a range of metallicities. Their models predict lower mass-loss rates than Vink et al. (2000, 2001). This is in line with the general trend towards lower mass-loss rates due to the presence of wind clumping (e.g., Fullerton, Massa, & Prinja, 2006; Muijres et al., 2011; Vink, 2022), although the empirical picture remains complex (e.g., Brands et al., 2022; Ramachandran et al., 2019; Rickard et al., 2022) with post-interaction binaries and other evolved objects yielding higher mass-loss rates (e.g., Bouret et al., 2021; Pauli et al., 2023, 2022) and thus blurring any sample of main-sequence OB stars. Vink and Sander (2021) update the Monte Carlo wind simulations of Vink et al. (2000, 2001) and include a consistent calculation of the wind terminal velocity (following Müller & Vink, 2008), finding a shallower dependence of the mass-loss rate on metallicity than their previous models. Similar to Krtićka and Kubát (2017, 2018), Björklund et al. (2023) solve the spherically symmetric steady-state equation of motion using non-thermodynamic equilibrium radiative transfer in the co-moving frame for a grid of models. They provide a fit for the mass-loss rates of massive O and B-type stars as a function of stellar parameters, finding that their rates are significantly lower than those of Vink et al. (2000, 2001). We implement the updated mass-loss prescriptions derived by Krtićka and Kubát (2018), Vink and Sander (2021) (new default) and Björklund et al. (2023) in COMPAS.

For massive stars with initial, zero-age main-sequence (ZAMS) masses $10 < M_{\text{ZAMS}}/M_{\odot} < 100$ at three different metallicities ($Z = [0.001, 0.01, 0.03]$), we show the terminal-age main-sequence (TAMS) mass M_{TAMS} predicted by each

of these prescriptions in Figure 18. The Krtićka and Kubát (2018) and Björklund et al. (2023) prescriptions produce similar results, both giving less than half the main-sequence mass loss compared to Vink et al. (2001). We also find that at high metallicity ($Z \gtrsim 0.01$) the implementation of both the Krtićka and Kubát (2018) and Björklund et al. (2023) prescriptions in COMPAS results in a plateau in M_{TAMS} as a function of M_{ZAMS} (cf. Fig. 18). This plateau arises as stars that exceed the Humphreys–Davidson (HD) limit (Humphreys & Davidson, 1979) may experience additional LBV mass loss already during core H burning, leading to a plateau at high mass; dashed lines have LBV mass-loss turned off to demonstrate the impact of the implemented main-sequence wind prescriptions.

6.2.2 Very massive stars. Very massive stars (here with $M \geq 100 M_{\odot}$, following Vink et al., 2015) approach the Eddington limit while still core hydrogen burning. In COMPAS, we compute the Eddington parameter Γ_e as

$$\Gamma_e = 2.49 \times 10^{-5} \left(\frac{L}{L_{\odot}} \right) \left(\frac{M}{M_{\odot}} \right)^{-1}. \quad (6.1)$$

The mass loss rate increases rapidly as the Eddington parameter approaches unity (Bestenlehner et al., 2014; Vink et al., 2011). The origin of this behavior is a transition from optically thin to optically thick winds (Sabharwal et al., 2023; Vink & Gräfener, 2012), and corresponds to a spectral type transition from O, to Of(Evolved O-type with nitrogen and helium emission lines)/WNh(Wolf-Rayet of the nitrogen sequence with hydrogen), and eventually to WNh (Crowther & Walborn, 2011).

Vink et al. (2011) show the difference between their predictions and those of Vink et al. (2000, 2001), as a function of Γ_e in their Figure 5. We model the prediction of Vink et al. (2011) by adding a quadratic polynomial in Γ_e to the

logarithm² of the Vink et al. (2000, 2001) mass-loss rate for stars with $\Gamma_e > 0.5$:

$$\log \dot{M}_{V11} = \log \dot{M}_{V01} + F(\Gamma_e), \quad (6.2)$$

where $\log \dot{M}_{V01}$ is the mass-loss rate according to Vink et al. (2000, 2001) and

$$F(\Gamma_e) = a_0 + a_1\Gamma_e + a_2\Gamma_e^2 \quad (6.3)$$

with $a_0 = 0.0447$, $a_1 = 0.309$ and $a_2 = 0.243$. The accuracy of this fit can be quantified with an r^2 value of 0.983.

Sabhahit et al. (2023) recently presented a further improvement of this model involving a Γ_e -dependent switch point based on a set of MESA models, below which the low efficiency of winds dictates the use of the Vink et al. (2001) prescriptions, and above which the VMS Vink et al. (2011) prescription is used. The switch point occurs at a metallicity-dependent mass, luminosity, and escape velocity. They suggest implementing an iterative search algorithm to determine the switch point at each time step. However, for the speed desired in many population synthesis applications, we implement the prescription using simple fits to their switch mass and luminosity by fitting the data in their Table 2 as

$$\Gamma_{\text{SWITCH}} = 2.49 \times 10^{-5} \cdot \frac{L_{\text{SWITCH}}}{L_{\odot}} \cdot \frac{M_{\odot}}{M_{\text{SWITCH}}}, \quad (6.4)$$

where

$$L_{\text{SWITCH}}/L_{\odot} = 10^{2.36} Z^{-1.91}, \quad (6.5)$$

and

$$M_{\text{SWITCH}}/M_{\odot} = 0.0615 Z^{-1.574} + 18.10. \quad (6.6)$$

Finally, if $\Gamma_e > \Gamma_{\text{SWITCH}}$, we model the mass-loss rate as

$$\dot{M}_{\text{Sabhahit2023}} = \dot{M}_{\text{SWITCH}} \left(\frac{L}{L_{\text{SWITCH}}} \right)^{4.77} \left(\frac{M}{M_{\text{SWITCH}}} \right)^{-3.99}, \quad (6.7)$$

²All logs are base 10.

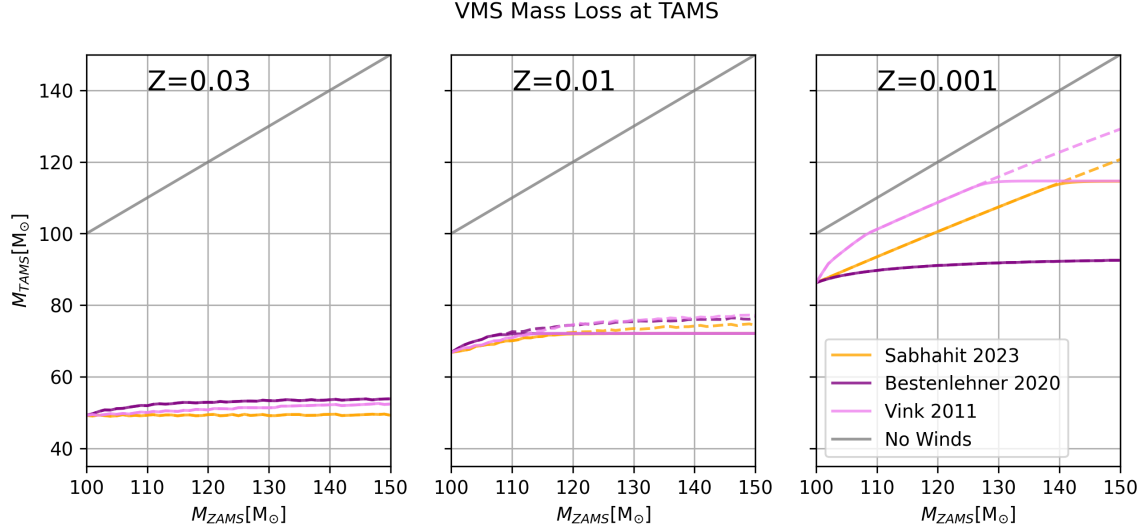


Figure 19. M_{TAMS} as a function of M_{ZAMS} for the three VMS mass-loss prescriptions described in Section 6.2.2. The three panels show the results for different metallicities: $Z = [0.03, 0.01, 0.001]$. The dotted lines show how VMS mass-loss treatment would proceed without the onset of LBV winds above the HD limit. The gray diagonal line shows $M_{\text{TAMS}} = M_{\text{ZAMS}}$, for no mass loss on the MS.

where

$$\log(\dot{M}_{\text{SWITCH}}/M_{\odot} \text{ yr}^{-1}) = -1.86 \log(Z) - 8.90; \quad (6.8)$$

otherwise, if $\Gamma_e \leq \Gamma_{\text{SWITCH}}$, $\dot{M}_{\text{Sabhahit2023}}$ follows the prescription for OB mass loss, for which Vink and Sander (2021) is the default model.

Finally, we also include the VMS mass-loss prescription from Bestenlehner (2020). This analytic prescription is a modified form of the original line driven theory from Castor et al. (1975) based on a study of the transition in Γ_e from optically thin to thick winds near $\Gamma_e \sim 0.5$.

In Figure 19 we show M_{TAMS} as a function of M_{ZAMS} in the regime where VMS winds occur for each prescription at three choices of metallicity ($Z = [0.03, 0.01, 0.001]$). At high (0.03) and near solar (0.01) metallicity, VMS with a broad range of initial masses yield similar $M_{\text{TAMS}} \sim 50 M_{\odot}$, and $M_{\text{TAMS}} \sim$

75 M_{\odot} , respectively, for all three VMS mass loss prescriptions, as all stars with $M_{\text{ZAMS}} \leq 150 M_{\odot}$ drop below the mass threshold for VMS winds for all three VMS prescriptions while still on the main sequence. The choices of VMS prescription diverge significantly in TAMS mass at low metallicity (0.001), however. Sabhahit et al. (2023) exhibits the greatest metallicity dependence, while Bestenlehner (2020) exhibits the least.

6.2.3 Red supergiant mass loss. Below $T_{\text{eff}} < 8000$ K, line-driven winds are no longer considered to be efficient and the mass loss mechanism changes. Stars with $8000 \text{ K} > T_{\text{eff}} > 3500 \text{ K}$ are considered “yellow” supergiants or hypergiants (de Jager, 1998), but the mass loss in this sparsely populated regime—also termed the “yellow void” (e.g., Nieuwenhuijzen & de Jager, 2000)—is highly uncertain with pulsations and outbursts possibly being more important than continuous winds for these stars (e.g., Humphreys, Jones, & Martin, 2023; Koumpia et al., 2020). Below $T_{\text{eff}} \sim 3500$ K, we reach the regime of red supergiants, which is much more populated and much better studied. The environment of the stars in this regime is usually cool enough to allow dust formation, which is thought to play a major role in explaining the winds of red supergiants – hence their common terminology as “dust driven” – though still with considerable uncertainties about the actual mechanisms and the strength of the outflows (see, e.g., Decin, 2021, for a recent review). Given the absence of dedicated recipes for the yellow supergiant domain, we follow the common strategy of many stellar evolution codes and treat the regime of evolved yellow and red massive stars with the same description, which for simplicity we call “red supergiants” (RSGs) for the rest of this work. We thus apply RSG winds to giant stars with a hydrogen-rich envelope with $T_{\text{eff}} < 8000$ K and ZAMS mass above 8 M_{\odot} (less massive cool stars experience NJ90 winds).

RSGs are observed as the progenitors of some hydrogen-rich type-IIP supernovae (Smartt, 2015; Smartt et al., 2009). The maximum observed RSG luminosity is around $\log(L/L_{\odot}) \approx 5.5$ (Davies & Beasor, 2020), and the maximum luminosity of a type-IIP RSG progenitor is fainter at $\log L/L_{\odot} \approx 5.1$, leading to the so called missing red supergiant problem (Smartt et al., 2009).³ There are several proposed explanations for this apparent discrepancy.

One proposal is that above some mass threshold (now estimated at $19_{-2}^{+4} M_{\odot}$), the missing RSGs experience a type of yet-unobserved failed supernova⁴ and directly collapse to form a black hole. This proposal has gained support from numerical simulations (O’Connor & Ott, 2011), and motivated searches for the disappearance of RSGs, with possible but inconclusive candidates found (Adams, Kochanek, Gerke, Stanek, & Dai, 2017b) (but see Beasor et al. 2024).

Another possible explanation of the missing RSG problem is that massive RSGs lose their hydrogen envelopes through mass loss, end their lives as stripped Wolf–Rayet stars, and produce hydrogen-poor (type I) supernovae (e.g., Georgy, 2012; Yoon & Cantiello, 2010). If a RSG undergoes core collapse and explodes with a hydrogen envelope, it will appear as a type-IIP supernova. If it loses its envelope through mass loss and becomes a Wolf–Rayet/helium star, it would go on to produce a H-poor supernova if it explodes. We find that these outcomes are very sensitive to the chosen mass-loss prescription during the RSG phase, and have major implications for the predicted ratios of different SN types and for the mass distributions of compact remnants.

³However, the significance of the missing RSGs is now estimated to be less than 2σ (Davies & Beasor, 2020), so there may not, in fact, be a missing population of luminous RSG type-IIP progenitors.

⁴Though see Neustadt et al. (2021) for potential candidates.

Typically, stellar evolution and population synthesis models have employed empirical prescriptions for RSG mass loss. The previous default in COMPAS (de Jager, Nieuwenhuijzen, & van der Hucht, 1988; Nieuwenhuijzen & de Jager, 1990) is a function of luminosity, mass, and radius based on a relatively small sample (271 stars) across the entire HR diagram, *of which only 14 were RSGs*. Recently, a number of updated RSG mass-loss prescriptions have become available. There was no “RSG” specific designation in mass-loss or stellar type, rather (de Jager et al., 1988; Nieuwenhuijzen & de Jager, 1990) was applied to stars with $T < 8000$ K and $L > 4000 L_{\odot}$. Our new switching criteria provide a set of RSG specific mass loss options, and applies to stars with $T < 8000$ K (thus including YSG and cooler RSG), $M_{\text{ZAMS}} > 8 M_{\odot}$, and belonging to one of the following evolved stellar types: Hertzsprung Gap (HG), Core Helium Burning (CHeB), First Giant Branch (FGB), Early Asymptotic Giant Branch (EAGB), Thermally Pulsing Asymptotic Giant Branch (TPAGB).

Beasor et al. (2020, 2023) derived an empirical RSG mass-loss prescription based on observations of RSGs in clusters, allowing them to fit the mass loss as a function of stellar mass M and luminosity L . This results in significantly lower mass-loss rates for RSGs compared to Nieuwenhuijzen and de Jager (1990), with even the most massive RSGs considered ($25 M_{\odot}$) by Beasor et al. (2020, 2023) retaining their hydrogen-rich envelopes (losing less than $1 M_{\odot}$ during the RSG phase) and avoiding self-stripping completely.

Kee et al. (2021) provide an analytical description of RSG mass loss by focusing on turbulence as the dominant mass-loss mechanism, and then further correct it numerically. This prescription is included in COMPAS for its unique approach, however, it proves very sensitive to the turbulent velocity parameter.

While this parameter is somewhat constrained from observation and from theory, within a reasonable range (15–21 km/s) the mass-loss rates vary by four orders of magnitude, limiting the predictive power of this prescription.

Decin et al. (2024) use ALMA data on CO line emission to determine the mass-loss rates of five red supergiants in the open cluster RSGC1. They find mass-loss rates systematically lower than those determined via SED fitting by a factor of ~ 2 (solid (CO) vs. dashed (SED) red lines in Figure 21). Decin et al. (2024) then use their ALMA data to recalibrate the mass-loss rates derived by Beasor et al. (2020) for RSGs in several clusters (solid green line in Figure 21). We take this as our default RSG mass-loss prescription in COMPAS. Decin et al. (2024) find that with this mass-loss prescription, RSGs do not lose their hydrogen envelopes due to wind mass loss.

Yang et al. (2023) study the mass-loss rates of a large sample of RSGs observed in the Small Magellanic Cloud (SMC). They obtain a third-order polynomial fit in L for the mass-loss rate, and find rates that are markedly higher than Beasor et al. (2020, 2023) or Decin et al. (2024), particularly for low luminosities ($L < 10^5 L_\odot$).

Vink and Sabhahit (2023) reinterpret the data from Yang et al. (2023), identifying a kink in the mass-loss rate at a luminosity of $\log(L/L_\odot) = 4.6$, and associating this with the onset of multiple scattering. They fit a functional form with both L and M dependence, similar to Beasor et al. (2020, 2023) and Decin et al. (2024). With this prescription, Vink and Sabhahit (2023) recover the Humphreys-Davidson limit (Humphreys & Davidson, 1979) at high luminosity, finding that high-mass RSGs lose their hydrogen envelopes, providing a solution to the missing red supergiant problem (Smartt et al., 2009).

We compare the impact of the weak RSG mass loss of Decin et al. (2024) to the strong RSG mass loss of Yang et al. (2023) in Figure 20. We show the fraction of hydrogen envelope mass remaining as a function of the dimensionless fractional time along the RSG phase $\tau_{\text{RSG}} = (t_{\text{RSG}} - t_{\text{RSG},i}) / (t_{\text{RSG},f} - t_{\text{RSG},i})$, where t_{RSG} is the age of the star on the RSG phase and subscripts i and f denote the start and end of the RSG phase. The Decin et al. (2024) prescription predicts that RSGs of masses $8\text{--}20 M_{\odot}$ retain a significant fraction of their hydrogen envelope. The much stronger mass-loss in the Yang et al. (2023) prescription leads RSGs with masses $\gtrsim 18 M_{\odot}$ to lose their envelopes and self strip, resulting in no massive RSG progenitors to type IIp supernovae.

We have implemented the Beasor et al. (2020, 2023), Decin et al. (2024), Yang et al. (2023) and Vink and Sabhahit (2023) RSG mass-loss prescriptions into COMPAS. Figure 21 shows a comparison of the mass-loss rates for RSGs predicted by each of these prescriptions. We choose the Decin et al. (2024) prescription as our new default mass-loss rate.

While the red supergiant populations are not necessarily the same at different metallicities (e.g., Bonanos et al., 2023; de Wit et al., 2024; Ou, Chen, Chu, & Tsai, 2023), the presumed mechanisms based on pulsation and dust as well as observational constraints suggest that the individual mass-loss rates may be largely insensitive to metallicity (e.g., Antoniadis et al., 2024; Goldman et al., 2017, though see Maunon and Josselin 2011). Moreover, the maximum RSG luminosity appears to be independent of metallicity (at least for $Z > 0.25 Z_{\odot}$; McDonald, Davies, & Beasor, 2022) suggesting that the mechanism leading to the Humphreys-Davidson limit (Humphreys & Davidson, 1979) is not strongly

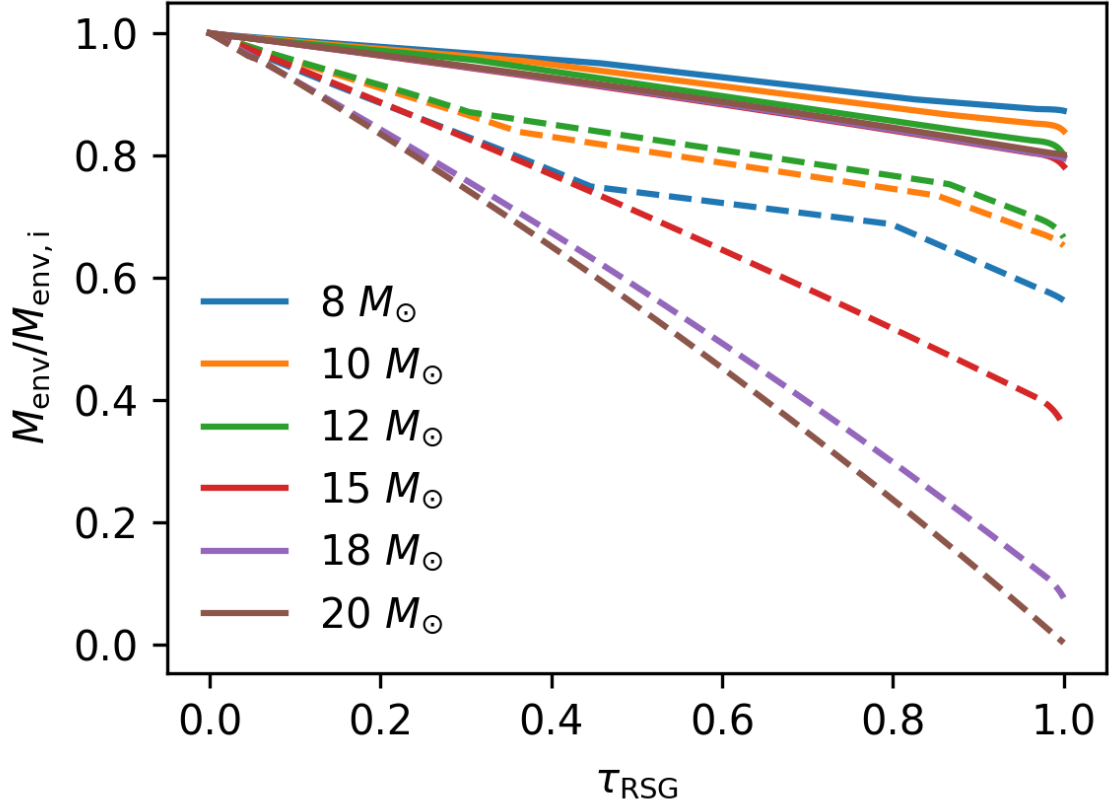


Figure 20. Fraction of envelope mass remaining for massive stars during the RSG phase. The abscissa is the fractional time along the RSG phase, whilst the ordinate is normalized to the envelope mass at the start of the RSG phase. The solid lines use our standard RSG prescription (Decin et al., 2024), whilst the dashed curves use the prescription from Yang et al. (2023). The colors denote the initial (ZAMS) mass of the stars in solar masses, as labeled in the legend. Solar metallicity is assumed.

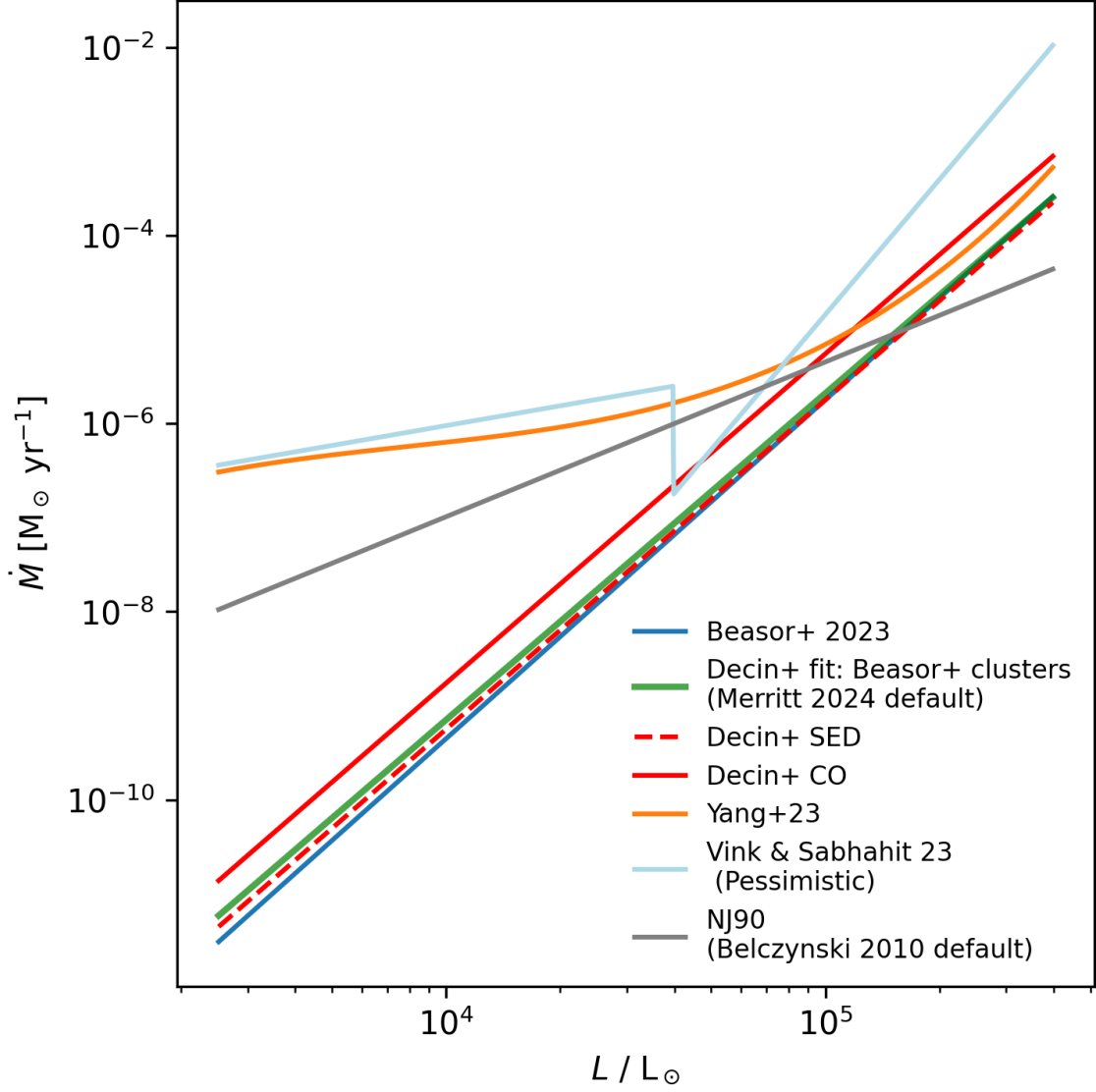


Figure 21. Mass-loss rate as a function of luminosity for RSGs according to the various prescriptions discussed in this paper. For prescriptions that are dependent on mass, we assume a mass of $15 M_{\odot}$ for visualization purposes. For NJ90, solar metallicity and a surface temperature of 4000 K is assumed. Kee et al. (2021) is not included, because rates vary over four orders of magnitude given reasonable choices of the turbulent velocity. None of the implemented prescriptions have direct metallicity dependence. [Incorrect for NJ90, which should be defined on first use.]

metallicity dependent. By default, we do not scale RSG mass-loss rates with metallicity.

Analyzing a large sample of RSGs in M31 and M33, Wang, Jiang, Ren, Yang, and Li (2021) find there can be an order-of-magnitude difference in the mass-loss rates between RSGs with carbon-rich dust (which typically have lower mass-loss rates) and those with oxygen/silicate rich dust. The inferred mass-loss rate from spectral energy distribution fitting also depends on the assumed gas-to-dust ratio (Wang et al., 2021). We have not implemented their prescription here, but aim to implement it in a future version of COMPAS.

Ultimately, we find that there are orders-of-magnitude variations between the different RSG mass-loss prescriptions, such that the mass loss of massive RSGs remains highly uncertain.

6.2.4 Wolf–Rayet stars. Classical Wolf–Rayet (WR) stars are massive, evolved, helium-rich stars, which lose mass at high rates through optically thick winds. Formally defined by their spectral appearance, we use the term WR in the sense of classical, i.e. He-burning, WRs here as other stars with WR-type spectra (e.g., VMS) are subject to a different wind treatment in COMPAS. (Classical) WR stars can arise either from high-mass single stars through wind stripping, from binary stars stripped through binary interactions, or a combination of both (Abbott & Conti, 1987; Crowther, 2007; Shenar, Gilkis, Vink, Sana, & Sander, 2020; Vanbeveren, De Loore, & Van Rensbergen, 1998). We apply WR winds to stars that are fusing helium in their cores on the helium main sequence (HeMS), as well as stars on the helium Hertzsprung gap (HeHG) and helium giant branch (HeGB).

Similar to RSGs, WR mass-loss prescriptions are typically empirical. Due to their optically thick winds, the mass of WR stars is not directly accessible from their spectra, meaning that resulting empirical recipes mainly scale with the luminosity of the stars (e.g., Hamann, Gräfener, & Liermann, 2006; Nugis & Lamers, 2000; A. Sander, Todt, Hainich, & Hamann, 2014; Shenar et al., 2019; Tramper, Sana, & de Koter, 2016). In our previous model for WR winds in COMPAS, we followed the prescription from Belczynski et al. (2010), which reduces the mass-loss rates from Hamann et al. (1995) by a factor of 10 (motivated by Yoon, Langer, & Norman, 2006), and applies a scaling of the mass-loss rate with initial metallicity proportional to $Z^{0.86}$, from Vink and de Koter (2005).

Recently, A. A. C. Sander and Vink (2020) presented the first thorough calculations of WR mass-loss rates using dynamically-consistent stellar atmosphere models (A. A. C. Sander, Hamann, Todt, Hainich, & Shenar, 2017). The atmosphere models of A. A. C. Sander and Vink (2020) made use of a single fixed effective temperature. Subsequently, A. A. C. Sander et al. (2023) derived a temperature correction to the mass-loss rates presented in A. A. C. Sander and Vink (2020) accounting for a realistic range of WR effective temperatures. We account for the temperature correction as

$$\log \left(\frac{\dot{M}_{\text{SV2023}}}{M_{\odot} \text{ yr}^{-1}} \right) = \log \left(\frac{\dot{M}_{\text{SV2020}}}{M_{\odot} \text{ yr}^{-1}} \right) - 6 \log \left(\frac{T_{\text{eff}}}{\text{K}} \right), \quad (6.9)$$

for $T_{\text{eff}} > T_{\text{min}}$. We assume a minimum temperature $T_{\text{min}} = 1 \times 10^5 \text{ K}$ (A. A. C. Sander et al., 2023). For $T_{\text{eff}} \leq T_{\text{min}}$, the unmodified \dot{M}_{SV2020} is used.

The mass-loss rates given by A. A. C. Sander et al. (2023); A. A. C. Sander and Vink (2020) are applicable to massive, high-luminosity WR stars, and predict no mass-loss below a cutoff luminosity. For lower-mass (and thus lower-luminosity)

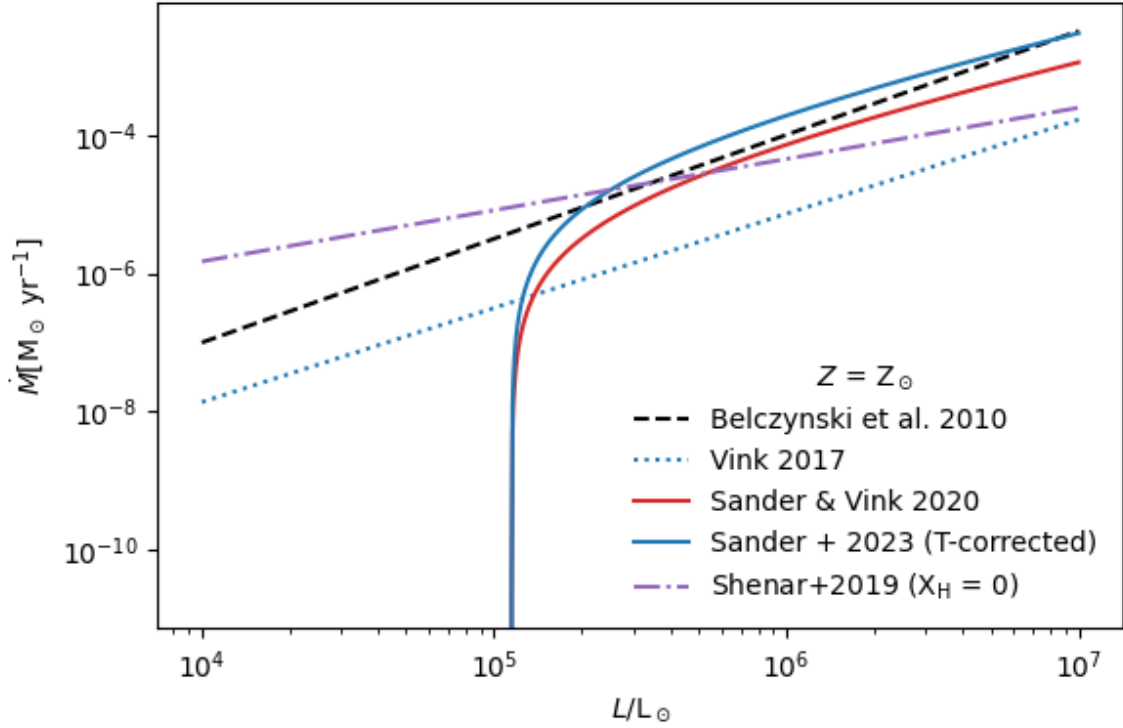


Figure 22. Mass-loss rates of WR stars as a function of luminosity at solar metallicity. The dashed black line shows the previous prescription in COMPAS (Belczynski et al., 2010; Hamann et al., 1995; Vink & de Koter, 2005). The dotted blue curve shows the mass-loss prescription from Vink (2017). The solid red curve shows the mass-loss prescription for massive WR stars from A. A. C. Sander and Vink (2020), without applying the temperature correction from A. A. C. Sander et al. (2023). As discussed in Section 6.2.4, in COMPAS we use the maximum of the Vink (2017) prescription and the A. A. C. Sander and Vink (2020) prescription with the temperature correction applied (cf. Equation 6.11). The blue curve shows the correction applied at an effective temperature of 120,000 K. The dashed purple curve shows the Shenar et al. (2019) mass-loss prescription.

helium stars, we opt to instead use the mass-loss rates from Vink (2017)

$$\dot{M}_{\text{Vink2017}} = -13.3 + 1.36 \log(L/L_{\odot}) + 0.61 \log(Z/Z_{\odot}). \quad (6.10)$$

following Woosley, Sukhbold, and Janka (2020). Recently, Ramachandran et al. (2024) have shown that this prescription provides an adequate estimate of the mass-loss rates of low-mass stripped stars. The final mass-loss rate for helium stars is then determined as

$$\dot{M}_{\text{WR}} = \max(\dot{M}_{\text{Vink2017}}, \dot{M}_{\text{SV2023}}) \quad (6.11)$$

Finally, as an alternative, we also implement the empirical WR mass-loss rate prescription from Shenar et al. (2019), based on a combined sample of analyzed WN stars from the Milky Way (Hamann et al., 2019), M31 (A. Sander et al., 2014), the SMC (Hainich et al., 2014; Shenar et al., 2016), and the LMC (Hainich et al., 2015; Shenar et al., 2019).

In COMPAS, we include the option to multiply WR mass-loss rates by an arbitrary factor f_{WR} (cf. Barrett et al., 2018). By default, we assume $f_{\text{WR}} = 1$ for all plots in this paper. We compare the mass-loss prescriptions from Belczynski et al. (2010), Vink (2017), Shenar et al. (2019) and A. A. C. Sander and Vink (2020) in Figure 22.

6.3 Population synthesis results

In this section we use the binary population synthesis code COMPAS to examine the impact of the updated mass-loss prescriptions for massive stars described in the previous section.

6.3.1 Maximum black hole mass. We begin by investigating the impact of our updated mass-loss prescriptions on the maximum black hole mass that can be formed by a single star. We evolve grids of single stars in the mass

range $5\text{--}150 M_{\odot}$ and in the metallicity range $0.0001 \leq Z \leq 0.03$ (Hurley et al., 2000). Unless otherwise stated, we use the default COMPAS settings, and only vary the mass-loss prescriptions. We calculate remnant masses and kicks using the remnant prescription from Mandel and Müller (2020).

We present results for three different sets of mass-loss prescriptions. These are the previous defaults BELCZYNSKI2010, our new defaults (MERRITT2024), and a choice with higher mass loss in most evolutionary phases (PESSIMISTIC). The choices of mass-loss prescription for each evolutionary phase (OB, VMS, RSG, WR) are given in Table 11.

In Figure 23 we show the initial-final mass relation at $Z = [0.03, 0.01, 0.001, 0.0001]$. The ‘saw-tooth’ feature at lower masses is due to stars experiencing SNe during core helium burning with an intact envelope, although PESSIMISTIC stars with increased RSG winds lose most of their hydrogen envelope even for relatively low ZAMS masses. With our updated RSG mass-loss rates (MERRITT2024, using the Decin et al., 2024 prescription for RSGs), stars with $10 M_{\odot} < M_{\text{ZAMS}} \lesssim 35 M_{\odot}$ do not lose their entire hydrogen envelopes. If a significant fraction of the hydrogen envelope can fall back, this may result in a relatively high mass BH. Beyond this, the drop at ZAMS masses of $\sim 40 M_{\odot}$ is due to envelope ejection/self-stripping, which occurs at an abrupt Z -dependent threshold in M_{ZAMS} driven primarily by RSG winds. Note that this feature is present with the MERRITT2024 winds and to a lesser extent with BELCZYNSKI2010, but not with the PESSIMISTIC winds (essentially all BH progenitors self-strip). The plateaus around $100 M_{\odot}$ are due in part to the onset of LBV winds at the HD limit, and to VMS winds above $100 M_{\odot}$.

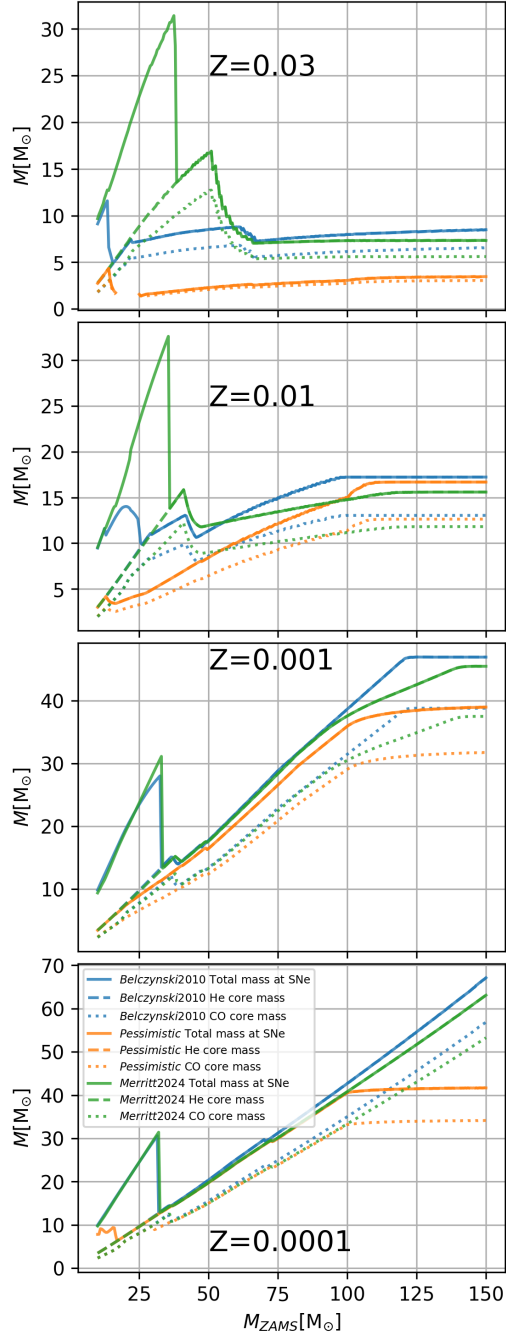


Figure 23. Initial-final total and core mass relation for single massive stars. The top panel shows the relation for $Z = 0.03$ and the bottom panel for $Z = 0.0001$, the highest and lowest metallicities modeled in COMPAS, respectively.

We show the maximum black hole mass formed as a function of metallicity in Figure 24. At low metallicity ($Z \lesssim 10^{-3}$), the maximum black hole mass is determined by the onset of the electron-positron pair-instability (Fowler & Hoyle, 1964; Rakavy & Shaviv, 1967), leading to a mass gap above a black hole mass of around $45 M_{\odot}$. For stars experiencing pulsational pair-instability supernovae (PPISN Belczynski, Heger, et al., 2016; Farmer, Renzo, de Mink, Marchant, & Justham, 2019; Hendriks et al., 2023; Marchant et al., 2019; Renzo & Smith, 2024; Stevenson et al., 2019; Woosley, 2017), we employ the Hendriks et al. (2023) prescription, based on the detailed stellar models from Farmer et al. (2019), (see also Renzo, Hendriks, van Son, & Farmer, 2022). This model employs a flexible parameter for the onset of PPISN, where the default is above a carbon-oxygen core mass of $34.8 M_{\odot}$.

At higher metallicity ($Z \gtrsim 10^{-2}$), some of the most massive black holes form via RSG progenitors that avoid losing their hydrogen envelopes through stellar winds. The maximum black hole mass in this metallicity range is $\sim 32 M_{\odot}$, using the Fryer et al. (2012) remnant mass prescription (which allows stars to retain their hydrogen envelopes upon collapse), and $\sim 18 M_{\odot}$, using the Mandel and Müller (2020) remnant mass prescription, which assumes that the hydrogen envelope is expelled via the Nadezhin (1980) mechanism (Fernández, Quataert, Kashiyama, & Coughlin, 2018; Lovegrove & Woosley, 2013). Several authors have argued that it may be possible to form more massive black holes if the hydrogen envelope is retained and falls back onto the black hole (e.g., Costa et al., 2021; Farrell et al., 2021; Vink, Higgins, Sander, & Sabhahit, 2021). On the other hand, the hydrogen envelope is expected to be stripped by mass transfer prior to BH formation in

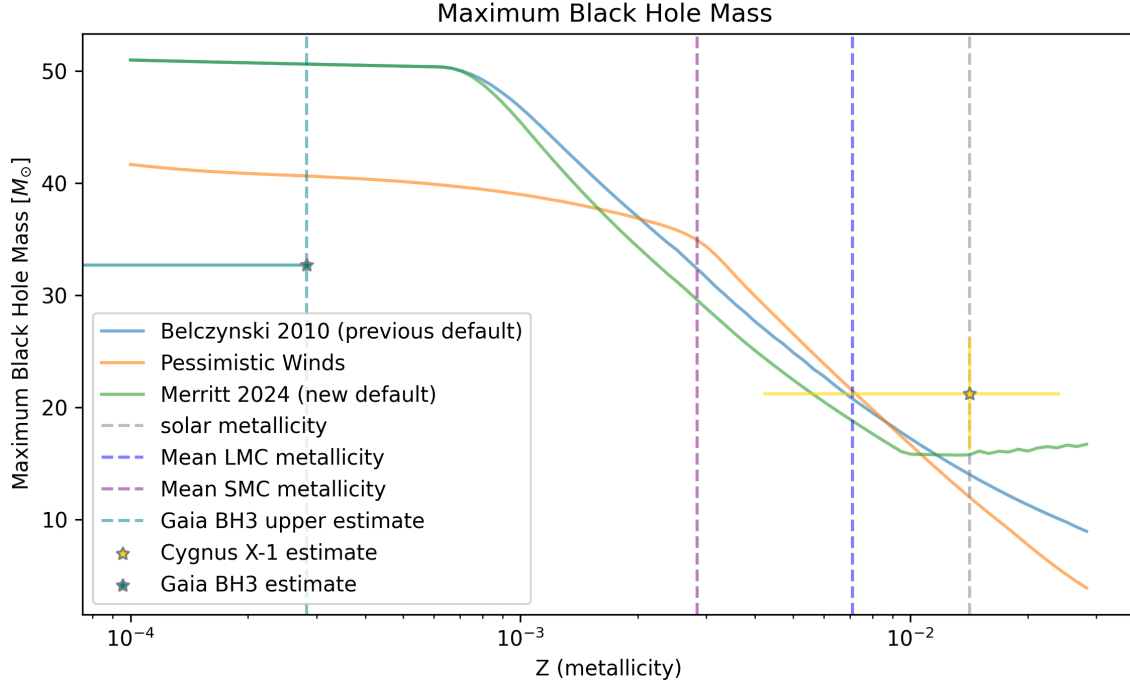


Figure 24. Maximum black hole mass formed from a single star as a function of metallicity. The blue line shows the result using the previous wind prescription in COMPAS (Belczynski et al., 2010). The green line shows the updated result using the new default combinations of wind prescriptions implemented in this work. The orange line shows a pessimistic choice of mass-loss prescriptions that lead to increased mass loss and typically lower black hole masses. All models use the Mandel and Müller (2020) remnant mass prescription. The maximum black hole mass at low metallicity ($Z \lesssim 10^{-3}$) for the **BELCZYNSKI2010** and **Merritt2024** models is set by pair instability supernovae, implemented according to Hendriks et al. (2023). The yellow cross and star show the mass and metallicity estimate for the black hole in Cyg X-1 (Miller-Jones et al., 2021), while the leftward teal line shows the mass and metallicity for Gaia BH3 (Panuzzo et al., 2024). LMC and SMC metallicity are assumed to be 0.5 and 0.2 of solar, respectively, Vink et al. (e.g. 2023).

compact binaries, such as those leading to the formation of merging BHs and X-ray binary systems.

6.3.2 Forming the most massive Galactic stellar mass BHs:

Cyg X-1 and Gaia BH3. Until recently, the most massive stellar-mass black hole known in the Milky Way was the high-mass X-ray binary Cygnus X-1, with a mass of $21 \pm 2 M_{\odot}$

Higgins, Sander, Vink, and Hirschi (2021) evolve detailed models of helium stars using WR mass-loss rates from A. A. C. Sander and Vink (2020). They find that a helium star with $M_{\text{He},i} \gtrsim 40 M_{\odot}$ can produce a helium star with a final mass of $M_{\text{He},f} \sim 20 M_{\odot}$, capable of producing a black hole as massive as Cyg X-1. However, they do not address the question of forming such a massive helium star at solar metallicity.

One potential pathway for forming high helium core masses at solar metallicity is to form Cyg X-1 through chemically homogeneous evolution (CHE; de Mink et al., 2009; Qin, Marchant, Fragos, Meynet, & Kalogera, 2019). In this scenario, rapid rotation due to tidal locking induces efficient mixing within the primary star, allowing it to fuse nearly all of its hydrogen into helium, thus producing a more massive helium star than classical evolution would allow.

Perhaps the most obvious resolution of the tension between the predicted and observed black hole masses may be due to shortcomings of stellar and binary evolution models in COMPAS. In particular, the use of Hurley et al. (2002) models for the evolution of mass-losing main-sequence stars leads to an artificial decrease in the final core mass (see discussion in Romero-Shaw, Hirai, Bahramian, Willcox, and Mandel 2023). Mass loss during the main sequence affects both the radial evolution of the mass-losing main sequence star, allowing it to remain compact and

blue (Bavera et al., 2023) and thus impacting subsequent mass transfer, and the evolution of the convective core, allowing more massive helium-rich cores to form than in COMPAS models (Shikauchi et al., 2024). The implications of allowing mass-losing stars to retain a greater fraction of their core mass (Shikauchi et al., 2024) for the formation of Cygnus X-1 will be discussed in detail elsewhere (Breck et al., in prep.).

Assumptions about convective mixing and overshooting also impact predictions for the final core masses of stars. COMPAS uses the stellar models from Pols et al. (1998). Examining five sets of commonly used stellar models at solar metallicity, Agrawal, Szécsi, Stevenson, Eldridge, and Hurley (2022) show that the maximum core mass that can be formed at solar metallicity varies in the range 20–40 M_{\odot} under different model assumptions. Other studies (e.g., Martinet, Meynet, Ekström, Georgy, & Hirschi, 2023; Vink, Sabhahit, & Higgins, 2024; Zapartas et al., 2021) also find a broad range of maximum black hole masses. Bavera et al. (2023) found in their detailed binary simulations that not only can black holes up to 30 M_{\odot} form at solar metallicity, they can be members of merging binary black holes.

Romagnolo et al. (2024) recently implemented a series of updated mass-loss prescriptions for massive stars in a *detailed* stellar evolution code to examine the maximum black hole mass that can be formed at solar metallicity from a slowly rotating, single star. They use the mass-loss prescription from Bestenlehner (2020) for VMS. For their choice of mass-loss prescriptions and input physics, they are unable to produce black holes with masses $\gtrsim 30 M_{\odot}$, unlike the results of Bavera et al. (2023) and Martinet et al. (2023).

The recent discovery of Gaia BH3 (Panuzzo et al., 2024), a $33 M_{\odot}$ black hole in a 11.6 yr orbit with a low-mass companion star, has revealed the existence of a population of even more massive stellar mass black holes in the Milky Way. Gaia BH3 may have formed through isolated binary evolution from an initially wide, eccentric binary (El-Badry, 2024; Iorio et al., 2024). Alternatively, Gaia BH3 may have formed dynamically in a star cluster (Marín Pina et al., 2024), as hinted at by the association with the disrupted stream ED-2 (Balbinot et al., 2024; Panuzzo et al., 2024). Whilst the birth metallicity of Gaia BH3, at $[\text{Fe}/\text{H}] \sim -2.5$ (Balbinot et al., 2024), which would correspond to $Z < 10^{-4}$, is outside of the range that can be modeled using COMPAS (Hurley et al., 2000; Pols et al., 1998; Riley et al., 2022b), this BH likely did not form from the current Population I stars. We see from Figure 24 that with our updated mass-loss prescriptions, black holes with masses $\gtrsim 30 M_{\odot}$ can form at metallicities $Z \lesssim 3 \times 10^{-3}$, consistent with the identification of the companion star as a very metal poor star (Panuzzo et al., 2024).

6.3.3 Impact on double compact objects. A large sample of double compact object (DCO) mergers have now been observed in gravitational waves (Abbott et al., 2023), including binary neutron star (BNS; Abbott et al., 2017), neutron star-black hole (NSBH; Abbott et al., 2021) and binary black hole (BBH; Abbott et al., 2016a) mergers. DCOs may form via the evolution of massive stellar binaries (e.g., Mandel & Farmer, 2022; Mapelli, 2021; Tutukov & Yungelson, 1973; van den Heuvel & De Loore, 1973).

In this section, we perform population synthesis using COMPAS to examine the impact of our updated mass-loss prescriptions on the formation of merging DCOs. Unlike Riley et al. (2021a), we assume that binaries experiencing Roche lobe overflow at birth lead to stellar mergers, because including these leads to an

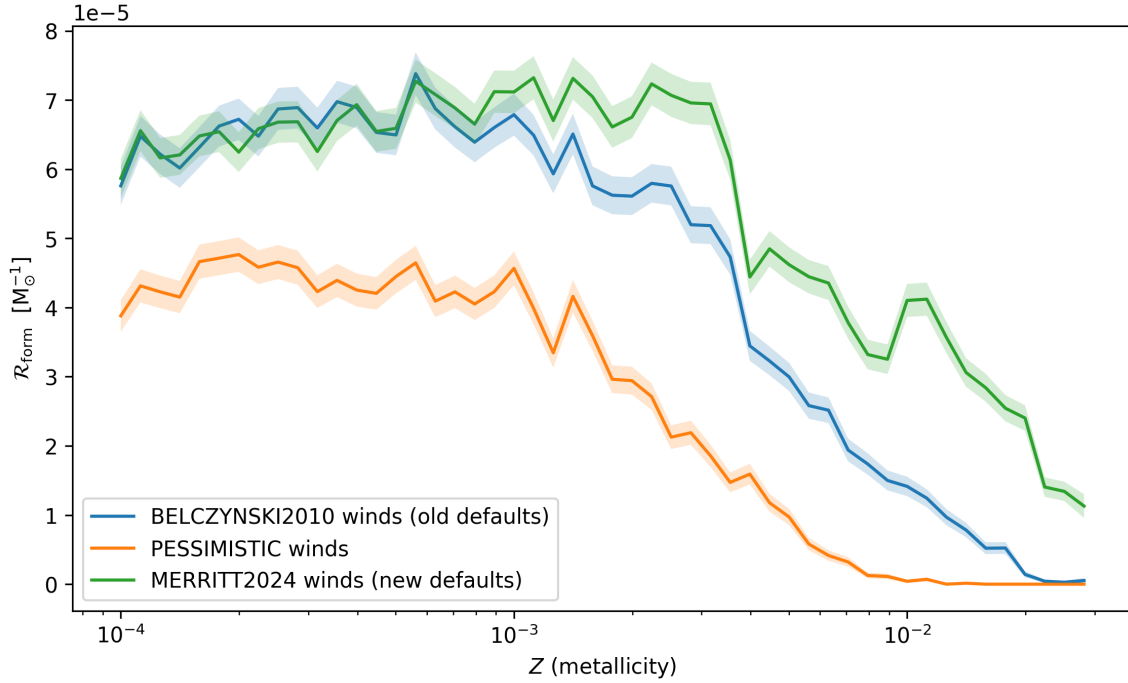


Figure 25. Formation rates of merging BBHs per star forming mass as a function of metallicity. The different colored lines denote our different sets of mass-loss prescriptions (see Table 11). The shaded region around each line indicates the sampling uncertainty, as estimated through bootstrapping. The blue line shows the previous default model (BELCZYNSKI2010: Belczynski et al., 2010; Riley et al., 2022b), the orange line shows the PESSIMISTIC model and the green line shows our new default model (MERRITT2024).

overproduction of BBHs through CHE inconsistent with observation (Stevenson & Clarke, 2022). We assume the Mandel and Müller (2020) remnant mass prescription and kick distribution. We calculate the yields of DCOs that merge within the age of the universe formed at a given metallicity per unit of star formation. In Figure 25 we show the yield of merging BBHs as a function of metallicity for each of our sets of mass-loss prescriptions.

Yields of double compact objects are highly sensitive to the treatment of mass loss (e.g., Broekgaarden et al., 2022; Wagg et al., 2022). We find that the treatments of RSG and WR winds are most consequential, especially on the formation of BBHs. WR winds have a dominant effect on the production of high metallicity systems, because high-mass stars are almost universally stripped above solar metallicity.

At low metallicity we find that RSG winds have a dominant effect on yields. The PESSIMISTIC (Vink & Sabhahit, 2023) RSG wind prescription leads to a reduction in merging BBH yields by a factor of ~ 2 . At these metallicities and below a ZAMS mass of $40 M_{\odot}$ (frequently the secondary for BBH formation), whether the star self-strips depends on the choice of prescription, as mass-loss rates vary over 3-5 orders of magnitude. By this time the core mass is sufficient for black hole formation in any case, but the ejection of the envelope often leads to orbital widening that prevents the system from merging in a Hubble time.

Compared to BBHs, the yields of BNSs and NSBHs, which generally come from less massive progenitors with lower wind mass loss, are more robust to changes in the mass-loss prescription, being consistent with sampling uncertainties at most metallicities. Our findings match those of van Son et al. (2024).

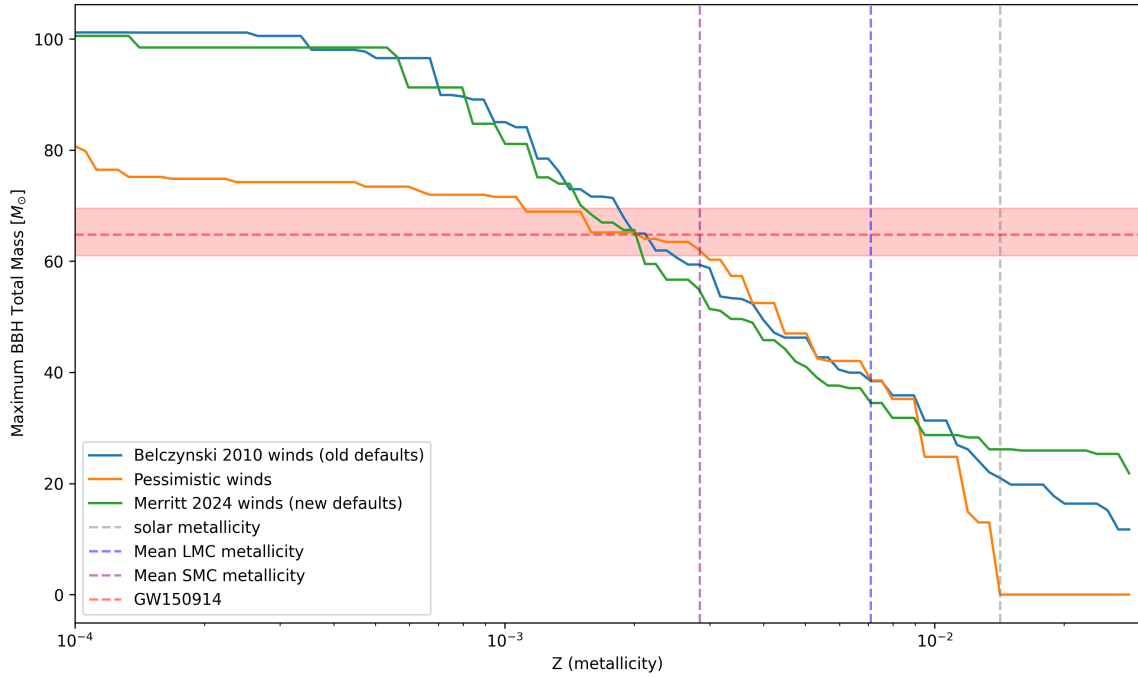


Figure 26. Maximum total mass of merging BBHs as a function of metallicity, as distinct from final mass which would account for energy lost in GWs. The vertical dashed lines denote solar metallicity, and that of the Large and Small Magellanic Clouds. The horizontal dashed red line denotes the total mass of GW150914, with the median sample, and 90% credible intervals filled (Abbott et al., 2016a), illustrating that such high-mass BBHs are expected to form only in low-metallicity environments in these models.

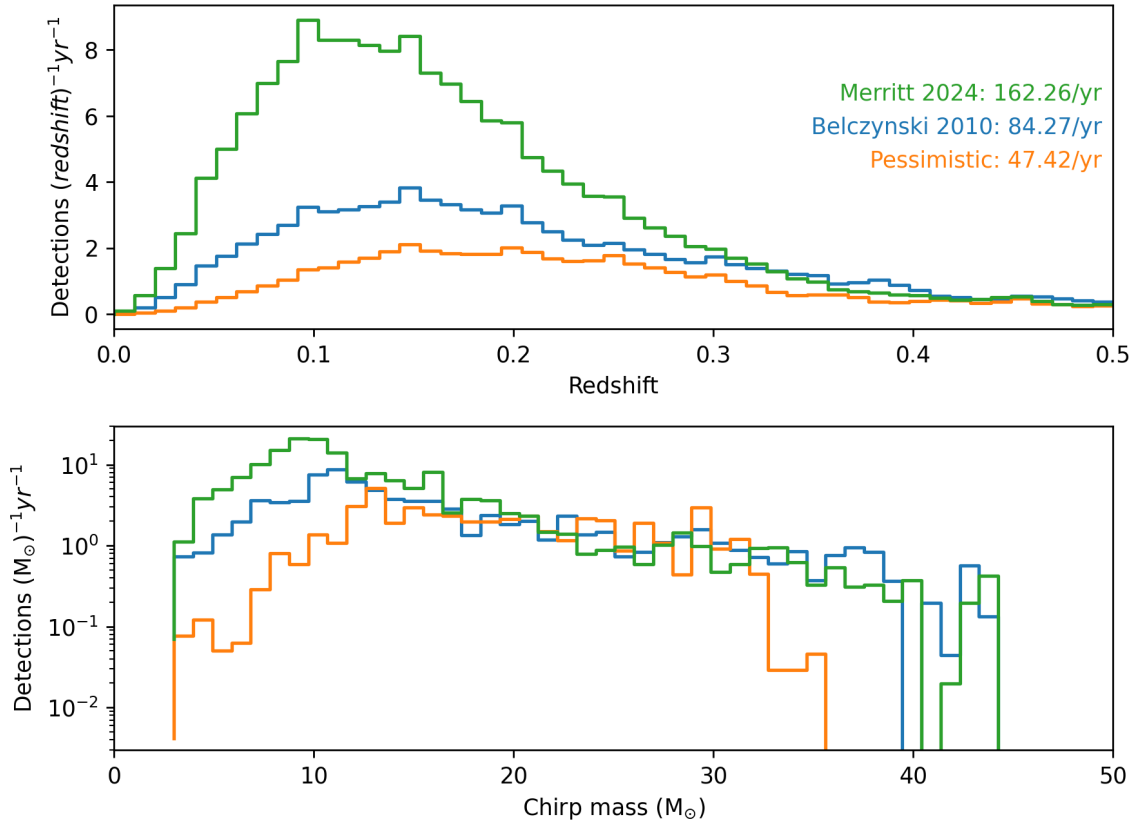


Figure 27. Projected detections of BBH binned by chirp mass and redshift, assuming sensitivity of the third observing run (O3) of LVK, with a detection threshold SNR of 8. Updating winds creates an excess near a chirp mass of 10 M_{\odot} , and lowers the density at 25–45 M_{\odot} . Blue=BELCZYNSKI2010, Orange=PESSIMISTIC, Green=MERRITT2024.

In Figure 26 we show the maximum total mass of merging BBHs formed as a function of metallicity (see also Belczynski, Holz, Bulik, & O’Shaughnessy, 2016). Similar to the single star case (Figure 24), we find a large difference at low-metallicity ($Z = 10^{-4}$) when using the PESSIMISTIC model, with a maximum total mass of merging BBHs of around $75 M_{\odot}$ compared to $90 M_{\odot}$ in BELCZYNSKI2010 and MERRITT2024. This means that massive merging BBHs such as GW150914 would need to be formed at $Z \lesssim 10^{-3}$ with the MERRITT2024 and BELCZYNSKI2010 prescriptions or at even lower metallicities with the PESSIMISTIC winds prescription (Abbott et al., 2016; Belczynski, Holz, et al., 2016). At solar metallicity ($Z = 0.0142$), we find that our new MERRITT2024 model can produce merging BBHs with total mass up to $35 M_{\odot}$, compared to $25 M_{\odot}$ in BELCZYNSKI2010 and PESSIMISTIC. At intermediate metallicities typical for the SMC and LMC, the three models predict similar maximum total BBH masses.

In Figure 27 we show predictions for the observed chirp mass and redshift distributions of merging BBHs. We perform cosmic integration using the built in tools in COMPAS (Barrett et al., 2018; Neijssel et al., 2019; Riley et al., 2022b). We assume a gravitational-wave network with the approximate sensitivity of LIGO during the O3 run. In the new MERRITT2024 model, the chirp mass distribution has an increased pileup in the $10 M_{\odot}$ peak and a decrease at higher masses. We also find that the total predicted BBH detection rate increases by a factor of ~ 2 in the MERRITT2024 model compared to the BELCZYNSKI2010 model. The PESSIMISTIC model decreases the BBH detection rate by a factor of ~ 2 compared to the BELCZYNSKI2010 model. For BNS and NSBH mergers, the chirp mass distribution remains approximately the same, within sampling error, among the tested wind variations.

6.4 Discussion and conclusions

Massive stars can lose a significant fraction of their mass through stellar winds in various evolutionary phases, impacting the masses of the compact objects they leave behind. Mass-loss prescriptions are hence an important ingredient in any stellar evolution or population synthesis code. There has been significant progress recently in both theoretical predictions and empirical measurements of the mass-loss rates for massive stars. Making use of this progress, and taking advantage of the ability of rapid population synthesis tools to explore a broad range of scenarios, we have updated the mass-loss rate prescriptions for several phases of massive stellar evolution (MS, VMS, RSG and WR) in the rapid binary population synthesis code COMPAS (Riley et al., 2022b; Stevenson et al., 2017). In total, we have implemented 15 new mass-loss prescriptions.

Our main conclusions are:

- Mass loss rates for massive stars (with $10 < M_{\text{ZAMS}}/M_{\odot} < 100$) on the MS are reasonably well constrained, and even the factor of 2–3 uncertainty in these rates (Björklund et al., 2023; Krtićka & Kubát, 2018; Vink et al., 2001) is likely to be subdominant to the impact of uncertainties in mass-loss rates during later evolutionary phases.
- For massive RSGs, it appears that there is still a large amount of variation in the determination of mass-loss rates (Wen et al., 2024). In the case of high mass-loss rates (e.g., Vink & Sabhahit, 2023; Yang et al., 2023), this leads to RSGs being able to lose their hydrogen envelopes, potentially providing a solution to the missing red supergiant problem (Smartt et al., 2009). Alternatively, low mass-loss rates (Beasor et al., 2020, 2023; Decin et al., 2024) imply that massive RSGs are unable to lose their hydrogen envelopes

through steady-state winds alone, although pulsations/eruptive mass loss may still provide an alternative mechanism to remove the envelope.

- Empirical mass-loss rate prescriptions are predominantly calibrated only at the relatively high metallicities of the Milky Way, the Magellanic Clouds (e.g., Wen et al., 2024; Yang et al., 2023) and other nearby galaxies (e.g., Wang et al., 2021). These prescriptions must then be extrapolated to the much lower metallicities ($Z \lesssim 10^{-3}$) relevant for binary black hole formation.
- With our updated winds prescription (including reduced WR mass-loss rates), we are unable to produce black holes at solar metallicity more massive than $\sim 20 M_{\odot}$. However, the details of the stellar evolution models used may be able to help explain this discrepancy, including models of stellar response to mass loss (Agrawal, Hurley, Stevenson, Szécsi, & Flynn, 2020; Agrawal et al., 2022; Shikauchi et al., 2024).
- With our updated winds prescription, massive stellar-mass black holes such as Gaia BH3 (Panuzzo et al., 2024) can form at metallicities $Z \lesssim 3 \times 10^{-3}$.
- The yield of merging BBHs is sensitive to uncertainties in mass-loss rates, especially in WR and RSG phases. The yields of merging BNSs and NSBHs are much less sensitive to uncertainties in mass-loss rates, giving similar predictions to van Son et al. (2024).

Recently, Wen et al. (2024) and Antoniadis et al. (2024) have presented empirical studies of the mass-loss rates of large samples of RSGs in the Large Magellanic Cloud (LMC), similar to that of Yang et al. (2023) for the SMC. These studies identify a turning point in the trend of mass-loss rates for stars

with luminosity at around $\log L/L_{\odot} = 4.4$. Below this luminosity, they find RSG mass-loss rates at least an order of magnitude lower than those of Yang et al. (2023) and other contemporary RSG prescriptions. This finding may be due to the metallicity of the LMC, or may indicate a systematic uncertainty due to differences in modeling approaches between Wen et al. (2024), Antoniadis et al. (2024) and Yang et al. (2023). These recent studies indicate that whilst empirical samples of RSGs are becoming larger and better studied, we still do not have a complete understanding of RSG mass-loss and its scaling with metallicity.

The authors acknowledge support from the Australian Research Council (ARC) Centre of Excellence for Gravitational Wave Discovery (OzGrav), through project number CE170100004 and CE230100016. Simon Stevenson is a recipient of an ARC Discovery Early Career Research Award (DE220100241). AACS is funded by the Deutsche Forschungsgemeinschaft (DFG, German Research Foundation) in the form of an Emmy Noether Research Group – Project-ID 445674056 (SA4064/1-1, PI Sander). AACS further acknowledges support from the Federal Ministry of Education and Research (BMBF) and the Baden-Württemberg Ministry of Science as part of the Excellence Strategy of the German Federal and State Governments. BF acknowledges support from the National Science Foundation under grant PHY-2146528, OzGrav through their international visitor program, the Simons Foundation through their sabbatical visitor program, and CERN through their Scientific Associate program. TW acknowledges support from NASA ATP grant 80NSSC24K0768.

COMPAS (Riley et al., 2022b). Our input files are available here. [Reminder to include zenodo link]

REFERENCES CITED

- Aasi, J., Abbott, B. P., Abbott, R., Abbott, T., Abernathy, M. R., Ackley, K., . . . Zweizig, J. (2015, March). Advanced ligo. *Classical and Quantum Gravity*, *32*(7), 074001. Retrieved from <http://dx.doi.org/10.1088/0264-9381/32/7/074001> doi: 10.1088/0264-9381/32/7/074001
- Abac, A. G., & Abbott, R. e. a. (2025, April). Search for continuous gravitational waves from known pulsars in the first part of the fourth ligo-virgo-kagra observing run. *The Astrophysical Journal*, *983*(2), 99. Retrieved from <http://dx.doi.org/10.3847/1538-4357/adb3a0> doi: 10.3847/1538-4357/adb3a0
- Abbott, B., Abbott, R., Abbott, T., Abernathy, M., Acernese, F., Ackley, K., . . . et al. (2016, Mar). GW150914: The Advanced LIGO Detectors in the Era of First Discoveries. *Physical Review Letters*, *116*(13). Retrieved from <http://dx.doi.org/10.1103/PhysRevLett.116.131103> doi: 10.1103/physrevlett.116.131103
- Abbott, B. P. (2017, October). Multi-messenger observations of a binary neutron star merger*. *The Astrophysical Journal Letters*, *848*(2), L12. Retrieved from <http://dx.doi.org/10.3847/2041-8213/aa91c9> doi: 10.3847/2041-8213/aa91c9
- Abbott, B. P., Abbott, R., Abbott, T. D., Abernathy, M. R., Acernese, F., Ackley, K., . . . et al. (2016, February). Astrophysical Implications of the Binary Black-hole Merger GW150914. , *818*(2), L22. doi: 10.3847/2041-8205/818/2/L22
- Abbott, B. P., Abbott, R., Abbott, T. D., Abernathy, M. R., Acernese, F., Ackley, K., . . . et al. (2016). Observation of gravitational waves from a binary black hole merger. *Physical Review Letters*, *116*(6), 061102. doi: 10.1103/PhysRevLett.116.061102
- Abbott, B. P., Abbott, R., Abbott, T. D., Abernathy, M. R., Acernese, F., Ackley, K., . . . et al. (2016a, February). Observation of Gravitational Waves from a Binary Black Hole Merger. , *116*(6), 061102. doi: 10.1103/PhysRevLett.116.061102
- Abbott, B. P., Abbott, R., Abbott, T. D., Abernathy, M. R., Acernese, F., Ackley, K., . . . et al. (2016b, February). Observation of Gravitational Waves from a Binary Black Hole Merger. *Physical Review Letters*, *116*(6), 061102. doi: 10.1103/PhysRevLett.116.061102

- Abbott, B. P., Abbott, R., Abbott, T. D., Abraham, S., Acernese, F., Ackley, K., ... Zweizig, J. (2020a, February). A guide to ligo–virgo detector noise and extraction of transient gravitational-wave signals. *Classical and Quantum Gravity*, *37*(5), 055002. Retrieved from <http://dx.doi.org/10.1088/1361-6382/ab685e> doi: 10.1088/1361-6382/ab685e
- Abbott, B. P., Abbott, R., Abbott, T. D., Abraham, S., Acernese, F., Ackley, K., ... et al. (2020b, Feb). A guide to ligo–virgo detector noise and extraction of transient gravitational-wave signals. *Classical and Quantum Gravity*, *37*(5), 055002. Retrieved from <http://dx.doi.org/10.1088/1361-6382/ab685e> doi: 10.1088/1361-6382/ab685e
- Abbott, B. P., Abbott, R., Abbott, T. D., Abraham, S., Acernese, F., Ackley, K., ... et al. (2020c, Sep). Prospects for observing and localizing gravitational-wave transients with advanced ligo, advanced virgo and kagra. *Living Reviews in Relativity*, *23*(1). Retrieved from <http://dx.doi.org/10.1007/s41114-020-00026-9> doi: 10.1007/s41114-020-00026-9
- Abbott, B. P., Abbott, R., Abbott, T. D., Acernese, F., Ackley, K., Adams, C., ... et al. (2017, October). GW170817: Observation of Gravitational Waves from a Binary Neutron Star Inspiral. , *119*(16), 161101. doi: 10.1103/PhysRevLett.119.161101
- Abbott, B. P., others (LIGO Scientific Collaboration, & Collaboration), V. (2016a). Binary black hole mergers in the first advanced ligo observing run. *Physical Review X*, *6*(4), 041015. doi: 10.1103/PhysRevX.6.041015
- Abbott, B. P., others (LIGO Scientific Collaboration, & Collaboration), V. (2016b). Properties of the binary black hole merger gw150914. *Phys. Rev. Lett.*, *116*(24), 241102. doi: 10.1103/PhysRevLett.116.241102
- Abbott, B. P., others (LIGO Scientific Collaboration, & Collaboration), V. (2019). Gwtc-1: A gravitational-wave transient catalog of compact binary mergers observed by ligo and virgo during the first and second observing runs. *Phys. Rev. X*, *9*, 031040. doi: 10.1103/PhysRevX.9.031040
- Abbott, D. C., & Conti, P. S. (1987, January). Wolf-rayet stars. , *25*, 113-150. doi: 10.1146/annurev.aa.25.090187.000553

- Abbott, R., Abbott, T., Abraham, S., Acernese, F., Ackley, K., Adams, C., . . . et al. (2020, Sep). Gw190521: A binary black hole merger with a total mass of 150m. *Physical Review Letters*, *125*(10). Retrieved from <http://dx.doi.org/10.1103/PhysRevLett.125.101102> doi: 10.1103/physrevlett.125.101102
- Abbott, R., Abbott, T. D., Abraham, S., Acernese, F., Ackley, K., Adams, A., . . . et al. (2021, July). Observation of Gravitational Waves from Two Neutron Star-Black Hole Coalescences. , *915*(1), L5. doi: 10.3847/2041-8213/ac082e
- Abbott, R., Abbott, T. D., Abraham, S., Acernese, F., Ackley, K., Adams, C., . . . et al. (2021, Jan). Open data from the first and second observing runs of advanced ligo and advanced virgo. *SoftwareX*, *13*, 100658. Retrieved from <http://dx.doi.org/10.1016/j.softx.2021.100658> doi: 10.1016/j.softx.2021.100658
- Abbott, R., Abbott, T. D., Acernese, F., Ackley, K., Adams, C., Adhikari, N., . . . et al. (2023, October). GWTC-3: Compact Binary Coalescences Observed by LIGO and Virgo during the Second Part of the Third Observing Run. *Physical Review X*, *13*(4), 041039. doi: 10.1103/PhysRevX.13.041039
- Abbott, R., others (LIGO Scientific Collaboration, & Collaboration), V. (2021). Constraints on cosmic strings using data from the third advanced ligo-virgo observing run. *Physical Review Letters*, *126*(24), 241102. doi: 10.1103/PhysRevLett.126.241102
- Abbott, R., others (LIGO Scientific Collaboration, & Collaboration), V. (2024). Gravitational waves detected by a burst search in ligo/virgo's third observing run. *arXiv preprint arXiv:2410.15191*.
- Adams, S. M., Kochanek, C. S., Gerke, J. R., Stanek, K. Z., & Dai, X. (2017a). The search for failed supernovae with the large binocular telescope: Confirmation of a disappearing star. *Monthly Notices of the Royal Astronomical Society*, *468*(4), 4968–4981. doi: 10.1093/mnras/stx816
- Adams, S. M., Kochanek, C. S., Gerke, J. R., Stanek, K. Z., & Dai, X. (2017b, April). The search for failed supernovae with the large binocular telescope: confirmation of a disappearing star. *Monthly Notices of the Royal Astronomical Society*, *468*(4), 4968–4981. Retrieved from <http://dx.doi.org/10.1093/mnras/stx816> doi: 10.1093/mnras/stx816
- Aerts, C., Christensen-Dalsgaard, J., & Kurtz, D. W. (2010). *Asteroseismology*. Springer Science & Business Media. doi: 10.1007/978-1-4020-5803-5

- Agrawal, P., Hurley, J., Stevenson, S., Szécsi, D., & Flynn, C. (2020, October). The fates of massive stars: exploring uncertainties in stellar evolution with METISSE. , *497*(4), 4549-4564. doi: 10.1093/mnras/staa2264
- Agrawal, P., Szécsi, D., Stevenson, S., Eldridge, J. J., & Hurley, J. (2022, June). Explaining the differences in massive star models from various simulations. , *512*(4), 5717-5725. doi: 10.1093/mnras/stac930
- Ajith, P., Boyle, M., Brown, D. A., et al. (2012). The ninja-2 catalog of hybrid post-newtonian/numerical-relativity waveforms for non-precessing black-hole binaries. *Classical and Quantum Gravity*, *29*(12), 124001. doi: 10.1088/0264-9381/29/12/124001
- Andersson, N. (2011). Gravitational waves from instabilities in relativistic stars. *Proceedings of the International Astronomical Union*, *6*, 261–272. doi: 10.1017/S1743921311027922
- Antoniadis, K., Bonanos, A. Z., de Wit, S., Zapartas, E., Munoz-Sanchez, G., & Maravelias, G. (2024, January). Establishing a mass-loss rate relation for red supergiants in the Large Magellanic Cloud. *arXiv e-prints*, arXiv:2401.15163. doi: 10.48550/arXiv.2401.15163
- Antonini, F., Gieles, M., Gualandris, A., Heggie, D. C., & Trenti, M. (2019). Binary black hole mergers from field triples: Properties, rates, and the impact of the kozai–lidov mechanism. *The Astrophysical Journal*, *871*(1), 91. Retrieved from <https://arxiv.org/abs/1806.09683> doi: 10.3847/1538-4357/aaf6b6
- Antonini, F., & Rasio, F. A. (2016). Black hole mergers and blue stragglers from hierarchical triples formed in globular clusters. *The Astrophysical Journal*, *831*(2), 187. Retrieved from <https://arxiv.org/abs/1606.04889> doi: 10.3847/0004-637X/831/2/187
- Ashton, G., Hübner, M., Lasky, P. D., Talbot, C., Ackley, K., Biscoveanu, S., ... et al. (2019, Apr). Bilby: A user-friendly bayesian inference library for gravitational-wave astronomy. *The Astrophysical Journal Supplement Series*, *241*(2). Retrieved from <http://dx.doi.org/10.3847/1538-4365/ab06fc> doi: 10.3847/1538-4365/ab06fc
- Astone, P., et al. (1997). The gravitational wave detector auriga. *Astroparticle Physics*, *7*(3), 231–243. doi: 10.1016/S0927-6505(97)00015-1
- Astone, P., et al. (2001). The international gravitational event collaboration: status of the network. *Classical and Quantum Gravity*, *18*(19), S243–S252. doi: 10.1088/0264-9381/18/19/301

- Balbinot, E., Dodd, E., Matsuno, T., Lardo, C., Helmi, A., Panuzzo, P., ... Starkenburg, E. (2024, April). The 33 M_{\odot} black hole Gaia BH3 is part of the disrupted ED-2 star cluster. *arXiv e-prints*, arXiv:2404.11604. doi: 10.48550/arXiv.2404.11604
- Barkat, Z., Rakavy, G., & Sack, N. (1967). Dynamics of supernova explosion resulting from pair formation. *Physical Review Letters*, 18(9), 379–381. doi: 10.1103/PhysRevLett.18.379
- Barnes, S. A. (2007). Ages for illustrative field stars using gyrochronology: viability, limitations, and errors. *The Astrophysical Journal*, 669(2), 1167–1189. doi: 10.1086/519295
- Barrett, J. W., Gaebel, S. M., Neijssel, C. J., Vigna-Gómez, A., Stevenson, S., Berry, C. P. L., ... Mandel, I. (2018, July). Accuracy of inference on the physics of binary evolution from gravitational-wave observations. , 477(4), 4685-4695. doi: 10.1093/mnras/sty908
- Bartos, I., Kocsis, B., Haiman, Z., & Márka, S. (2017). Rapid and bright stellar-mass binary black hole mergers in active galactic nuclei. *The Astrophysical Journal*, 835(2), 165. Retrieved from <https://arxiv.org/abs/1602.03831> doi: 10.3847/1538-4357/835/2/165
- Bavera, S. S., Fragos, T., Zapartas, E., Andrews, J. J., Kalogera, V., Berry, C. P. L., ... Xing, Z. (2023, June). The formation of merging black holes with masses beyond 30 M_{\odot} at solar metallicity. *Nature Astronomy*. doi: 10.1038/s41550-023-02018-5
- Bavera, S. S. e. a. (2020). The impact of pair-instability mass loss on black hole mergers. *Astronomy Astrophysics*, 635, A97. Retrieved from <https://arxiv.org/abs/1906.12257> doi: 10.1051/0004-6361/201936528
- Beasor, E. R., Davies, B., Smith, N., van Loon, J. T., Gehrz, R. D., & Figer, D. F. (2020, March). A new mass-loss rate prescription for red supergiants. , 492(4), 5994-6006. doi: 10.1093/mnras/staa255
- Beasor, E. R., Davies, B., Smith, N., van Loon, J. T., Gehrz, R. D., & Figer, D. F. (2023, September). Correction to: 'A new mass-loss rate prescription for red supergiants'. , 524(2), 2460-2462. doi: 10.1093/mnras/stad1818
- Beasor, E. R., Hosseinzadeh, G., Smith, N., Davies, B., Jencson, J. E., Pearson, J., & Sand, D. J. (2024, April). JWST Reveals a Luminous Infrared Source at the Position of the Failed Supernova Candidate N6946-BH1. , 964(2), 171. doi: 10.3847/1538-4357/ad21fa

- Begelman, M. C., Volonteri, M., & Rees, M. J. (2006). Formation of supermassive black holes by direct collapse in pre-galactic haloes. *Monthly Notices of the Royal Astronomical Society*, *370*(1), 289–298. Retrieved from <https://arxiv.org/abs/astro-ph/0602363> doi: 10.1111/j.1365-2966.2006.10467.x
- Belczynski, K., Bulik, T., Fryer, C. L., Ruiter, A., Valsecchi, F., Vink, J. S., & Hurley, J. R. (2010, May). On the Maximum Mass of Stellar Black Holes. , *714*(2), 1217-1226. doi: 10.1088/0004-637X/714/2/1217
- Belczynski, K., Heger, A., Gladysz, W., Ruiter, A. J., Woosley, S., Wiktorowicz, G., ... Berti, E. (2016, October). The effect of pair-instability mass loss on black-hole mergers. , *594*, A97. doi: 10.1051/0004-6361/201628980
- Belczynski, K., Holz, D. E., Bulik, T., & O’Shaughnessy, R. (2016, June). The first gravitational-wave source from the isolated evolution of two stars in the 40-100 solar mass range. , *534*(7608), 512-515. doi: 10.1038/nature18322
- Belczynski, K., Kalogera, V., Rasio, F. A., Taam, R. E., Zezas, A., Bulik, T., ... Ivanova, N. (2008, Jan). Compact object modeling with the startrack population synthesis code. *The Astrophysical Journal Supplement Series*, *174*(1), 223–260. Retrieved from <http://dx.doi.org/10.1086/521026> doi: 10.1086/521026
- Belczynski, K., Klencki, J., Fields, C. E., Olejak, A., Berti, E., O’Shaughnessy, R., ... Bulik, T. (2020). Evolutionary roads to low effective spin binary black holes. *Astronomy Astrophysics*, *636*, A104. Retrieved from <https://arxiv.org/abs/1706.07053> doi: 10.1051/0004-6361/201936528
- Belczynski, K., Ryu, T., Perna, R., Berti, E., Tanaka, T. L., & Bulik, T. (2017). The origin of low spin of black holes in ligo/virgo mergers. *Monthly Notices of the Royal Astronomical Society*, *471*(4), 4702–4721. Retrieved from <https://arxiv.org/abs/1706.07053> doi: 10.1093/mnras/stx1759
- Bernini-Peron, M., Marcolino, W. L. F., Sander, A. A. C., Bouret, J. C., Ramachandran, V., Saling, J., ... Najarro, F. (2023, September). Clumping and X-rays in cooler B supergiant stars. , *677*, A50. doi: 10.1051/0004-6361/202346469
- Bestenlehner, J. M. (2020, April). Mass loss and the Eddington parameter: a new mass-loss recipe for hot and massive stars. , *493*(3), 3938-3946. doi: 10.1093/mnras/staa474

- Bestenlehner, J. M., Gräfener, G., Vink, J. S., Najarro, F., de Koter, A., Sana, H., . . . Walborn, N. R. (2014, October). The VLT-FLAMES Tarantula Survey. XVII. Physical and wind properties of massive stars at the top of the main sequence. , *570*, A38. doi: 10.1051/0004-6361/201423643
- Björklund, R., Sundqvist, J. O., Singh, S. M., Puls, J., & Najarro, F. (2023, August). New predictions for radiation-driven, steady-state mass-loss and wind-momentum from hot, massive stars. III. Updated mass-loss rates for stellar evolution. , *676*, A109. doi: 10.1051/0004-6361/202141948
- Bonanos, A. Z., Tramper, F., de Wit, S., Christodoulou, E., Munoz-Sanchez, G., Antoniadis, K., . . . Zapartas, E. (2023, December). Investigating episodic mass loss in evolved massive stars: I. Spectroscopy of dusty massive stars in ten southern galaxies. *arXiv e-prints*, arXiv:2312.04626. doi: 10.48550/arXiv.2312.04626
- Bono, G., Marconi, M., & Stellingwerf, R. F. (2000). Pulsating variables in the hertzsprung–russell diagram. *Astronomy and Astrophysics*, *360*, 245–256.
- Bouret, J. C., Martins, F., Hillier, D. J., Marcolino, W. L. F., Rocha-Pinto, H. J., Georgy, C., . . . Hubeny, I. (2021, March). Massive stars in the Small Magellanic Cloud. Evolution, rotation, and surface abundances. , *647*, A134. doi: 10.1051/0004-6361/202039890
- Boyajian, T. S., von Braun, K., van Belle, G., et al. (2012). Stellar diameters and temperatures. ii. main-sequence k-and m-stars. *The Astrophysical Journal*, *757*(2), 112.
- B. P. Abbott, t. V. C. t. K. C., The LIGO Scientific Collaboration. (2020, September). Prospects for observing and localizing gravitational-wave transients with advanced ligo, advanced virgo and kagra. *Living Reviews in Relativity*, *23*(1). Retrieved from <http://dx.doi.org/10.1007/s41114-020-00026-9> doi: 10.1007/s41114-020-00026-9
- Braginsky, V., Ryazhskaya, O., & Vyatchanin, S. (2006, Jan). Notes about noise in gravitational wave antennas created by cosmic rays. *Physics Letters A*, *350*(1-2), 1–4. Retrieved from <http://dx.doi.org/10.1016/j.physleta.2005.09.073> doi: 10.1016/j.physleta.2005.09.073
- Branca, A., Bonaldi, M., Cerdonio, M., Conti, L., Falferi, P., Marin, F., . . . Zendri, J.-P. (2017, January). Search for an ultralight scalar dark matter candidate with the auriga detector. *Physical Review Letters*, *118*(2). Retrieved from <http://dx.doi.org/10.1103/PhysRevLett.118.021302> doi: 10.1103/physrevlett.118.021302

- Brands, S. A., de Koter, A., Bestenlehner, J. M., Crowther, P. A., Sundqvist, J. O., Puls, J., . . . Vink, J. S. (2022, July). The R136 star cluster dissected with Hubble Space Telescope/STIS. III. The most massive stars and their clumped winds. , *663*, A36. doi: 10.1051/0004-6361/202142742
- Breivik, K., Chatterjee, S., Larson, S. L., & Kalogera, V. (2020). Cosmic variance in binary population synthesis. *The Astrophysical Journal*, *898*, 71. doi: 10.3847/1538-4357/ab9d85
- Broekgaarden, F. S., Berger, E., Stevenson, S., Justham, S., Mandel, I., Chruślińska, M., . . . Neijssel, C. J. (2022, November). Impact of massive binary star and cosmic evolution on gravitational wave observations - II. Double compact object rates and properties. , *516*(4), 5737-5761. doi: 10.1093/mnras/stac1677
- Bruzual, G., & Charlot, S. (2003). Stellar population synthesis at the resolution of 2003. *Monthly Notices of the Royal Astronomical Society*, *344*(4), 1000–1028. doi: 10.1046/j.1365-8711.2003.06897.x
- Cabero, M., Lundgren, A., Nitz, A. H., Dent, T., Barker, D., Goetz, E., . . . et al. (2019, Jul). Blip glitches in advanced ligo data. *Classical and Quantum Gravity*, *36*(15), 155010. Retrieved from <http://dx.doi.org/10.1088/1361-6382/ab2e14> doi: 10.1088/1361-6382/ab2e14
- Caprini, C., & Figueroa, D. G. (2018). Cosmological backgrounds of gravitational waves. *Class. Quantum Grav.*, *35*, 163001. doi: 10.1088/1361-6382/aac608
- Carroll, B. W., & Ostlie, D. A. (2007). *An Introduction to Modern Astrophysics* (2nd (International) ed.). Addison-Wesley, San Francisco: Pearson.
- Castor, J. I., Abbott, D. C., & Klein, R. I. (1975, January). Radiation-driven winds in Of stars. , *195*, 157-174. doi: 10.1086/153315
- Chabrier, G., & Baraffe, I. (1997). Structure and evolution of low-mass stars. *Astronomy and Astrophysics*, *327*, 1039–1053. Retrieved from <https://ui.adsabs.harvard.edu/abs/1997A&A...327.1039C>
- Chandrasekhar, S. (1931). The maximum mass of ideal white dwarfs. *Astrophysical Journal*, *74*, 81–82. doi: 10.1086/143324
- Chaplin, W. J., & Miglio, A. (2013). Asteroseismology of solar-type and red-giant stars. *Annual Review of Astronomy and Astrophysics*, *51*, 353–392. doi: 10.1146/annurev-astro-082812-140938

- Chatterjee, D., Mandal, S., & Mukhopadhyay, B. (2024). Gravitational-wave fingerprints of neutron star starquakes. *arXiv preprint*. Retrieved from <https://arxiv.org/abs/2404.03675>
- Chatterji, S., Blackburn, L., Martin, G., & Katsavounidis, E. (2004, Sep). Multiresolution techniques for the detection of gravitational-wave bursts. *Classical and Quantum Gravity*, *21*(20), S1809–S1818. Retrieved from <http://dx.doi.org/10.1088/0264-9381/21/20/024> doi: 10.1088/0264-9381/21/20/024
- Chelli, A., Duvert, G., Bourgès, L., Mella, G., Lafrasse, S., Bonneau, D., & Chesneau, O. (2016, April). Pseudomagnitudes and differential surface brightness: Application to the apparent diameter of stars. *Astronomy and Astrophysics*, *589*, A112. Retrieved from <http://dx.doi.org/10.1051/0004-6361/201527484> doi: 10.1051/0004-6361/201527484
- Choi, J., Dotter, A., Conroy, C., Cantiello, M., Paxton, B., & Johnson, B. D. (2016). Mesa isochrones and stellar tracks (mist). i. solar-scaled models. *The Astrophysical Journal*, *823*(2), 102. Retrieved from <https://arxiv.org/abs/1604.08592> doi: 10.3847/0004-637X/823/2/102
- Collaboration, T. L. S., the Virgo Collaboration, & et. al., R. A. (2021). *Gwtc-2.1: Deep extended catalog of compact binary coalescences observed by ligo and virgo during the first half of the third observing run*.
- Cornish, N. J. (2021). Rapid and Robust Parameter Inference for Binary Mergers. *Phys. Rev. D*, *103*(10), 104057. doi: 10.1103/PhysRevD.103.104057
- Cornish, N. J., & Littenberg, T. B. (2007). Tests of bayesian model selection techniques for gravitational wave astronomy. *Phys. Rev. D*, *76*, 083006. doi: 10.1103/PhysRevD.76.083006
- Cornish, N. J., & Littenberg, T. B. (2015, Jun). Bayeswave: Bayesian inference for gravitational wave bursts and instrument glitches. *Classical and Quantum Gravity*, *32*(13), 135012. Retrieved from <http://dx.doi.org/10.1088/0264-9381/32/13/135012> doi: 10.1088/0264-9381/32/13/135012
- Cornish, N. J., Littenberg, T. B., Bécsy, B., Chatziioannou, K., Clark, J. A., Ghonge, S., & Millhouse, M. (2021). BayesWave analysis pipeline in the era of gravitational wave observations. *Phys. Rev. D*, *103*(4), 044006. doi: 10.1103/PhysRevD.103.044006

- Costa, G., Bressan, A., Mapelli, M., Marigo, P., Iorio, G., & Spera, M. (2021, March). Formation of GW190521 from stellar evolution: the impact of the hydrogen-rich envelope, dredge-up, and $^{12}\text{C}(\alpha, \gamma)^{16}\text{O}$ rate on the pair-instability black hole mass gap. , *501*(3), 4514-4533. doi: 10.1093/mnras/staa3916
- Crowther, P. A. (2007, September). Physical Properties of Wolf-Rayet Stars. , *45*(1), 177-219. doi: 10.1146/annurev.astro.45.051806.110615
- Crowther, P. A., & Walborn, N. R. (2011, September). Spectral classification of O2-3.5 If*/WN5-7 stars. , *416*(2), 1311-1323. doi: 10.1111/j.1365-2966.2011.19129.x
- da Silva, L., Girardi, L., Pasquini, L., & et al. (2006). Basic physical parameters of a selected sample of evolved stars. *Astronomy Astrophysics*, *458*, 609–623. doi: 10.1051/0004-6361:20065105
- Davies, B., & Beasor, E. R. (2020, June). ‘on the red supergiant problem’: a rebuttal, and a consensus on the upper mass cut-off for ii-p progenitors. *Monthly Notices of the Royal Astronomical Society: Letters*, *496*(1), L142–L146. Retrieved from <http://dx.doi.org/10.1093/mnrasl/slaa102> doi: 10.1093/mnrasl/slaa102
- Davis, D., White, L. V., & Saulson, P. R. (2020, Jun). Utilizing aligo glitch classifications to validate gravitational-wave candidates. *Classical and Quantum Gravity*, *37*(14), 145001. Retrieved from <http://dx.doi.org/10.1088/1361-6382/ab91e6> doi: 10.1088/1361-6382/ab91e6
- de Jager, C. (1998, January). The yellow hypergiants. , *8*(3), 145-180. doi: 10.1007/s001590050009
- de Jager, C., Nieuwenhuijzen, H., & van der Hucht, K. A. (1988, February). Mass loss rates in the Hertzsprung-Russell diagram. , *72*, 259-289.
- de Mink, S. E., Cantiello, M., Langer, N., Pols, O. R., Brott, I., & Yoon, S. C. (2009, April). Rotational mixing in massive binaries. Detached short-period systems. , *497*(1), 243-253. doi: 10.1051/0004-6361/200811439
- de Wit, S., Bonanos, A. Z., Antoniadis, K., Zapartas, E., Ruiz, A., Britavskiy, N., ... Tsopele, A. (2024, February). Investigating episodic mass loss in evolved massive stars: II. Physical properties of red supergiants at subsolar metallicity. *arXiv e-prints*, arXiv:2402.12442. doi: 10.48550/arXiv.2402.12442

- Decin, L. (2021, September). Evolution and Mass Loss of Cool Ageing Stars: a Daedalean Story. , *59*, 337-389. doi: 10.1146/annurev-astro-090120-033712
- Decin, L., Richards, A. M. S., Marchant, P., & Sana, H. (2024, January). ALMA detection of CO rotational line emission in red supergiant stars of the massive young star cluster RSGC1. Determination of a new mass-loss rate prescription for red supergiants. , *681*, A17. doi: 10.1051/0004-6361/202244635
- de Mink, S., & Mandel, I. (2016). Chemically homogeneous evolution in massive binaries: producing gravitational-wave sources with small black hole spins. *Monthly Notices of the Royal Astronomical Society*, *460*(4), 3545–3553. Retrieved from <https://arxiv.org/abs/1603.02291> doi: 10.1093/mnras/stw1219
- Deupree, R. G. (1990). Two-dimensional stellar evolution calculations including rotation and magnetic fields. *The Astrophysical Journal*, *357*, 175–186. doi: 10.1086/168904
- de Waele, A. T. A. M., et al. (1993). The cryogenic gravitational wave antenna explorer. *Cryogenics*, *33*(9), 853–858. doi: 10.1016/0011-2275(93)90233-V
- Dillon, J. V., Langmore, I., Tran, D., Brevdo, E., Vasudevan, S., Moore, D., ... Saurous, R. A. (2017). *Tensorflow distributions*.
- Donati, J.-F., & Brown, S. F. (1997). Zeeman-doppler imaging of active stars. v. sensitivity of maximum entropy magnetic maps to field orientation. *Astronomy and Astrophysics*, *326*, 1135–1142.
- Dosopoulou, F., & Kalogera, V. (2016). Orbital evolution of eccentric binaries under the influence of isotropic winds and conservative and non-conservative mass transfer. *The Astrophysical Journal*, *825*(1), 71. Retrieved from <https://arxiv.org/abs/1603.06939> doi: 10.3847/0004-637X/825/1/71
- Duchêne, G., & Kraus, A. (2013). Stellar multiplicity. *Annual Review of Astronomy and Astrophysics*, *51*, 269–310. Retrieved from <https://arxiv.org/abs/1303.3028> doi: 10.1146/annurev-astro-081710-102602
- Dupret, M.-A., Grigahcène, A., Garrido, R., Gabriel, M., & Scuflaire, R. (2005). Theoretical instability strips for γ doradus and δ scuti stars. *Astronomy and Astrophysics*, *435*, 927–939. doi: 10.1051/0004-6361:20042273
- Eggleton, P. P. (1983). Approximations to the radii of roche lobes. *The Astrophysical Journal*, *268*, 368–369. doi: 10.1086/160960

- Einstein, A. (1915). Die feldgleichungen der gravitation. *Sitzung der physikalische-mathematischen Klasse*, 25, 844–847.
- Eker, Z., Soyduğan, F., Soyduğan, E., & et al. (2015). Main-sequence effective temperatures from 2mass photometry. *The Astronomical Journal*, 149(4), 131. doi: 10.1088/0004-6256/149/4/131
- El-Badry, K. (2024, April). Formation of a $33 M_{\odot}$ black hole in a low-metallicity binary. *arXiv e-prints*, arXiv:2404.13047. doi: 10.48550/arXiv.2404.13047
- El-Badry, K., Rix, H.-W., Cendes, Y., Rodriguez, A. C., Conroy, C., Quataert, E., ... Faigler, S. (2023, May). A red giant orbiting a black hole. , 521(3), 4323-4348. doi: 10.1093/mnras/stad799
- Eldridge, J. J., & Stanway, E. R. (2009). Spectral population synthesis including massive binaries. *Monthly Notices of the Royal Astronomical Society*, 400, 1019-1028. doi: 10.1111/j.1365-2966.2009.15514.x
- et. al., D. D. (2021). Ligo detector characterization in the second and third observing runs.
- et.al., R. A. (2021). Gwtc-2: Compact binary coalescences observed by ligo and virgo during the first half of the third observing run.
- et al. (LIGO Scientific Collaboration, B. P. A., & Collaboration), V. (2019). Search for the isotropic stochastic background using data from advanced ligo’s second observing run. *Phys. Rev. D*, 100, 061101. doi: 10.1103/PhysRevD.100.061101
- Farmer, R., Renzo, M., de Mink, S. E., Marchant, P., & Justham, S. (2019, December). Mind the Gap: The Location of the Lower Edge of the Pair-instability Supernova Black Hole Mass Gap. , 887(1), 53. doi: 10.3847/1538-4357/ab518b
- Farr, B., & Farr, W. M. (2015). kombine: a kernel-density-based, embarrassingly parallel ensemble sampler.
(in prep)
- Farrell, E., Groh, J. H., Hirschi, R., Murphy, L., Kaiser, E., Ekström, S., ... Meynet, G. (2021, March). Is GW190521 the merger of black holes from the first stellar generations? , 502(1), L40-L44. doi: 10.1093/mnrasl/slaa196
- Fernández, R., Quataert, E., Kashiyaama, K., & Coughlin, E. R. (2018, May). Mass ejection in failed supernovae: variation with stellar progenitor. , 476(2), 2366-2383. doi: 10.1093/mnras/sty306

- Foreman-Mackey, D., Hogg, D. W., Lang, D., & Goodman, J. (2013, Mar). emcee: The mcmc hammer. *Publications of the Astronomical Society of the Pacific*, *125*(925), 306–312. Retrieved from <http://dx.doi.org/10.1086/670067> doi: 10.1086/670067
- Forward, R. L. (1978). Wideband laser-interferometer gravitational-radiation experiment. *Physical Review D*, *17*(2), 379–390. doi: 10.1103/PhysRevD.17.379
- Fowler, W. A., & Hoyle, F. (1964). Neutrino processes and pair formation in massive stars and supernovae. *Astrophysical Journal Supplement Series*, *9*, 201–319. doi: 10.1086/190103
- Fowler, W. A., & Hoyle, F. (1964, December). Neutrino Processes and Pair Formation in Massive Stars and Supernovae. , *9*, 201. doi: 10.1086/190103
- Fragos, T., Andrews, J. J., Bavera, S. S., Berry, C. P. L., Coughlin, S., Dotter, A., ... Zapartas, E. (2023). Posydon: A general-purpose population synthesis code with detailed binary-evolution simulations. *The Astrophysical Journal*, *944*, 58. doi: 10.3847/1538-4357/acac2e
- Fraley, G. S. (1968). Supernovae explosions induced by pair-production instability. *Astrophysical Journal*, *151*, 587–610. doi: 10.1086/149465
- Frebel, A. (2010). Stellar archaeology: Exploring the universe with metal-poor stars (ludwig biermann award lecture 2009). *Astronomische Nachrichten*, *331*(5), 474–488. Retrieved from <https://doi.org/10.1002/asna.201011355> doi: 10.1002/asna.201011355
- Freeman, K., & Bland-Hawthorn, J. (2002). The new galaxy: Signatures of its formation. *Annual Review of Astronomy and Astrophysics*, *40*, 487–537. Retrieved from <https://doi.org/10.1146/annurev.astro.40.060401.093840> doi: 10.1146/annurev.astro.40.060401.093840
- Freytag, B., Steffen, M., Ludwig, H.-G., Wedemeyer-Böhm, S., Schaffenberger, W., & Steiner, O. (2012). Simulations of stellar convection with co5bold. *Journal of Computational Physics*, *231*(3), 919–959. doi: 10.1016/j.jcp.2011.09.026
- Fryer, C. L. (1999). Mass limits for black hole formation. *The Astrophysical Journal*, *522*, 413–418. doi: 10.1086/307647

- Fryer, C. L., Belczynski, K., Wiktorowicz, G., Dominik, M., Kalogera, V., & Holz, D. E. (2012, March). Compact remnant mass function: Dependence on the explosion mechanism and metallicity. *The Astrophysical Journal*, *749*(1), 91. Retrieved from <http://dx.doi.org/10.1088/0004-637X/749/1/91> doi: 10.1088/0004-637x/749/1/91
- Fryxell, B., Olson, K., Ricker, P., & et al. (2000). Flash: An adaptive mesh hydrodynamics code for modeling astrophysical thermonuclear flashes. *The Astrophysical Journal Supplement Series*, *131*(1), 273–334. doi: 10.1086/317361
- Fullerton, A. W., Massa, D. L., & Prinja, R. K. (2006, February). The Discordance of Mass-Loss Estimates for Galactic O-Type Stars. , *637*(2), 1025-1039. doi: 10.1086/498560
- García, R. A., Hekker, S., Stello, D., et al. (2011). Rotation and magnetism of kepler solar-like stars. towards asteroseismically calibrated age-rotation relations. *Monthly Notices of the Royal Astronomical Society: Letters*, *414*(1), L6–L10. Retrieved from <https://arxiv.org/abs/1103.0382> doi: 10.1111/j.1745-3933.2011.01042.x
- Georgy, C. (2012, February). Yellow supergiants as supernova progenitors: an indication of strong mass loss for red supergiants? , *538*, L8. doi: 10.1051/0004-6361/201118372
- Gerke, J. R., Kochanek, C. S., & Stanek, K. Z. (2014). The search for failed supernovae with the large binocular telescope: First candidates. *The Astrophysical Journal*, *792*(2), 118. doi: 10.1088/0004-637X/792/2/118
- Gertsenshtein, M. E., & Pustovoit, V. I. (1963). On the detection of low frequency gravitational waves. *Soviet Physics JETP*, *16*(2), 433–435. (Originally published in *ZhETF* 43, 605 (1962))
- Giliberti, E., & Cambiotti, G. (2021). On the deformation of neutron stars due to starquakes and the corresponding gravitational wave emission. *Monthly Notices of the Royal Astronomical Society*, *504*(1), 709–720. Retrieved from <https://arxiv.org/abs/2102.02540> doi: 10.1093/mnras/stab870
- Goldman, S. R., van Loon, J. T., Zijlstra, A. A., Green, J. A., Wood, P. R., Nanni, A., ... Gómez, J. F. (2017, February). The wind speeds, dust content, and mass-loss rates of evolved AGB and RSG stars at varying metallicity. , *465*(1), 403-433. doi: 10.1093/mnras/stw2708

- Graham, M. J. e. a. (2020). Candidate electromagnetic counterpart to the binary black hole merger gravitational-wave event s190521g. *Physical Review Letters*, *124*(25), 251102. Retrieved from <https://arxiv.org/abs/2006.14122> doi: 10.1103/PhysRevLett.124.251102
- Gray, D. F. (2005). *The observation and analysis of stellar photospheres*. Cambridge University Press.
- Haberl, F. (2007). The magnificent seven: magnetic fields and surface temperature distributions. *Astrophysics and Space Science*, *308*, 181–190. doi: 10.1007/s10509-007-9325-4
- Hainich, R., Pasemann, D., Todt, H., Shenar, T., Sander, A., & Hamann, W. R. (2015, September). Wolf-Rayet stars in the Small Magellanic Cloud. I. Analysis of the single WN stars. , *581*, A21. doi: 10.1051/0004-6361/201526241
- Hainich, R., Rühling, U., Todt, H., Oskinova, L. M., Liermann, A., Gräfener, G., ... Hamann, W. R. (2014, May). The Wolf-Rayet stars in the Large Magellanic Cloud. A comprehensive analysis of the WN class. , *565*, A27. doi: 10.1051/0004-6361/201322696
- Hamann, W. R., Gräfener, G., & Liermann, A. (2006, October). The Galactic WN stars. Spectral analyses with line-blanketed model atmospheres versus stellar evolution models with and without rotation. , *457*(3), 1015-1031. doi: 10.1051/0004-6361:20065052
- Hamann, W. R., Gräfener, G., Liermann, A., Hainich, R., Sander, A. A. C., Shenar, T., ... Oskinova, L. M. (2019, May). The Galactic WN stars revisited. Impact of Gaia distances on fundamental stellar parameters. , *625*, A57. doi: 10.1051/0004-6361/201834850
- Hamann, W. R., & Koesterke, L. (1998, July). Spectrum formation in clumped stellar winds: consequences for the analyses of Wolf-Rayet spectra. , *335*, 1003-1008.
- Hamann, W. R., Koesterke, L., & Wessolowski, U. (1995, July). Spectral analyses of the Galactic Wolf-Rayet stars: hydrogen-helium abundances and improved stellar parameters for the WN class. , *299*, 151.
- Hansen, C. J., Kawaler, S. D., & Trimble, V. (2004). *Stellar interiors: Physical principles, structure, and evolution* (2nd ed.). New York, NY: Springer.
- Hartle, J. B. (2003). *Gravity: An introduction to einstein's general relativity*. Addison-Wesley.

- Hartwig, T., Volonteri, M., Bromm, V., Klessen, R. S., Barausse, E., Magg, M., & Stacy, A. (2016). Gravitational waves from the remnants of the first stars. *Monthly Notices of the Royal Astronomical Society*, *460*(1), L74–L78. Retrieved from <https://arxiv.org/abs/1603.05655> doi: 10.1093/mnras/slw074
- Helmling-Cornell, A. (n.d.). *Blip glitches in ligo hanford*. (<https://dcc.ligo.org/LIGO-G2001007/public>)
- Hendriks, D. D., van Son, L. A. C., Renzo, M., Izzard, R. G., & Farmer, R. (2023). *Pulsational pair-instability supernovae in gravitational-wave and electromagnetic transients*. Retrieved from <https://arxiv.org/abs/2309.09339>
- Higgins, E. R., Sander, A. A. C., Vink, J. S., & Hirschi, R. (2021, August). Evolution of Wolf-Rayet stars as black hole progenitors. , *505*(4), 4874–4889. doi: 10.1093/mnras/stab1548
- Higgins, E. R., & Vink, J. S. (2020, March). Theoretical investigation of the Humphreys-Davidson limit at high and low metallicity. , *635*, A175. doi: 10.1051/0004-6361/201937374
- Hinder, I., Ossokine, S., Pfeiffer, H. P., & Buonanno, A. (2018). Gravitational waveforms for high spin and high mass-ratio binary black holes: A synergistic use of numerical-relativity codes. *Physical Review D*, *98*(8), 084005. doi: 10.1103/PhysRevD.98.084005
- Hiramatsu, D., Howell, D. A., Van Dyk, S. D., Goldberg, J. A., Maeda, K., Moriya, T. J., ... Itagaki, K. (2021, June). The electron-capture origin of supernova 2018zd. *Nature Astronomy*, *5*(9), 903–910. Retrieved from <http://dx.doi.org/10.1038/s41550-021-01384-2> doi: 10.1038/s41550-021-01384-2
- (n.d.). In *Gravitational-wave physics and astronomy* (p. I–XIV). John Wiley & Sons, Ltd. Retrieved from <https://onlinelibrary.wiley.com/doi/abs/10.1002/9783527636037.fmatter> doi: <https://doi.org/10.1002/9783527636037.fmatter>
- Huang, S.-S. (1956). Evolution of close binaries. *The Astrophysical Journal*, *123*, 491. doi: 10.1086/146254
- Humphreys, R. M., & Davidson, K. (1979, September). Studies of luminous stars in nearby galaxies. III. Comments on the evolution of the most massive stars in the Milky Way and the Large Magellanic Cloud. , *232*, 409–420. doi: 10.1086/157301

- Humphreys, R. M., Jones, T. J., & Martin, J. C. (2023, August). Yellow Supergiants and Post-red Supergiant Evolution in the Large Magellanic Cloud. , *166*(2), 50. doi: 10.3847/1538-3881/acdd6c
- Hunter, J. D. (2007). Matplotlib: A 2d graphics environment. *Computing in Science & Engineering*, *9*(3), 90–95. doi: 10.1109/MCSE.2007.55
- Hurley, J. R., Pols, O. R., & Tout, C. A. (2000, July). Comprehensive analytic formulae for stellar evolution as a function of mass and metallicity. , *315*, 543-569. doi: 10.1046/j.1365-8711.2000.03426.x
- Hurley, J. R., Tout, C. A., & Pols, O. R. (2002, 02). Evolution of binary stars and the effect of tides on binary populations. *Monthly Notices of the Royal Astronomical Society*, *329*(4), 897-928. Retrieved from <https://doi.org/10.1046/j.1365-8711.2002.05038.x> doi: 10.1046/j.1365-8711.2002.05038.x
- Iorio, G., Torniamenti, S., Mapelli, M., Dall’Amico, M., Trani, A. A., Rastello, S., ... Arca Sedda, M. (2024, April). The boring history of Gaia BH3 from isolated binary evolution. *arXiv e-prints*, arXiv:2404.17568. doi: 10.48550/arXiv.2404.17568
- Ivanova, N., Justham, S., Chen, X., De Marco, O., Fryer, C. L., Gaburov, E., ... Webbink, R. F. (2013). Common envelope evolution: where we stand and how we can move forward. *AA Review*, *21*, 59. Retrieved from <https://arxiv.org/abs/1209.4302> doi: 10.1007/s00159-013-0059-2
- Josiek, J., Ekström, S., & Sander, A. A. C. (2024, April). Impact of main-sequence mass loss on the appearance, structure and evolution of Wolf-Rayet stars. *arXiv e-prints*, arXiv:2404.14488. doi: 10.48550/arXiv.2404.14488
- Kee, N. D., Sundqvist, J. O., Decin, L., de Koter, A., & Sana, H. (2021, February). Analytic, dust-independent mass-loss rates for red supergiant winds initiated by turbulent pressure. , *646*, A180. doi: 10.1051/0004-6361/202039224
- Khan, S., Husa, S., Hannam, M., Ohme, F., Pürrer, M., Forteza, X. J., & Bohé, A. (2016). Frequency-domain gravitational waves from nonprecessing black-hole binaries. ii. a phenomenological model for the advanced detector era. *Physical Review D*, *93*(4), 044007. doi: 10.1103/PhysRevD.93.044007
- Kimball, C., Talbot, C., Berry, C. P. L., Zevin, M., Thrane, E., Kalogera, V., ... others (2020). Evidence for hierarchical black hole mergers in the second ligo–virgo gravitational-wave catalog. *arXiv preprint arXiv:2011.05332*. Retrieved from <https://arxiv.org/abs/2011.05332>

- Kinugawa, T., Inayoshi, K., Hotokezaka, K., Nakauchi, D., & Nakamura, T. (2014). Possible indirect confirmation of the existence of pop iii massive stars by gravitational wave. *Monthly Notices of the Royal Astronomical Society*, *442*(4), 2963–2993. Retrieved from <https://arxiv.org/abs/1402.6672> doi: 10.1093/mnras/stu1022
- Kippenhahn, R., Weigert, A., & Weiss, A. (2012). *Stellar structure and evolution*. Springer.
- Koumpia, E., Oudmaijer, R. D., Graham, V., Banyard, G., Black, J. H., Wichittanakom, C., . . . Wallström, S. H. J. (2020, March). Optical and near-infrared observations of the Fried Egg Nebula. Multiple shell ejections on a 100 yr timescale from a massive yellow hypergiant. , *635*, A183. doi: 10.1051/0004-6361/201936177
- Kroupa, P. (2001). On the variation of the initial mass function. *Monthly Notices of the Royal Astronomical Society*, *322*, 231–246. doi: 10.1046/j.1365-8711.2001.04022.x
- Krtićka, J., & Kubát, J. (2017, October). Comoving frame models of hot star winds. II. Reduction of O star wind mass-loss rates in global models. , *606*, A31. doi: 10.1051/0004-6361/201730723
- Krtićka, J., & Kubát, J. (2018, April). Global hot-star wind models for stars from Magellanic Clouds. , *612*, A20. doi: 10.1051/0004-6361/201731969
- Krtićka, J., Kubát, J., & Krtićková, I. (2024, January). New mass-loss rates of Magellanic Cloud B supergiants from global wind models. , *681*, A29. doi: 10.1051/0004-6361/202347916
- Kruckow, M. U., Neunteufel, P. G., Di Stefano, R., Gao, Y., & Kobayashi, C. (2021). A catalog of potential post–common envelope binaries. *The Astrophysical Journal*, *920*(2), 86. Retrieved from <https://arxiv.org/abs/2107.05221> doi: 10.3847/1538-4357/ac10c1
- Kudritzki, R. P., & Reimers, D. (1978, November). On the absolute scale of mass-loss in red giants. II. Circumstellar absorption lines in the spectrum of alpha Sco B and mass-loss of alpha Sco A. , *70*, 227-239.
- Kutner, M. L. (2003). *Astronomy: A physical perspective* (2nd ed.). Cambridge, UK: Cambridge University Press.
- Langer, N., & Maeder, A. (1995, March). The problem of the blue-to-red supergiant ratio in galaxies. , *295*, 685.

- Latif, M. A., Schleicher, D. R. G., Schmidt, W., & Niemeyer, J. (2013). Black hole formation in the early universe. *Monthly Notices of the Royal Astronomical Society*, *433*(2), 1607–1618. Retrieved from <https://arxiv.org/abs/1304.0962> doi: 10.1093/mnras/stt817
- Lau, M. Y. M., Hirai, R., González-Bolívar, M., Price, D. J., De Marco, O., & Mandel, I. (2022, June). Common envelopes in massive stars: towards the role of radiation pressure and recombination energy in ejecting red supergiant envelopes. , *512*(4), 5462-5480. doi: 10.1093/mnras/stac049
- Laughlin, G., & Bodenheimer, P. (1997). The end of the main sequence. *The Astrophysical Journal*, *491*, L51–L54. doi: 10.1086/311068
- Littenberg, T. B., & Cornish, N. J. (2010). Bayesian inference for spectral estimation of gravitational wave detector noise. *Phys. Rev. D*, *82*, 103007. doi: 10.1103/PhysRevD.82.103007
- Lovegrove, E., & Woosley, S. E. (2013, June). Very Low Energy Supernovae from Neutrino Mass Loss. , *769*(2), 109. doi: 10.1088/0004-637X/769/2/109
- Macleod, D., Urban, A. L., Coughlin, S., Massinger, T., Pitkin, M., rngeorge, . . . Badger, T. G. (2021, April). *gwpy/gwpy: 2.0.4*. Zenodo. Retrieved from <https://doi.org/10.5281/zenodo.4723317> doi: 10.5281/zenodo.4723317
- MacLeod, M., Macias, P. J., Ramirez-Ruiz, E., Graczyk, D., & Schweizer, F. (2017). Lessons learned from the light curve of v1309 scorpii: Real-time luminous red novae and stellar mergers. *Astrophysical Journal*, *835*(2), 282. Retrieved from <https://arxiv.org/abs/1610.02016> doi: 10.3847/1538-4357/835/2/282
- Madau, P., & Rees, M. J. (2001). Massive black holes as population iii remnants. *The Astrophysical Journal Letters*, *551*(1), L27–L30. Retrieved from <https://arxiv.org/abs/astro-ph/0101223> doi: 10.1086/319848
- Mandel, I., & de Mink, S. (2016). The chemically homogeneous evolutionary channel for binary black hole mergers: Rates and properties of gravitational-wave events detectable by advanced ligo. *Monthly Notices of the Royal Astronomical Society*, *458*(3), 2634–2647. Retrieved from <https://arxiv.org/abs/1601.00007> doi: 10.1093/mnras/stw379
- Mandel, I., & Farmer, A. (2022). Merging stellar-mass binary black holes. *Physics Reports*, *955*, 1–51. doi: 10.1016/j.physrep.2021.10.002
- Mandel, I., & Farmer, A. (2022, April). Merging stellar-mass binary black holes. , *955*, 1-24. doi: 10.1016/j.physrep.2022.01.003

- Mandel, I., & Müller, B. (2020). Simple recipes for compact remnant masses and natal kicks. *Mon. Not. Roy. Astron. Soc.*, *499*(3), 3214–3221. doi: 10.1093/mnras/staa3043
- Mapelli, M. (2021). Formation Channels of Single and Binary Stellar-Mass Black Holes. In C. Bambi, S. Katsanevas, & K. D. Kokkotas (Eds.), *Handbook of gravitational wave astronomy* (p. 16). doi: 10.1007/978-981-15-4702-7_16-1
- Marchant, P., Langer, N., Podsiadlowski, P., Tauris, T. M., & Moriya, T. J. (2016). A new route towards merging massive black holes. *Astronomy Astrophysics*, *588*, A50. Retrieved from <https://arxiv.org/abs/1601.03718> doi: 10.1051/0004-6361/201628133
- Marchant, P., Renzo, M., Farmer, R., Pappas, K. M. W., Taam, R. E., de Mink, S. E., & Kalogera, V. (2019, September). Pulsational Pair-instability Supernovae in Very Close Binaries. , *882*(1), 36. doi: 10.3847/1538-4357/ab3426
- Marín Pina, D., Rastello, S., Gieles, M., Kremer, K., Fitzgerald, L., & Rando, B. (2024, April). Dynamical formation of Gaia BH3 in the progenitor globular cluster of the ED-2 stream. *arXiv e-prints*, arXiv:2404.13036. doi: 10.48550/arXiv.2404.13036
- Martinet, S., Meynet, G., Ekström, S., Georgy, C., & Hirschi, R. (2023, November). Very massive star models. I. Impact of rotation and metallicity and comparisons with observations. , *679*, A137. doi: 10.1051/0004-6361/202347514
- Mauron, N., & Josselin, E. (2011, February). The mass-loss rates of red supergiants and the de Jager prescription. , *526*, A156. doi: 10.1051/0004-6361/201013993
- McDonald, S. L. E., Davies, B., & Beasor, E. R. (2022, March). Red supergiants in M31: the Humphreys-Davidson limit at high metallicity. , *510*(3), 3132-3144. doi: 10.1093/mnras/stab3453
- McKernan, B., Ford, K. E. S., Lyra, W., & Perets, H. B. (2012). Intermediate mass black holes in agn discs - i. production and growth. *Monthly Notices of the Royal Astronomical Society*, *425*(1), 460–469. Retrieved from <https://arxiv.org/abs/1206.2309> doi: 10.1111/j.1365-2966.2012.21433.x
- Meakin, C. A., & Arnett, D. (2007). Turbulent convection in stellar interiors. i. hydrodynamic simulation. *The Astrophysical Journal*, *667*(1), 448–475. doi: 10.1086/520318

- Mereghetti, S. (2008). The strongest cosmic magnets: soft gamma-ray repeaters and anomalous x-ray pulsars. *The Astronomy and Astrophysics Review*, 15, 225–287. doi: 10.1007/s00159-008-0011-z
- Miller-Jones, J. C. A., et al. (2021). Cygnus X-1 contains a 21-solar mass black hole—Implications for massive star winds. *Science*, 371(6533), 1046–1049. doi: 10.1126/science.abb3363
- Minka, T. P. (2000). *Automatic choice of dimensionality for pca* (Tech. Rep.).
- Misner, C. W., Thorne, K. S., & Wheeler, J. A. (1973). *Gravitation*. W. H. Freeman and Company.
- Moe, M., & Di Stefano, R. (2017). Mind your ps and qs: The interrelation between period (p) and mass-ratio (q) distributions of binary stars. *The Astrophysical Journal Supplement Series*, 230(2), 15. Retrieved from <https://arxiv.org/abs/1606.05347> doi: 10.3847/1538-4365/aa6fb6
- Mordasini, C., Alibert, Y., Benz, W., & Naef, D. (2009). Extrasolar planet population synthesis. i. method, formation tracks, and mass-distance distribution. *Astronomy Astrophysics*, 501(3), 1139–1160. doi: 10.1051/0004-6361/200810961
- Muijres, L. E., de Koter, A., Vink, J. S., Krtićka, J., Kubát, J., & Langer, N. (2011, February). Predictions of the effect of clumping on the wind properties of O-type stars. , 526, A32. doi: 10.1051/0004-6361/201014290
- Mukherjee, S., Obaid, R., & Matkarimov, B. (2010, aug). Classification of glitch waveforms in gravitational wave detector characterization. *Journal of Physics: Conference Series*, 243, 012006. Retrieved from <https://doi.org/10.1088/1742-6596/243/1/012006> doi: 10.1088/1742-6596/243/1/012006
- Müller, C., & Anabel, M. (2018). *Gravitational-wave astronomy with compact binary coalescences : From blip glitches to the black hole area increase law* (Doctoral Thesis, Hannover : Institutionelles Repositorium der Leibniz Universität Hannover). doi: 10.15488/3422
- Müller, P. E., & Vink, J. S. (2008, December). A consistent solution for the velocity field and mass-loss rate of massive stars. , 492(2), 493-509. doi: 10.1051/0004-6361:20078798
- Müller, B., Janka, H.-T., & Heger, A. (2012). A new multi-dimensional general relativistic neutrino hydrodynamics code for core-collapse supernovae. i. method and code tests in spherical symmetry. *The Astrophysical Journal*, 761(1), 72. doi: 10.1088/0004-637X/761/1/72

- Nadezhin, D. K. (1980, May). Some Secondary Indications of Gravitational Collapse. , *69*(1), 115-125. doi: 10.1007/BF00638971
- Neijssel, C. J., Vigna-Gómez, A., Stevenson, S., Barrett, J. W., Gaebel, S. M., Broekgaarden, F. S., ... Mandel, I. (2019, December). The effect of the metallicity-specific star formation history on double compact object mergers. , *490*(3), 3740-3759. doi: 10.1093/mnras/stz2840
- Neijssel, C. J., Vinciguerra, S., Vigna-Gomez, A., Hirai, R., Miller-Jones, J. C. A., Bahramian, A., ... Mandel, I. (2021). Wind mass-loss rates of stripped stars inferred from Cygnus X-1. *Astrophys. J.*, *908*(2), 118. doi: 10.3847/1538-4357/abde4a
- Neustadt, J. M. M., Kochanek, C. S., Stanek, K. Z., Basinger, C., Jayasinghe, T., Garling, C. T., ... Gerke, J. (2021, November). The search for failed supernovae with the Large Binocular Telescope: a new candidate and the failed SN fraction with 11 yr of data. , *508*(1), 516-528. doi: 10.1093/mnras/stab2605
- Nieuwenhuijzen, H., & de Jager, C. (1990, May). Parametrization of stellar rates of mass loss as functions of the fundamental stellar parameters M, L, and R. , *231*, 134-136.
- Nieuwenhuijzen, H., & de Jager, C. (2000, January). Checking the yellow evolutionary void. Three evolutionary critical Hypergiants: HD 33579, HR 8752 & IRC +10420. , *353*, 163-176.
- Nieva, M.-F. (2013, January). Temperature, gravity, and bolometric correction scales for non-supergiant ob stars. *Astronomy amp; Astrophysics*, *550*, A26. Retrieved from <http://dx.doi.org/10.1051/0004-6361/201219677> doi: 10.1051/0004-6361/201219677
- Noyes, R. W., Weiss, N. O., & Vaughan, A. H. (1984). Rotation, convection, and magnetic activity in lower main-sequence stars. *The Astrophysical Journal*, *279*, 763-777. doi: 10.1086/161945
- Nugis, T., & Lamers, H. J. G. L. M. (2000, August). Mass-loss rates of Wolf-Rayet stars as a function of stellar parameters. , *360*, 227-244.
- Ou, P.-S., Chen, K.-J., Chu, Y.-H., & Tsai, S.-H. (2023, February). Critical Metallicity of Cool Supergiant Formation. I. Effects on Stellar-mass Loss and Feedback. , *944*(1), 34. doi: 10.3847/1538-4357/aca96e
- O'Connor, E., & Ott, C. D. (2011, March). Black hole formation in failing core-collapse supernovae. *The Astrophysical Journal*, *730*(2), 70. Retrieved from <http://dx.doi.org/10.1088/0004-637X/730/2/70> doi: 10.1088/0004-637x/730/2/70

- Palamos, J. (2020). *Search for gravitational wave signals associated with gamma-ray bursts during ligo's second observing run* (Ph.D. Dissertation, University of Oregon). Retrieved from <https://scholarsbank.uoregon.edu/items/c214778f-6465-4344-90d8-4d6872375ac1>
- Pamyatnykh, A. A. (1999). Pulsational instability domain of hot main sequence stars: Observational constraints and theoretical challenges. *Acta Astronomica*, *49*, 119–148.
- Panuzzo, P., Mazeh, T., Arenou, F., Holl, B., Caffau, E., Jorissen, A., ... Zwitter, T. (2024, April). Discovery of a dormant 33 solar-mass black hole in pre-release gaia astrometry. *Astronomy & Astrophysics*. Retrieved from <http://dx.doi.org/10.1051/0004-6361/202449763> doi: 10.1051/0004-6361/202449763
- Pauldrach, A., Puls, J., & Kudritzki, R. P. (1986, August). Radiation-driven winds of hot luminous stars. Improvements of the theory and first results. , *164*, 86-100.
- Pauli, D., Oskinova, L. M., Hamann, W. R., Bowman, D. M., Todt, H., Shenar, T., ... Wofford, A. (2023, May). Spectroscopic and evolutionary analyses of the binary system AzV 14 outline paths toward the WR stage at low metallicity. , *673*, A40. doi: 10.1051/0004-6361/202345881
- Pauli, D., Oskinova, L. M., Hamann, W. R., Ramachandran, V., Todt, H., Sander, A. A. C., ... Prinja, R. (2022, March). The earliest O-type eclipsing binary in the Small Magellanic Cloud, AzV 476: A comprehensive analysis reveals surprisingly low stellar masses. , *659*, A9. doi: 10.1051/0004-6361/202141738
- Paxton, B., Bildsten, L., Dotter, A., & et al. (2011). Modules for experiments in stellar astrophysics (mesa). *ApJS*, *192*, 3. Retrieved from <https://arxiv.org/abs/1009.1622> doi: 10.1088/0067-0049/192/1/3
- Paxton, B., Cantiello, M., Arras, P., & et al. (2013). Modules for experiments in stellar astrophysics (mesa): Planets, oscillations, rotation, and massive stars. *The Astrophysical Journal Supplement Series*, *208*(1), 4. Retrieved from <https://arxiv.org/abs/1301.0319> doi: 10.1088/0067-0049/208/1/4
- Pejcha, O., Metzger, B. D., & Tomida, K. (2016). Cool and luminous transients from mass-losing binary stars. *Monthly Notices of the Royal Astronomical Society*, *461*(3), 2527–2539. Retrieved from <https://arxiv.org/abs/1604.07414> doi: 10.1093/mnras/stw1412

- Petrov, B., Vink, J. S., & Gräfener, G. (2016, May). Two bi-stability jumps in theoretical wind models for massive stars and the implications for luminous blue variable supernovae. , *458*(2), 1999-2011. doi: 10.1093/mnras/stw382
- Pols, O. R. (2011). *Stellar structure and evolution*.
<https://www.ucolick.org/~woosley/ay112-14/texts/pols11.pdf>.
 (Lecture notes, Utrecht University)
- Pols, O. R., Schröder, K.-P., Hurley, J. R., Tout, C. A., & Eggleton, P. P. (1998, August). Stellar evolution models for $Z = 0.0001$ to 0.03 . , *298*(2), 525-536. doi: 10.1046/j.1365-8711.1998.01658.x
- Portegies Zwart, S. F., & Verbunt, F. (1996). Population synthesis of high-mass binaries. *Astronomy and Astrophysics*, *309*, 179-196.
- Powell, J., Torres-Forné, A., Lynch, R., Trifirò, D., Cuoco, E., Cavaglià, M., ... Font, J. A. (2017, Jan). Classification methods for noise transients in advanced gravitational-wave detectors ii: performance tests on advanced ligo data. *Classical and Quantum Gravity*, *34*(3), 034002. Retrieved from <http://dx.doi.org/10.1088/1361-6382/34/3/034002> doi: 10.1088/1361-6382/34/3/034002
- Powell, J., Trifirò, D., Cuoco, E., Heng, I. S., & Cavaglià, M. (2015, Oct). Classification methods for noise transients in advanced gravitational-wave detectors. *Classical and Quantum Gravity*, *32*(21), 215012. Retrieved from <http://dx.doi.org/10.1088/0264-9381/32/21/215012> doi: 10.1088/0264-9381/32/21/215012
- Qin, Y., Marchant, P., Fragos, T., Meynet, G., & Kalogera, V. (2019, January). On the Origin of Black Hole Spin in High-mass X-Ray Binaries. , *870*(2), L18. doi: 10.3847/2041-8213/aaf97b
- Qin, Y., Marchant, P., Fragos, T., Meynet, G., Kalogera, V., & Andrews, J. J. (2018). The spin of the second-born black hole in coalescing binary black holes. *Astronomy Astrophysics*, *616*, A28. Retrieved from <https://arxiv.org/abs/1803.02623> doi: 10.1051/0004-6361/201832834
- Rakavy, G., & Shaviv, G. (1967, June). Instabilities in Highly Evolved Stellar Models. , *148*, 803. doi: 10.1086/149204
- Ramachandran, V., Hamann, W. R., Oskinova, L. M., Gallagher, J. S., Hainich, R., Shenar, T., ... Fulmer, L. (2019, May). Testing massive star evolution, star formation history, and feedback at low metallicity. Spectroscopic analysis of OB stars in the SMC Wing. , *625*, A104. doi: 10.1051/0004-6361/201935365

- Ramachandran, V., Sander, A. A. C., Pauli, D., Klencki, J., Backs, F., Tramper, F., ... the XShootU collaboration (2024, June). X-Shooting ULLYSES: Massive Stars at low metallicity VIII. Stellar and wind parameters of newly revealed stripped stars in Be binaries. *arXiv e-prints*, arXiv:2406.17678. doi: 10.48550/arXiv.2406.17678
- Renzo, M., Hendriks, D. D., van Son, L. A. C., & Farmer, R. (2022, February). Pair-instability Mass Loss for Top-down Compact Object Mass Calculations. *Research Notes of the American Astronomical Society*, 6(2), 25. doi: 10.3847/2515-5172/ac503e
- Renzo, M., & Smith, N. (2024, July). Pair-instability evolution and explosions in massive stars. *arXiv e-prints*, arXiv:2407.16113. doi: 10.48550/arXiv.2407.16113
- Rickard, M. J., Hainich, R., Hamann, W. R., Oskinova, L. M., Prinja, R. K., Ramachandran, V., ... Gallagher, J. S. (2022, October). Stellar wind properties of the nearly complete sample of O stars in the low metallicity young star cluster NGC 346 in the SMC galaxy. , 666, A189. doi: 10.1051/0004-6361/202243281
- Ricker, P. M., & Taam, R. E. (2012). Inspiration and fallback in the common envelope binary interaction. *The Astrophysical Journal*, 746(1), 74. doi: 10.1088/0004-637X/746/1/74
- Riley, J., Agrawal, P., Barrett, J. W., Boyett, K. N. K., Broekgaarden, F. S., Chattopadhyay, D., ... Willcox, R. (2022, February). Rapid stellar and binary population synthesis with compas. *The Astrophysical Journal Supplement Series*, 258(2), 34. Retrieved from <http://dx.doi.org/10.3847/1538-4365/ac416c> doi: 10.3847/1538-4365/ac416c
- Riley, J., Mandel, I., Marchant, P., Butler, E., Nathaniel, K., Neijssel, C., ... Vigna-Gomez, A. (2021a). Chemically homogeneous evolution: a rapid population synthesis approach. *Mon. Not. Roy. Astron. Soc.*, 505(1), 663–676. doi: 10.1093/mnras/stab1291
- Riley, J., Mandel, I., Marchant, P., Butler, E., Nathaniel, K., Neijssel, C., ... Vigna-Gómez, A. (2021b, May). Chemically homogeneous evolution: a rapid population synthesis approach. *Monthly Notices of the Royal Astronomical Society*, 505(1), 663–676. Retrieved from <http://dx.doi.org/10.1093/mnras/stab1291> doi: 10.1093/mnras/stab1291

- Riley, J., et al. (2022a, January). COMPAS: A rapid binary population synthesis suite. *The Journal of Open Source Software*, 7(69), 3838. doi: 10.21105/joss.03838
- Riley, J., et al. (2022b). Rapid Stellar and Binary Population Synthesis with COMPAS. *Astrophys. J. Supp.*, 258(2), 34. doi: 10.3847/1538-4365/ac416c
- Riley, J., Stevenson, S., Vigna-Gómez, A., Neijssel, C. J., Mandel, I., Barrett, J. W., . . . Woosley, S. E. (2022). Rapid stellar and binary population synthesis with compas. *The Astrophysical Journal Supplement Series*, 258, 34. doi: 10.3847/1538-4365/ac3f2c
- Rodriguez, C. L., Haster, C.-J., Chatterjee, S., Kalogera, V., & Rasio, F. A. (2016). Binary black hole mergers from globular clusters: Masses, merger rates, and the impact of stellar evolution. *The Astrophysical Journal Letters*, 824(1), L8. Retrieved from <https://arxiv.org/abs/1604.04254> doi: 10.3847/2041-8205/824/1/L8
- Romagnolo, A., Gormaz-Matamala, A. C., & Belczynski, K. (2024, April). On the Maximum Black Hole Mass at Solar Metallicity. , 964(2), L23. doi: 10.3847/2041-8213/ad2fbe
- Romero-Shaw, I., Hirai, R., Bahramian, A., Willcox, R., & Mandel, I. (2023, September). Rapid population synthesis of black hole high-mass X-ray binaries: implications for binary stellar evolution. , 524(1), 245-259. doi: 10.1093/mnras/stad1732
- Ross, M. P., Mistry, T., Datrier, L., Kissel, J., Venkateswara, K., Weller, C., . . . Gundlach, J. (2021). *Initial results from the ligo newtonian calibrator*. Retrieved from <https://arxiv.org/abs/2107.00141>
- Sabhahit, G. N., Vink, J. S., Sander, A. A. C., & Higgins, E. R. (2023). Very massive stars and pair-instability supernovae: mass-loss framework for low metallicity. *Mon. Not. Roy. Astron. Soc.*, 524(1), 1529–1546. doi: 10.1093/mnras/stad1888
- Sahu, K. C., Anderson, J., Casertano, S., & et al. (2022). An isolated stellar-mass black hole detected through astrometric microlensing. *The Astrophysical Journal*, 933(1), 83. doi: 10.3847/1538-4357/ac6dfa
- Salpeter, E. E. (1955). The luminosity function and stellar evolution. *The Astrophysical Journal*, 121, 161–167. doi: 10.1086/145971
- Sana, H., de Mink, S. E., de Koter, A., Langer, N., Evans, C. J., Gieles, M., . . . Schneider, F. R. N. (2012, July). Binary Interaction Dominates the Evolution of Massive Stars. *Science*, 337(6093), 444. doi: 10.1126/science.1223344

- Sana, H., de Mink, S. E., de Koter, A., Langer, N., Evans, C. J., Gieles, M., . . . Schneider, F. R. N. (2012). Binary interaction dominates the evolution of massive stars. *Science*, *337*(6093), 444–446. Retrieved from <https://arxiv.org/abs/1207.6397> doi: 10.1126/science.1223344
- Sander, A., Todt, H., Hainich, R., & Hamann, W. R. (2014, March). The Wolf-Rayet stars in M 31. I. Analysis of the late-type WN stars. , *563*, A89. doi: 10.1051/0004-6361/201323240
- Sander, A. A. C., Hamann, W. R., Todt, H., Hainich, R., & Shenar, T. (2017, July). Coupling hydrodynamics with comoving frame radiative transfer. I. A unified approach for OB and WR stars. , *603*, A86. doi: 10.1051/0004-6361/201730642
- Sander, A. A. C., Lefever, R. R., Poniatowski, L. G., Ramachandran, V., Sabhahit, G. N., & Vink, J. S. (2023, February). The temperature dependency of Wolf-Rayet-type mass loss. An exploratory study for winds launched by the hot iron bump. , *670*, A83. doi: 10.1051/0004-6361/202245110
- Sander, A. A. C., & Vink, J. S. (2020, November). On the nature of massive helium star winds and Wolf-Rayet-type mass-loss. , *499*(1), 873-892. doi: 10.1093/mnras/staa2712
- Saulson, P. R. (2003). *The history of ligo*. https://www.ligo.caltech.edu/system/media_files/binaries/386/original/LIGOHistory.pdf. (LIGO Laboratory public document)
- Schofield, R., Covas, P., Effler, A., & Savage, R. (2017). *Why the gw channel detects thirsty black ravens along with colliding black holes*. (<https://alog.ligo-wa.caltech.edu/aLOG/index.php?callRep=37630>)
- Schutz, B. F. (1985). *A first course in general relativity*. Cambridge University Press.
- Schwarzschild, K. (1906). Über das Gleichgewicht der Sonnenatmosphäre. *Nachrichten von der Gesellschaft der Wissenschaften zu Göttingen, Mathematisch-Physikalische Klasse*, 41–53.
- Shenar, T., Gilkis, A., Vink, J. S., Sana, H., & Sander, A. A. C. (2020, February). Why binary interaction does not necessarily dominate the formation of Wolf-Rayet stars at low metallicity. , *634*, A79. doi: 10.1051/0004-6361/201936948
- Shenar, T., Hainich, R., Todt, H., Sander, A., Hamann, W. R., Moffat, A. F. J., . . . Richardson, N. D. (2016, June). Wolf-Rayet stars in the Small Magellanic Cloud. II. Analysis of the binaries. , *591*, A22. doi: 10.1051/0004-6361/201527916

- Shenar, T., Sablowski, D. P., Hainich, R., Todt, H., Moffat, A. F. J., Oskinova, L. M., . . . Hamann, W. R. (2019, July). The Wolf-Rayet binaries of the nitrogen sequence in the Large Magellanic Cloud. Spectroscopy, orbital analysis, formation, and evolution. , *627*, A151. doi: 10.1051/0004-6361/201935684
- Shikauchi, M., Hirai, R., & Mandel, I. (2024). *Evolution of the convective core mass during the main sequence*. Retrieved from <https://arxiv.org/abs/2409.00460>
- Smartt, S. J. (2015, April). Observational Constraints on the Progenitors of Core-Collapse Supernovae: The Case for Missing High-Mass Stars. , *32*, e016. doi: 10.1017/pasa.2015.17
- Smartt, S. J., Eldridge, J. J., Crockett, R. M., & Maund, J. R. (2009, May). The death of massive stars - i. observational constraints on the progenitors of type ii-p supernovae. *Monthly Notices of the Royal Astronomical Society*, *395*(3), 1409–1437. Retrieved from <http://dx.doi.org/10.1111/j.1365-2966.2009.14506.x> doi: 10.1111/j.1365-2966.2009.14506.x
- Snedden, C. (1973). Carbon and nitrogen abundances in metal-poor stars. *ApJ*, *184*, 839–849. doi: 10.1086/152374
- Soberman, G. E., Phinney, E. S., & van den Heuvel, E. P. J. (1997). Stability criteria for mass transfer in binary stellar evolution. *Astronomy and Astrophysics*, *327*, 620–635.
- Soni, S., Berry, C. P. L., Coughlin, S. B., Harandi, M., Jackson, C. B., Crowston, K., . . . Zhang, C. (2021). *Discovering features in gravitational-wave data through detector characterization, citizen science and machine learning*.
- Stassun, K. G., Collins, K. A., & Gaudi, B. S. (2017). Accurate empirical radii and masses of planets and their host stars with gaia parallaxes. *The Astronomical Journal*, *153*(3), 136.
- Stevenson, S., & Clarke, T. A. (2022, December). Constraints on the contributions to the observed binary black hole population from individual evolutionary pathways in isolated binary evolution. , *517*(3), 4034-4053. doi: 10.1093/mnras/stac2936
- Stevenson, S., Sampson, M., Powell, J., Vigna-Gómez, A., Neijssel, C. J., Szécsi, D., & Mandel, I. (2019, September). The Impact of Pair-instability Mass Loss on the Binary Black Hole Mass Distribution. , *882*(2), 121. doi: 10.3847/1538-4357/ab3981

- Stevenson, S., Vigna-Gómez, A., Mandel, I., Barrett, J. W., Neijssel, C. J., Perkins, D., & de Mink, S. E. (2017). Formation of the first three gravitational-wave observations through isolated binary evolution. *Nature Commun.*, *8*, 14906. doi: 10.1038/ncomms14906
- The Royal Swedish Academy of Sciences. (2017). *The nobel prize in physics 2017 – scientific background: Gravitational waves and the ligo-virgo collaboration*. <https://www.nobelprize.org/uploads/2018/06/advanced-physicsprize2017.pdf>. (Nobel Prize official scientific background document)
- Tipping, M. E., & Bishop, C. (1999, January). Probabilistic principal component analysis. *Journal of the Royal Statistical Society, Series B*, *21*(3), 611-622. Retrieved from <https://www.microsoft.com/en-us/research/publication/probabilistic-principal-component-analysis/> (Available from <http://www.ncrg.aston.ac.uk/Papers/index.html>)
- Torres, G., Andersen, J., & Gimenez, A. (2010). Accurate masses and radii of normal stars: modern results and applications. *Astronomy and Astrophysics Review*, *18*, 67–126. doi: 10.1007/s00159-009-0025-1
- Torres-Forné, A., Cuoco, E., Font, J. A., & Marquina, A. (2020, Jul). Application of dictionary learning to denoise ligo’s blip noise transients. *Physical Review D*, *102*(2). Retrieved from <http://dx.doi.org/10.1103/PhysRevD.102.023011> doi: 10.1103/physrevd.102.023011
- Tramper, F., Sana, H., & de Koter, A. (2016, December). A New Prescription for the Mass-loss Rates of WC and WO Stars. , *833*(2), 133. doi: 10.3847/1538-4357/833/2/133
- Tutukov, A., & Yungelson, L. (1973, January). Evolution of massive close binaries. *Nauchnye Informatsii*, *27*, 70.
- van den Heuvel, E. P. J., & De Loore, C. (1973, June). The nature of X-ray binaries III. Evolution of massive close binaries with one collapsed component - with a possible application to Cygnus X-3. , *25*, 387.
- van Belle, G. T., Ciardi, D. R., Thompson, R. R., Akeson, R. L., & Lada, E. A. (2001). Directly determined linear radii and effective temperatures of exoplanet host stars. *The Astrophysical Journal*, *559*(2), 1155–1164. doi: 10.1086/322411
- Vanbeveren, D., De Loore, C., & Van Rensbergen, W. (1998, January). Massive stars. , *9*(1-2), 63-152. doi: 10.1007/s001590050015

- van der Walt, S., Colbert, S. C., & Varoquaux, G. (2011, Mar). The numpy array: A structure for efficient numerical computation. *Computing in Science & Engineering*, *13*(2), 22–30. Retrieved from <http://dx.doi.org/10.1109/MCSE.2011.37> doi: 10.1109/mcse.2011.37
- van Son, L. A. C., de Mink, S. E., Renzo, M., Justham, S., Zapartas, E., Breivik, K., ... Conroy, C. (2022, December). No peaks without valleys: The stable mass transfer channel for gravitational-wave sources in light of the neutron star–black hole mass gap. *The Astrophysical Journal*, *940*(2), 184. Retrieved from <http://dx.doi.org/10.3847/1538-4357/ac9b0a> doi: 10.3847/1538-4357/ac9b0a
- van Son, L. A. C., Roy, S. K., Mandel, I., Farr, W. M., Lam, A., Merritt, J., ... Andrews, J. J. (2024). *Winds of change: why binary black hole formation is metallicity dependent, while binary neutron star formation is not*. Retrieved from <https://arxiv.org/abs/2411.02484>
- Vassiliadis, E., & Wood, P. R. (1993, August). Evolution of Low- and Intermediate-Mass Stars to the End of the Asymptotic Giant Branch with Mass Loss. , *413*, 641. doi: 10.1086/173033
- Veitch, J., Raymond, V., Farr, B., Farr, W. M., Graff, P., Vitale, S., ... Vecchio, A. (2015). Parameter estimation for compact binaries with ground-based gravitational-wave observations using the lalinference software library. *Phys. Rev. D*, *91*, 042003. doi: 10.1103/PhysRevD.91.042003
- Viallet, M., Meakin, C., Arnett, D., & Mocák, M. (2013). Toward global hydrodynamical models of stellar interiors. *The Astrophysical Journal*, *769*(1), 1. doi: 10.1088/0004-637X/769/1/1
- Vink, J. S. (2017, November). Winds from stripped low-mass helium stars and Wolf-Rayet stars. , *607*, L8. doi: 10.1051/0004-6361/201731902
- Vink, J. S. (2022, August). Theory and Diagnostics of Hot Star Mass Loss. , *60*, 203-246. doi: 10.1146/annurev-astro-052920-094949
- Vink, J. S., & de Koter, A. (2005, November). On the metallicity dependence of Wolf-Rayet winds. , *442*(2), 587-596. doi: 10.1051/0004-6361:20052862
- Vink, J. S., de Koter, A., & Lamers, H. J. G. L. M. (1999, October). On the nature of the bi-stability jump in the winds of early-type supergiants. , *350*, 181-196. doi: 10.48550/arXiv.astro-ph/9908196
- Vink, J. S., de Koter, A., & Lamers, H. J. G. L. M. (2000, October). New theoretical mass-loss rates of O and B stars. , *362*, 295-309. doi: 10.48550/arXiv.astro-ph/0008183

- Vink, J. S., de Koter, A., & Lamers, H. J. G. L. M. (2001, April). Mass-loss predictions for O and B stars as a function of metallicity. , *369*, 574-588. doi: 10.1051/0004-6361:20010127
- Vink, J. S., & Gräfener, G. (2012, June). The Transition Mass-loss Rate: Calibrating the Role of Line-driven Winds in Massive Star Evolution. , *751*(2), L34. doi: 10.1088/2041-8205/751/2/L34
- Vink, J. S., Heger, A., Krumholz, M. R., Puls, J., Banerjee, S., Castro, N., ... Zhang, Y. (2015, March). Very Massive Stars in the local Universe. *Highlights of Astronomy*, *16*, 51-79. doi: 10.1017/S1743921314004657
- Vink, J. S., Higgins, E. R., Sander, A. A. C., & Sabhahit, G. N. (2021, June). Maximum black hole mass across cosmic time. , *504*(1), 146-154. doi: 10.1093/mnras/stab842
- Vink, J. S., Mehner, A., Crowther, P. A., Fullerton, A., Garcia, M., Martins, F., ... Wang, L. (2023, July). X-Shooting ULLYSES: Massive stars at low metallicity. I. Project description. , *675*, A154. doi: 10.1051/0004-6361/202245650
- Vink, J. S., Muijres, L. E., Anthonisse, B., de Koter, A., Gräfener, G., & Langer, N. (2011, July). Wind modelling of very massive stars up to 300 solar masses. , *531*, A132. doi: 10.1051/0004-6361/201116614
- Vink, J. S., & Sabhahit, G. N. (2023, October). Exploring the Red Supergiant wind kink. A Universal mass-loss concept for massive stars. , *678*, L3. doi: 10.1051/0004-6361/202347801
- Vink, J. S., Sabhahit, G. N., & Higgins, E. R. (2024, August). The maximum black hole mass at solar metallicity. , *688*, L10. doi: 10.1051/0004-6361/202450655
- Vink, J. S., & Sander, A. A. C. (2021, June). Metallicity-dependent wind parameter predictions for OB stars. , *504*(2), 2051-2061. doi: 10.1093/mnras/stab902
- Virtanen, P., Gommers, e. a., & SciPy 1.0 Contributors. (2020). SciPy 1.0: Fundamental Algorithms for Scientific Computing in Python. *Nature Methods*, *17*, 261–272. doi: 10.1038/s41592-019-0686-2
- Wagg, T., Broekgaarden, F. S., de Mink, S. E., Frankel, N., van Son, L. A. C., & Justham, S. (2022, October). Gravitational Wave Sources in Our Galactic Backyard: Predictions for BHBH, BHNS, and NSNS Binaries Detectable with LISA. , *937*(2), 118. doi: 10.3847/1538-4357/ac8675

- Wang, T., Jiang, B., Ren, Y., Yang, M., & Li, J. (2021, May). Red Supergiants in M31 and M33. II. The Mass-loss Rate. , *912*(2), 112. doi: 10.3847/1538-4357/abed4b
- Weber, J. (1960). Detection and generation of gravitational waves. *Physical Review*, *117*(1), 306–313. doi: 10.1103/PhysRev.117.306
- Weber, J. (1969). Evidence for discovery of gravitational radiation. *Physical Review Letters*, *22*(24), 1320–1324. doi: 10.1103/PhysRevLett.22.1320
- Weiss, R. (1972). Electromagnetically coupled broadband gravitational antenna. *Quarterly Progress Report of the MIT Research Laboratory of Electronics*, *105*.
- Weiss, R., Drever, R., & Thorne, K. S. (1992). *Proposal to the national science foundation: The ligo project* (Tech. Rep.). California Institute of Technology and Massachusetts Institute of Technology. (Submitted to the NSF; foundational document for the approval of LIGO)
- Wen, J., Gao, J., Yang, M., Chen, B., Ren, Y., Wang, T., & Jiang, B. (2024, January). Evolved Massive Stars at Low-metallicity VI. Mass-Loss Rate of Red Supergiant Stars in the Large Magellanic Cloud. *arXiv e-prints*, arXiv:2401.03778. doi: 10.48550/arXiv.2401.03778
- Willems, B., Kolb, U., Justham, S., & Tout, C. A. (2010). Bisepts: a new binary population synthesis code. *Monthly Notices of the Royal Astronomical Society*, *401*, 191-206. doi: 10.1111/j.1365-2966.2009.15652.x
- Woosley, S. E. (2017). Pulsational pair-instability supernovae. *Astrophysical Journal*, *836*(2), 244. doi: 10.3847/1538-4357/836/2/244
- Woosley, S. E. (2017, February). Pulsational Pair-instability Supernovae. , *836*(2), 244. doi: 10.3847/1538-4357/836/2/244
- Woosley, S. E., Heger, A., & Weaver, T. A. (2002). The evolution and explosion of massive stars. *Reviews of Modern Physics*, *74*, 1015–1071. Retrieved from <https://arxiv.org/abs/astro-ph/0206004> doi: 10.1103/RevModPhys.74.1015
- Woosley, S. E., Sukhbold, T., & Janka, H. T. (2020, June). The Birth Function for Black Holes and Neutron Stars in Close Binaries. , *896*(1), 56. doi: 10.3847/1538-4357/ab8cc1

- Yamamoto, K., Hayakawa, H., Okada, A., Uchiyama, T., Miyoki, S., Ohashi, M., ... Tsunesada, Y. (2008, Jul). Effect of energy deposited by cosmic-ray particles on interferometric gravitational wave detectors. *Physical Review D*, 78(2). Retrieved from <http://dx.doi.org/10.1103/PhysRevD.78.022004> doi: 10.1103/physrevd.78.022004
- Yang, M., Bonanos, A. Z., Jiang, B., Zapartas, E., Gao, J., Ren, Y., ... Luo, C. (2023, August). Evolved massive stars at low-metallicity. V. Mass-loss rate of red supergiant stars in the Small Magellanic Cloud. , 676, A84. doi: 10.1051/0004-6361/202244770
- Yoon, S.-C., & Cantiello, M. (2010, July). Evolution of Massive Stars with Pulsation-driven Superwinds During the Red Supergiant Phase. , 717(1), L62-L65. doi: 10.1088/2041-8205/717/1/L62
- Yoon, S. C., Langer, N., & Norman, C. (2006, December). Single star progenitors of long gamma-ray bursts. I. Model grids and redshift dependent GRB rate. , 460(1), 199-208. doi: 10.1051/0004-6361:20065912
- Zahn, J.-P. (1975). The dynamical tide in close binaries. *Astronomy and Astrophysics*, 41, 329-344.
- Zapartas, E., Renzo, M., Fragos, T., Dotter, A., Andrews, J. J., Bavera, S. S., ... Xing, Z. P. (2021, December). Revisiting the explodability of single massive star progenitors of stripped-envelope supernovae. , 656, L19. doi: 10.1051/0004-6361/202141506
- Zevin, M., Coughlin, S., Bahaadini, S., Besler, E., Rohani, N., Allen, S., ... et al. (2017, Feb). Gravity spy: integrating advanced ligo detector characterization, machine learning, and citizen science. *Classical and Quantum Gravity*, 34(6), 064003. Retrieved from <http://dx.doi.org/10.1088/1361-6382/aa5cea> doi: 10.1088/1361-6382/aa5cea